INFORMATION TO USERS

72-26,462

PAWLOSKI, John Norman, 1939-
ION-ELECTRON RECOMBINATION STUDIES OF SOME
SIMPLE POLYATOMIC POSITIVE IONS IN THE GAS
PHASE.

Rice University, Ph.D., 1972
Chemistry, physical

University Microfilms, A XEROX Company , Ann Arbor, Michigan

RICE UNIVERSITY

Ion-Electron Recombination Studies of Some Simple
Polyatomic Positive Ions in the Gas Phase
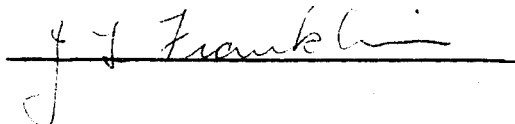
by

John N. Pawloski

A THESIS SUBMITTED
IN PARTIAL FULFILLMENT OF THE
REQUIREMENTS FOR THE DEGREE OF

DOCTOR OF PHILOSOPHY

Thesis Director's signature:

Houston, Texas

May, 1972

PLEASE NOTE:

Some pages may have

indistinct print.

. Filmed as received.

University Microfilms, A Xerox Education Company

TABLE OF CONTENTS

TABLE OF CONTENTS (continued)

ACKNOWLEDGMENTS

A project of this nature requires many and various resources for a successful conclusion. I would like to offer my sincere thanks to the following:

LIST OF FIGURES

I. INTRODUCTION

A. The Recombination Problem

The study of chemical reactions, their rates, mechanisms and products has been one of the most actively pursued areas in science. Although many techniques have been developed on the macroscopic level of investigation, it has long been the desire of the kineticist to view each reaction from the standpoint of discrete particle collisions. Only in this manner can he consider himself a spectator in the full sense.

Observation of reactions on the particle level leads to a more concise picture of

(1) the intermolecular potentials; both long and short range.

(2) the distribution of products over the solid angle energetically allowed.

(3) the reaction mechanism over a given energy range.

The general method employed in these experiments involves generating beams of the reactant species and observing their collisions at a given point within the apparatus. The types of reactions which have been studied in this manner are:

1. electron-neutral

2. electron-ion

3. ion-neutral

4. ion-ion

5. neutral-neutral

Table I gives examples of each of the above interactions available in the current literature. This research deals with the second category, namely, ion-electron recombination.

1

Table I

Collisions Investigated by Beam Techniques

Collision Event		Year	Reference
electron-neutral	$Cs + e^- \rightarrow Cs + e^-$	1971	(2)
electron-ion	$N_2^+ + e^- \rightarrow N + N$	1968	(3)
ion-neutral	$N^+ + O_2 \rightarrow NO^+ + O$	1971	(4)
ion-ion	$N^+ + O^- \rightarrow N + O$	1968	(5)
neutral-neutral	$Cs + RbCl \rightarrow CsCl + Rb$	1967	(6)

Recombination studies of ions with electrons date back to the work
of Thomson and Rutherford (1) in 1896. Many attempts have been made since
but the data available are still not comprehensive. The systems investi-
gated have been limited to diatomic molecular ions due to the experimental
difficulty of product identification. Only in the diatomic case can theory
predict the products since but one decomposition path is allowed. This,
however, should not imply that such recombinations have been thoroughly
investigated.

Collision phenomena can further be categorized as to the disposition
of energy when the reactant particles come together. The energy can (a)
be observed as radiation, (b) be transferred to a third body, or (c)
internally excite the resulting neutral molecule. If internal excitation
occurs, the recombination is transitory unless the excitation energy is
dissipated. The process is termed dissociative recombination if the
neutral excited complex breaks into atoms or radicals which move apart.
This phenomenon is represented below.

$$AX^+ + e^- \rightarrow (AX)^* \rightarrow A + X + \text{kinetic energy}$$
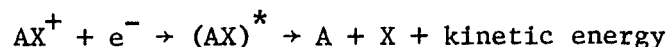
where AX^+ represents a molecular ion, either diatomic or polyatomic; e
is an electron; $(AX)^*$ is the unstable complex and A, X are the neutral
fragments which can be in excited states themselves. Initially, as the
principals in recombination approach each other, the electron is attracted
by the Coloumb potential of the ion. If favorable curve crossing occurs
for the system's potential energy versus internuclear separation, as
illustrated by Figure 1, then the molecular ion captures the electron
into a non-bonding or anti-bonding molecular state, $(AX)^*$. In this case,
there is no change in the total energy of the system and considerable

3

Figure 1

Potential Energy vs Internuclear Separation Illustrating Curve Crossing

in Dissociative Recombination

G. Initial state of system indicating the molecular ion in its ground

state of vibration with the electron at rest at infinity.

B. Curve representing repulsive state of excited molecule AX^*.

Z. Critical point of curve crossing; if internuclear separation

increases beyond point Z before electron is emitted then auto-

ionization is not possible energetically and dissociation goes

to completion.

Ed. Kinetic energy of dissociation, shared between atoms A^* and X.

C. Repulsion curve for A and X in ground states.

$A^+ + X + e^-(\infty)$

G

(AX^+)

$A^* + X$

E_D

Z

B

C

$A + X$

POTENTIAL ENERGY

INTERNUCLEAR DISTANCE
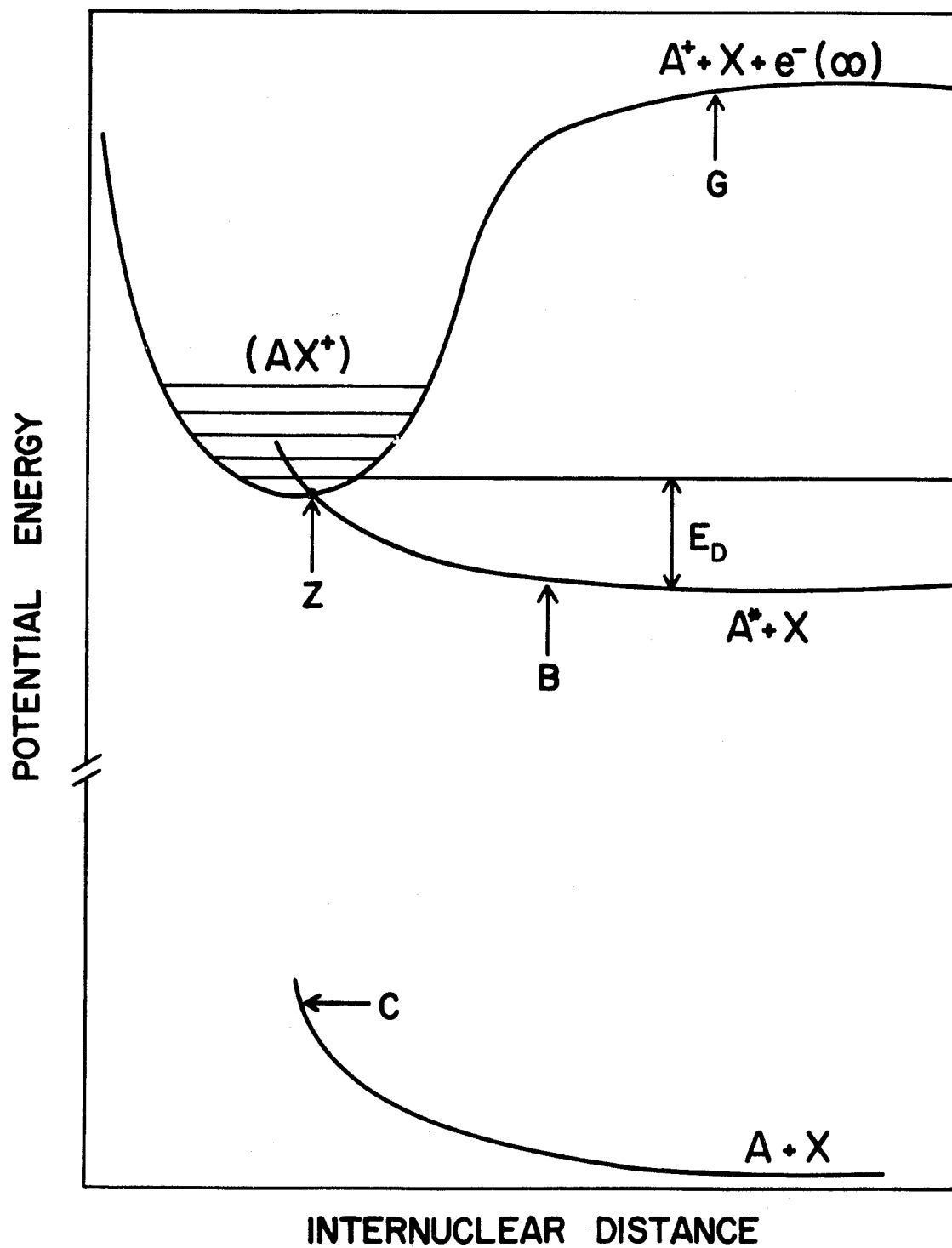
overlap occurs between the initial and final states of the system. The unstable molecule $(AX)^*$ can follow one of several paths in reaching a stable state. It can auto-ionize, $(AX)^* \rightarrow AX^+ + e^-$, or radiate the excess energy, $(AX)^* \rightarrow AX + hv$, or dissociate into neutral particles which can themselves be in excited states and move apart with excess kinetic energy as mentioned earlier.

Bates [7] has pointed out that the radiative path for the unstable molecule $(AX)^*$ has low probability of being followed. Atoms in an unstable state exert repulsive forces between them of approximately 5 eV/Å. If an internuclear separation of 0.2 Å occurs, the kinetic energy of relative motion is increased by 1 eV in 8×10^{-15} sec. If a separation of several angstroms is considered then about 10^{-13} sec would be necessary. Since radiative lifetimes are generally greater than 10^{-9} sec, the unstable neutral should prefer dissociation.

Sayers [8] has determined the rate coefficient for the reaction

$$N_2^+ + e^- + N_2 \rightarrow N_2^* + N_2$$
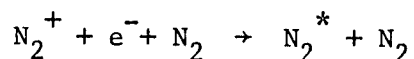
in which the excess energy from recombination is removed by a third body, namely, an N_2 neutral. He found that a process of this type would occur at a comparable rate to the dissociative recombination process at particle temperatures of 300°K and nitrogen pressures of the order of 0.1 atmosphere.

The purpose of this work, therefore, is to investigate positive ion-electron dissociative recombination for polyatomic positive ions employing a crossed beam technique. Identification of reaction products will be accomplished by mass spectroscopy.

II. PREVIOUS EXPERIMENTAL TECHNIQUES

A. The Microwave Experiment

In 1948, with the advent of microwave techniques for measurement of average electron densities in afterglows, Biondi and Brown (9) applied them to investigation of recombination phenomena. This marked the beginning of fairly comprehensive data acquisition for simple diatomic systems.

The microwave experiments concentrate on measuring local electron density variations after external ionizing sources have abated. A stationary electron energy distribution is assumed and described by position and time parameters in an equation of the form

$$\frac{\partial n_e}{\partial t}(\underline{r},t) = \sum_i C_i(\underline{r},t) - \sum_j L_j(\underline{r},t) - \sum_k \nabla \cdot \Gamma_e(\underline{r},t)$$

$$- \sum_\ell \alpha_\ell n_e(\underline{r},t)\, n_\ell(\underline{r},t) \qquad\qquad (1)$$

The parameters and terms are defined as

    (a) $\underline{r}$ represents position

    (b) t represents time

    (c) n_e is electron density

    (d) the C_i term represents electron creating processes

    (e) the L_j term indicates electron loss from other than recombination phenomena (i.e., negative ion formation)

    (f) Γ_e represents electron particle current density

    (g) the last term represents electron loss due to two body recombination with α_ℓ indicating the recombination coefficient.

If volume production terms are small and the main volume loss term is two body ion-electron recombination and if only one positive ion species is present with no negative ions then

$$dn_i/dt = dn_e/dt \qquad (2)$$

$$n_i \cong n_e \qquad (3)$$

The continuity equation becomes

$$\frac{dn_e}{dt} \cong -\alpha n_e^2 \qquad (4)$$

with the solution

$$\frac{1}{n_e} = \frac{1}{n_o} + \alpha t \qquad (5)$$

where n_o is the initial electron density at $t = 0$ and n_e is the electron density at time $t = t'$. Thus, a plot of the reciprocal of the electron density versus time will give the recombination coefficient.

Recombination coefficients measured by this technique have been found to vary from 10^{-8} to 10^{-6} cm^3/sec. At room temperature they fall into the range of $10^{-7} - 10^{-6}$ cc/ion sec for diatomic ions (10) of Ne, Ar, Kr and Xe and for N_2^+, O_2^+ and NO^+. For He_2^{+2} and H_2^+, 10^{-8} cc/ion sec (11).

Recombination phenomena were first approached on the beam level in 1929 by Davis and Barnes (12). They attempted, though unsuccessfully, to measure capture probability of He^{++} and He^+ with electrons as a function of their relative velocity. In 1966, Hammer and Aubrey (13) measured the recombination cross sections and coefficients for Cs_2^+ and Cs^+. Hagen (3) in 1968 measured these recombination parameters for molecular N_2^+ ions via beam technique.

B.   The Beam Experiment

A beam experiment in theory offers the following advantages over previous methods.

(a)   Primary ions, mass filtered for identification and energy selected.

(b)   Controlled electron energies in the neutralization region.

(c)   Identification of product species.

(d)   Angular distribution of products as a function of interaction energies.

(Figures 2 and 2a diagramatically illustrate the experiment.) The primary ion beam is considered to be parallel and composed of mono-energetic ions of velocity V (14). The electrons are also considered to be monoenergetic of velocity v. If the angle of intersection is denoted by Θ, the collision rate k(z)dz for single collisions in an element of height dz located at z in each beam is given by

$$k(z)dz = Q(\epsilon)\rho(z)\eta(z)\ \Lambda\ \omega(z)\ell(z)dz/\sin\Theta \qquad (6)$$

Q(ϵ) is the collision cross section at incident electron energy ϵ which corresponds to an incident velocity Λ given by

$$\Lambda = (V^2 + v^2 - 2vV\cos\Theta)^{\frac{1}{2}} \qquad (7)$$

Substituting for ρ(z) and η(z) which are respectively the ion and electron densities yields

$$k(z)dz = \frac{Q(\epsilon)(V^2 + v^2 - 2Vv\cos\Theta)^{\frac{1}{2}}\ i(z)j(z)dz}{Ne^2Vv\sin\Theta} \qquad (8)$$

8

Figure 2

Schematic Illustrating Crossed Beam Ion-Electron Experiment
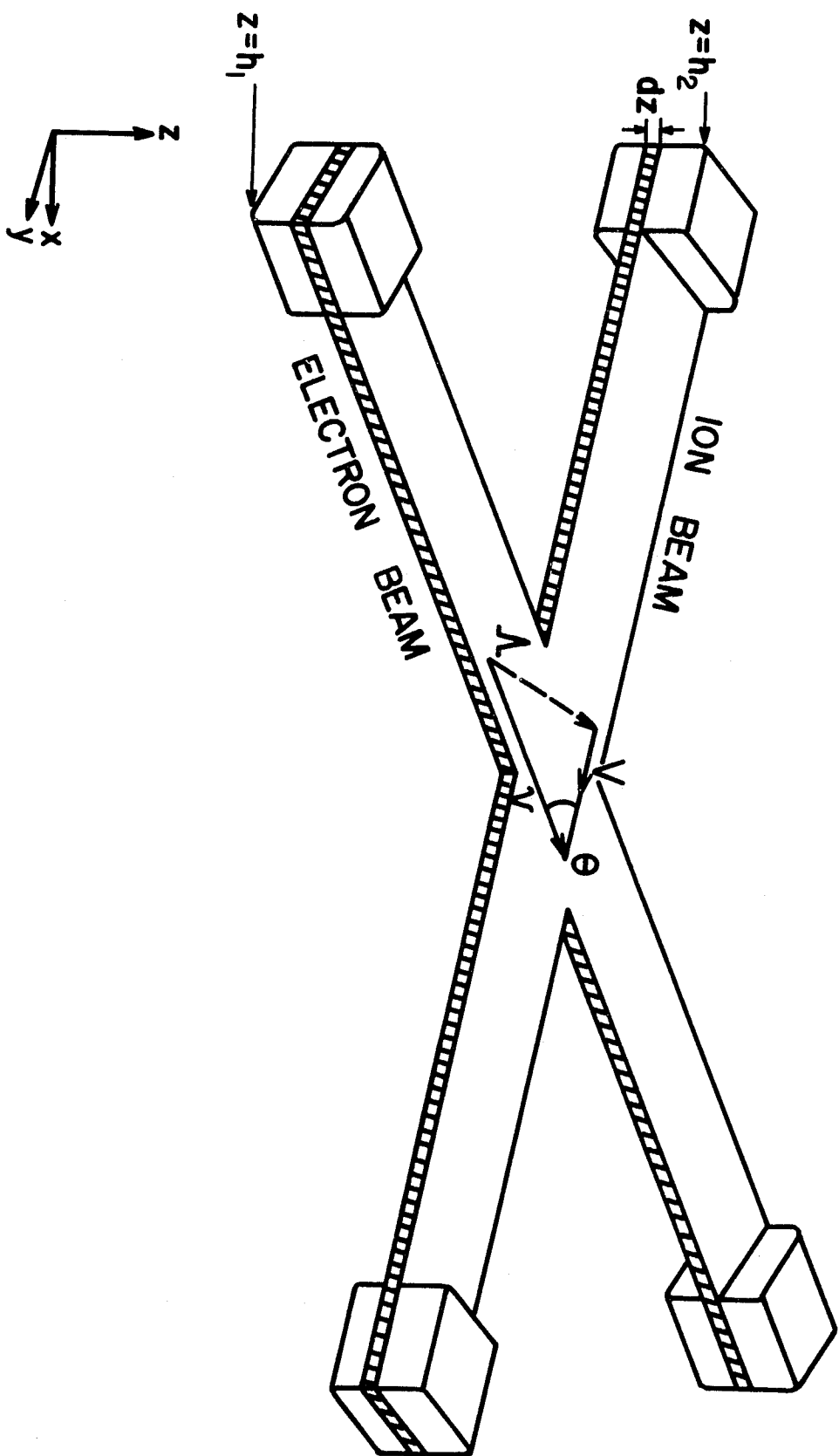
Figure 2A

Vector Diagram for Ion-Electron Crossed Beam Experiment at
90° Collision Angle

ION BEAM

V

θ

v
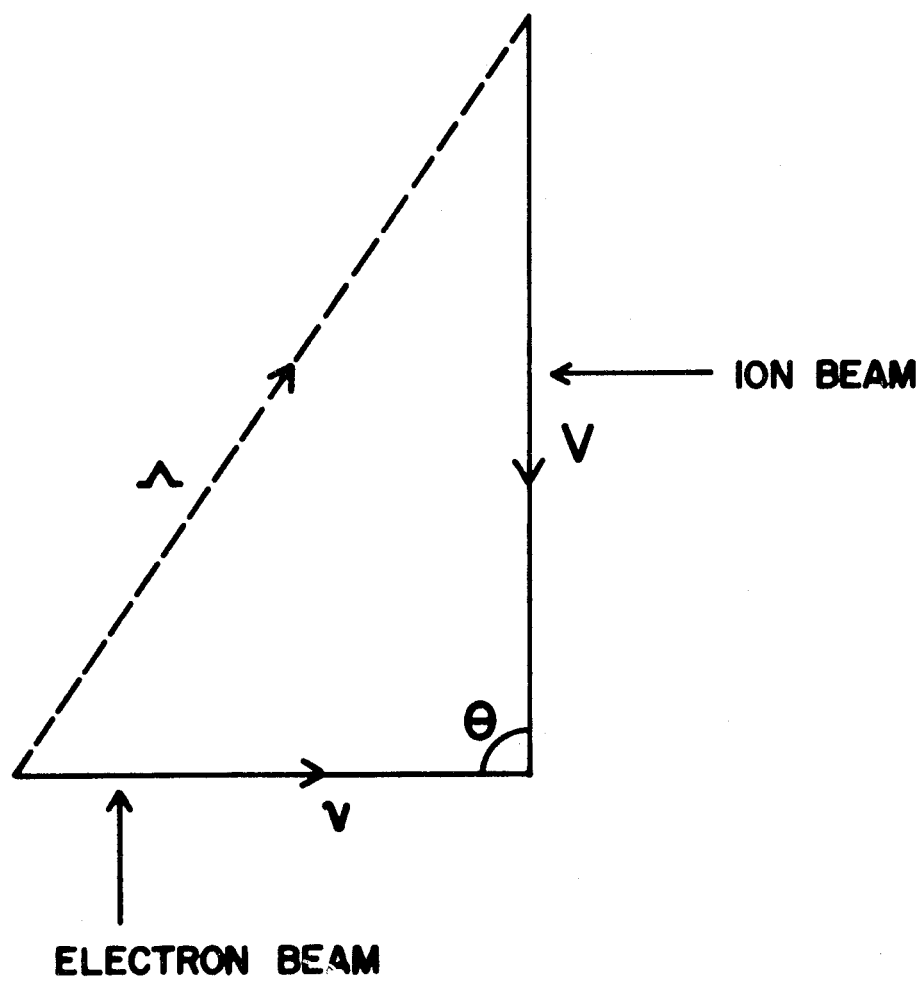
ELECTRON BEAM

where $i(z)dz$ represents the current of parent ions of charge Ne passing through the height element dz and width $\omega(z)$; $j(z)dz$ represents the corresponding electron beam current in element of width $\ell(z)$. The total collision rate K is found by integrating between the spatial limits of the beam, i.e., from $z = h_1$ to $z = h_2$.

For a crossed beam experiment, where the beams interact at 90°, the cross section is given by

$$Q(\varepsilon) = \frac{Ne^2 \, Vv \, K \, h'}{(V^2 + v^2)^{\frac{1}{2}} \, IJ} \tag{9}$$

where I and J are the total currents of ions and electrons; h' is referred to as an effective height of the beams and is given by

$$h' = \frac{\int_{h_1}^{h_2} i(z)dz \, \int_{h_1}^{h_2} j(z)dz}{\int_{h_1}^{h_2} i(z)j(z)dz} \tag{10}$$

The beam investigations thus far have been limited in detection technique to either surface ionization or secondary emission caused by the fast neutrals impinging on an electron multiplier. The optimum detector would be a mass analyzer equipped with a highly efficient ionizer so that neutral particles can be re-ionized and positively identified. The observations could then be extended to polyatomic molecular ions and their recombination energetics.

The total signal observed, thus, depends on

    (a)   ion beam and electron beam intensities; they

            should be as intense as possible at low inter-

            action energies since the recombination cross

section falls off rapidly with interaction
energy.

(b) ionization efficiency of the mass analyzer's
    ion source, i.e., about 0.1% for thermal
    neutrals.

(c) total efficiency of the detector train;
    including electron multiplier gain and pre-
    amplifier characteristics.

The angular distribution of products is determined by the internal
energy released upon decomposition and the translational velocity of the
ion at the instant of neutralization. If fragmentation occurs with the
elimination of light atoms such as hydrogen or deuterium from a relatively
massive molecule, the angular distribution of heavy products will be
small (~10°). On the other hand, if the molecule fragments into particles
of almost equal mass, the maximum dispersion will be greater (~20°) which
correspondingly lessens the intensity. If preferred energy states are
involved then these will be reflected in the angular distribution, i.e.,
small total dispersion angles.

Thus from product identification and angular distribution, information
relating to the mechanism of decomposition can be obtained, i.e., whether
two H atoms or an H_2 molecule are ejected, whether specific electronic
states are involved and how much excess energy is contained in the neutral
products.

III. EXPERIMENTAL

The apparatus employed in this investigation is composed of (1) a
primary, high-intensity ion source with appropriate extraction and focusing

12

elements, (2) a Wien velocity filter which can function as either a mass filter or focusing element, (3) a deceleration lens system, (4) an electron gun producing high-density, low-energy electrons and coupled with electrostatic post-neutralizer deflection plates, (5) the detector train consisting of a high-efficiency ionizer, spherical deflector, quadrupole mass filter, electron multiplier and electronic equipment sufficiently sensitive to detect low, pulsed signal levels, and (6) the vacuum environment, housing and interfacing the above components. Each segment of the instrument as outlined will be described in relevant detail within the following sections of this chapter.

A.   The Primary Ion Source (15)

The ion source used to generate a well-defined high-intensity primary beam is classified as a discharge source by nature of operation (16). It consists of a boron nitride or ceramic (Aremco 1100) housing, anode, tungsten filament material and interfacing electrical feedthrough/gas inlet flange. It was noted that ion source pressures of 100 microns or above were sufficient to produce strong currents. The source is illustrated in Figure 3. A stainless steel water-jacket provides the necessary cooling. Power requirements for the tungsten filaments are:

      (a)   filament: 15V - 20A D.C. for 0.020" wire

                          15V - 12A D.C. for 0.015" wire

      (b)   anode: 0-1000V D.C.

Typical operating pressures depending on the species studied varied from approximately 25-200 microns as measured by a Norton (NRC) 531 thermocouple gauge and monitored on a Norton 804-A five station controller. Gas loads were controlled by a Granville Phillips variable leak which was gently heated by wrapping with heating tape to retard condensation.

Figure 3

Schematic of Discharge Ion Source

A.   Boron nitride housing

B.   Tantalum anode

C.   Boron nitride cap

D.   Tungsten filament

E.   Tantalum filament supports

F.   Gas inlet
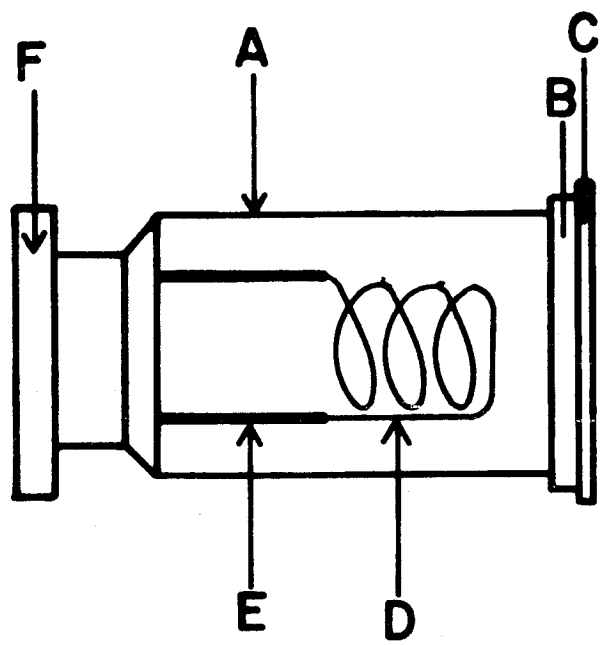
It was noted that with all species observed the source had two output ranges, one at low and one at high pressure. Ion currents with polyatomic species such as CH_4 were observed to range from ~25 µamps at the anode exit to ~5 µamps upon entry of the Wien filter and to 10^{-7} amps at the beam flag located immediately prior to the neutralizer entrance. These currents were observed for 200V ions and were somewhat stronger for beams of N_2^+ ions. The anode aperture can also be varied from a diameter of 20 mils to 60 mils for beam intensity enhancement. All gases were commercially available reagent grade obtained from Matheson. A Keithley 610 CR electrometer was used to monitor beam intensity along the beam path before and after each experimental procedure. Beam stability was observed to be a function of pressure, filament temperature and initiation period at constant anode potentials. It was usually allowed to stabilize over a period of several hours.

The extraction and focusing system consists of three elements — one extraction cup and two cylindrical lenses. The cup and last focusing element are maintained at ground potential; the ion source potential is kept at positive acceleration potential. The first cylindrical focusing element is electrically isolated and operated at a potential between that of the ion source and extraction cup. Figure 4 illustrates the lens system.

Focusing voltages are obtained from a Kepco, ABC 1000, power supply with appropriate divider circuit (17). The focusing voltage is about 2/3 the acceleration voltage and the extraction field strength between the ion source and extraction cup is maintained at 1-5 Kv/cm. For low ion energies, a small extraction washer can be mounted on the cup to decrease the distance between the source exit and extractor.

Figure 4

Schematic of Extraction Lens System

A.   Extractor

B.   Einsel lens (focusing)

C.   Ground potential lens

D.   Stainless steel lens mount

BEAM PATH →

A

B

C D
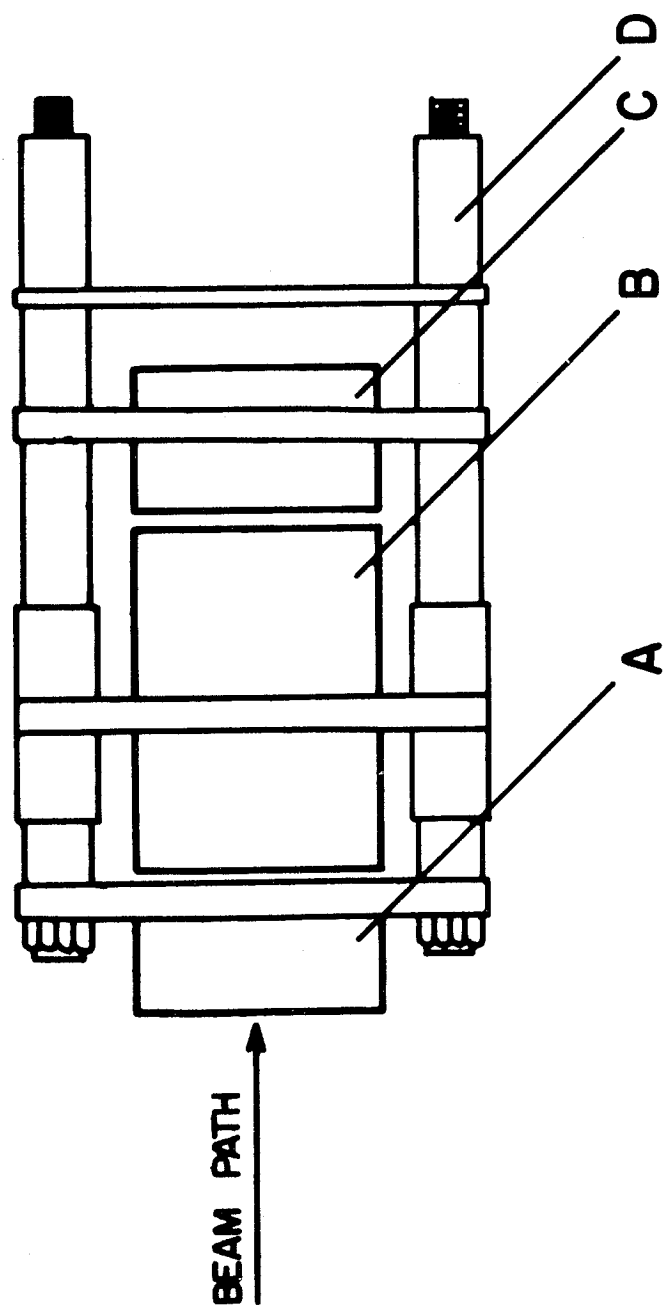
B.   The Wien Filter

The Wien filter described by Wahlin (18) and used for some time in ion-molecule beam experiments (19) consists essentially of a magnet and a pair of electrostatic deflection plates. Figures 5 and 6 illustrate its construction. The electrostatic plates are mounted between the magnet poles which produces an electric field E perpendicular to the magnetic field B.

When a beam of charged particles enters the filter with a velocity v, it will be deflected by the electrostatic and magnetic fields but in different directions. The magnitude of both these bending forces is given by the equations

$$\text{Magnetic force:} \quad F_M = Be\ v \tag{11}$$

$$\text{Electrostatic force:} \quad F_E = Ee \tag{12}$$

where B is the magnetic field strength; E is the electric field strength and e is the particle charge.

When the two opposing forces are equal,

$$Be\ v = Ee \tag{13}$$

then the particles with velocity v_o pass undeflected through the filter. Particles having different velocities are deflected on either side of and dispersed downstream from the filter.

In this experiment the beam is accelerated across a constant electric potential before entering the filter. The velocity of each ionic species in the beam is given by

$$v = \sqrt{2eV/m} \tag{14}$$

17

Figure 5

Schematic of Wien Filter

A. Magnet elements

B. Electrostatic deflection plates
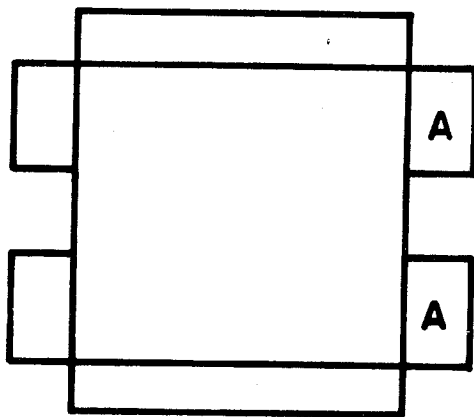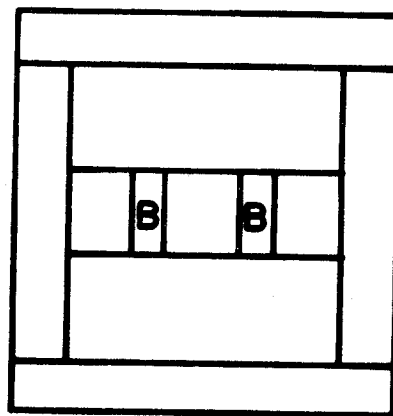
SIDE VIEW   FRONT VIEW

Figure 6

Schematic of The Wien Filter Indicating Magnetic and Electric Fields

        A.   Electrostatic plates

        C.   Magnet elements

$$v = \sqrt{\frac{2eV}{M}}$$

BEAM

+

−

A

TOP VIEW

C

N

+

−

⊗

BEAM

S
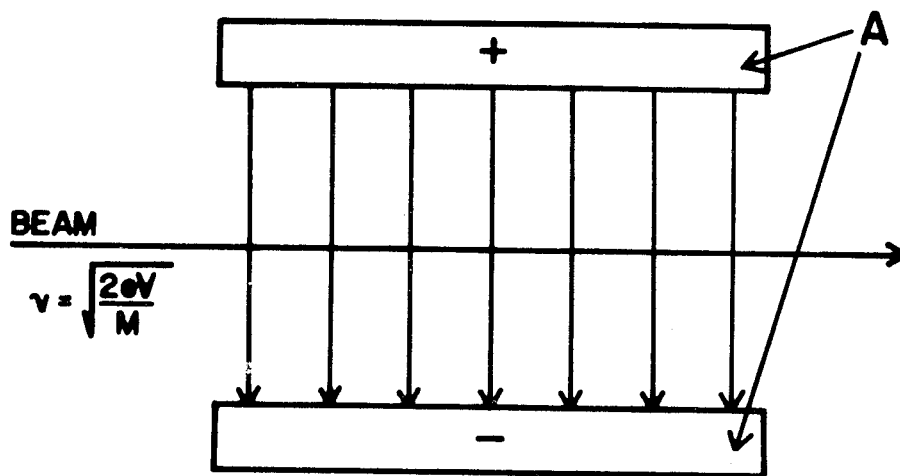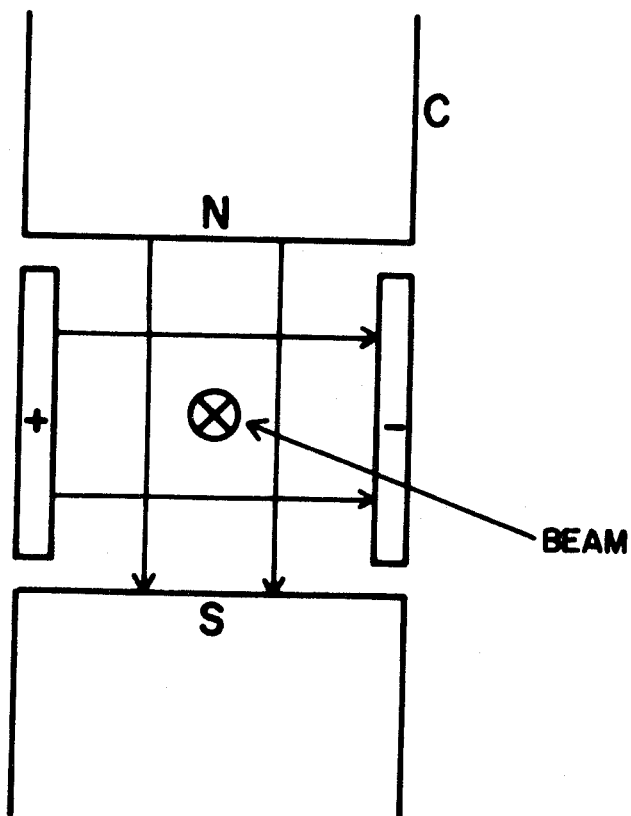
BEAM ENTRANCE VIEW

where m is the mass of the species. Thus different masses will be separated by the filter since each has a different velocity.

This type of filter was used in early ion-molecule beam reaction studies and has the following experimental advantages:

(a)   it is a straight line system.

(b)   the dispersion is adjustable.

(c)   its size is small, i.e., up to about 50 times smaller in weight and size when compared to the sector magnetic analyzer.

(d)   it will select v_o for both positive and negative ions simultaneously.

The Wien filter can also be used as a focusing element by adjustment of one or two guard ring potentiometers. It is actually this strong focusing property of the filter which has caused it to be little used since this limits the length of the drift path between the filter and target. The drift path magnifies the mass or velocity dispersion at the target.

The dispersion capability of the filter is determined by the following formula:

$$D = \frac{\ell \cdot a}{4} \cdot \frac{E}{V} \cdot \frac{\Delta m}{m} \tag{15}$$

and $m = 2 \, e \, v \left(\frac{B}{E}\right)^2$

where

D is the dispersion between masses m and (m − Δm).

m is the mass passing through the filter undeflected and collected as the center mass on the target.

20

ℓ is the distance from the center of the filter to the target (drift space).

a is the filter length.

E is the electric field strength.

V is the acceleration voltage or ion energy.

B is the magnetic field strength.

e is the ionic charge.

$m/\Delta m$ is the maximum resolution; Δm is the full width at half maximum intensity.

The Wien filter used in this project has the following specifications:

a = 0.076 m (3.00 in)

E = approximately 12500 V/m at a maximum plate voltage of 225V

V = 10 eV - 2 K eV

B = 750 gauss

$m/\Delta m$ = approximately 200

Magnet power = 30 watts

Beam aperture = 0.75" x 0.75"

Weight: approximately 12 lbs

The filter is designed for vacuum systems up to 10^{-7} torr. Parts are made of stainless steel, soft iron, teflon and alumina. The magnet coils are wound with 180°C magnet wire impregnated with Dow Corning 996 varnish suitable for ultra-high vacuum. The coils are wrapped with teflon tape.

C. The Deceleration Lens System

The deceleration system consists basically of six concentric cylinders contained in a vacuum casing. Each element is electrically insulated and connected to a ceramic feedthrough. The unit can be baked to 225°C. Figure 7 illustrates the system.

Figure 7

Schematic of Deceleration Lens System

A. Entrance guard ring

B. Lens 2 ⎱
             ⎰ deceleration step 1
C. Lens 3 ⎱
             ⎰ deceleration step 2
D. Lens 4

E. Einsel lens (focusing)

F. Lens 6 (variable potential)

G. Beam entrance
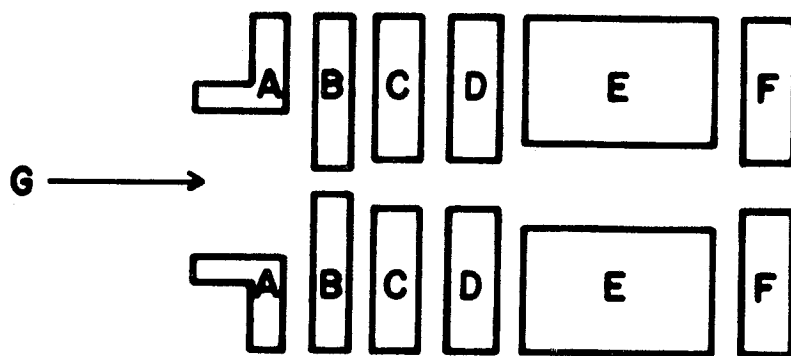
Element 1 is the entrance guard ring and is usually maintained at the same potential as the undecelerated beam. Element 2 is at the same potential as 1. In theory, the operation of the unit using, for example, a 200 eV beam decelerated to 1 eV is as follows:

$$V_{in}/V_{out} = 200 \qquad (16)$$

After the beam passes through element 2 it is decelerated in two steps in the regions between elements 2 and 3, and 3 and 4, respectively. The voltage ratio for each step is

$$V_{in}/V_{out} = 14 \qquad (17)$$

Element 5 is an einsel lens and has the function of refocusing the beam, which is widely diverged upon leaving element 4.

The decelerator is designed to operate over an energy range of approximately 0-1 K eV and decelerates beams to 1/200 (18) of their original energy. It is bakeable to 250°C and weights about 2 1/2 lbs.

D. The Neutralizer

The electron gun, or neutralizer as it will be designated in this section, was designed to meet three requirements.

(1) It should produce a very high output of electrons to assure a high neutral flux.

(2) The electrons should be low energy electrons so that the neutrals will not be highly energetic. Also, recombination is favored at low energies.

(3) The physical dimensions should be reasonably short so that the decomposition kinematics can be investigated.

The initial calculations of neutral flux were based upon a configuration similar to the one described by Weiss (20). The neutralizer is essentially a planar diode with the grid located in close proximity to the cathode. The anode and grid are held at the same potential. Spangenberg (21) discussed this configuration and points our its similarity to beam power tubes.

The current drawn from the cathode into the grid-anode region will increase until space charge limited conditions are achieved. The current density is then represented mathematically by the Child-Langmuir law (22). This relationship is given below.

$$J = \frac{8 \ A^2 \ V^{3/2}}{d^2} \tag{18}$$

where J = current density in amperes unit area

A = area of emitting surface

V = extraction potential

d = distance between the cathode and grid-anode region.

Weiss points out that electrons injected into the grid-anode region in which both the grid and anode are at the same potential V can produce space charge limited conditions but having a potential below the applied anode potential. He calculates this potential as being approximately one-quarter (V/4) of that measured on the anode. This should significantly favor recombination since V can be increased to obtain high current density but due to the potential minimum the electrons remain "slow". Figure 8 illustrates the potential minimum and Figure 9 the neutralizer configuration. For a given emitter area and distance between the cathode and the grid-anode region, a plot of emission current versus applied anode

24

Figure 8

Space Charge Limited Potential Energy Minimum between Anode and Grid
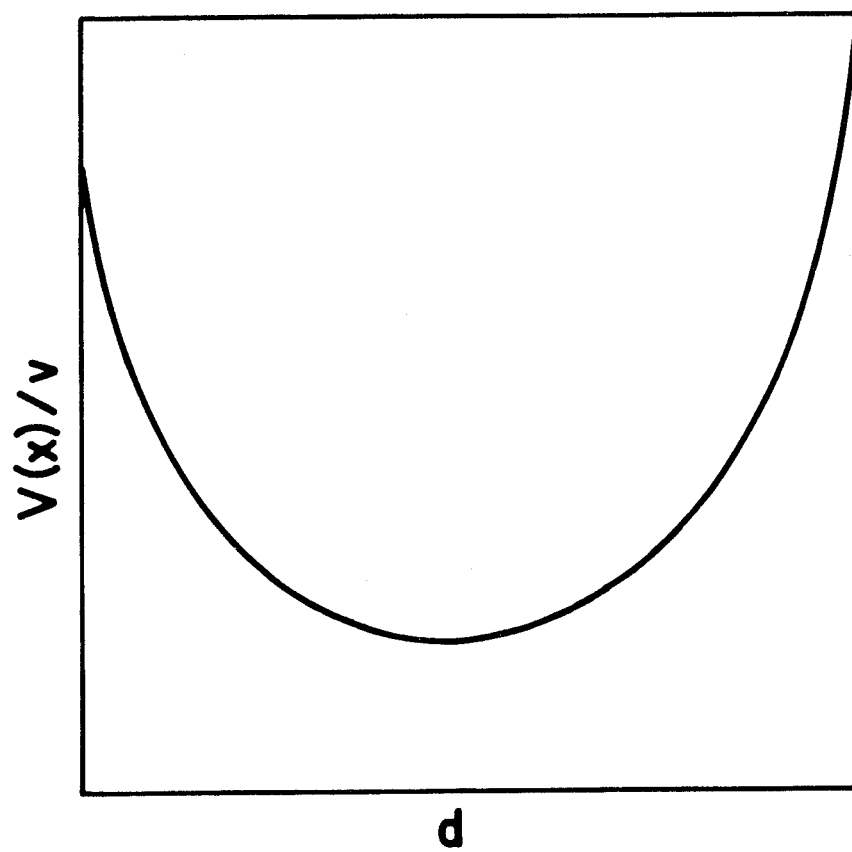
Figure 9

Schematic of Electron Gun

A. Anode

B. Grid

C. Chopping grid

D. Cathode on molybdenum support

E. Ion beam entrance

F. Deflection plate (ground potential)

G. Deflection plate (negative potential)

H. Molybdenum main support

I. Filaments

A

E

B

C

D

H

G

F

I
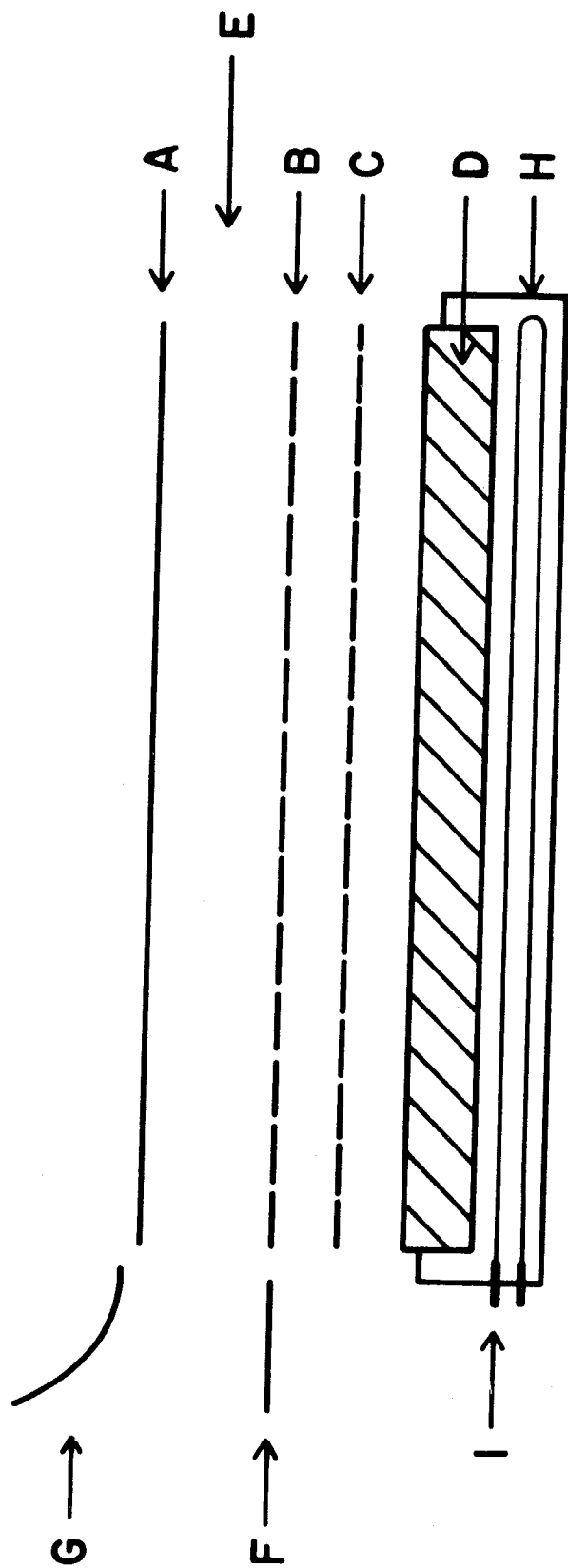
potential should give a slope of 0.667 according to Equation (18).
Figure 10 illustrates the performance of a fully activated cathode.
From these data it can be seen that space charge limited conditions are
reached over a wide range of extraction potentials. Only the low energy
portion of this plot, however, would indicate the useful current for
recombination.

A second grid was added to the gun in order to gate or chop the
electron beam for purposes of distinguishing background neutrals from
signal neutrals. The passage of an ion beam through the background gas
can result in ion-molecule reactions and these will produce neutrals
which can interfere with the neutral particle detection resulting from
the recombination reaction. Most ion-molecule reactions have rate
constants in the order of 10^{-9} cc/molecule sec as indicated by Lampe
et al. (23). Some of these exhibit a decline in the rate constant with
increasing relative velocity of ion and molecule. For an energy range
of ~10 eV some rates would not be affected and some would become negli-
gible. If we take an ion velocity of 5.5×10^5 cm/sec, the cross section
for ion-molecule reaction will be about 2×10^{-15} cm^2

$$n_{IM} \approx I_o \, \sigma \times [M] = 2 \times 10^9 \text{ neutrals/sec} \tag{19}$$

where the length of travel for the ion beam is taken as 5 cm and the
density of background gas as 4×10^9/cc (equivalent to a pressure of 10^{-7}
torr).

Also, a major competing process with recombination is charge exchange.
The rate of neutral production from charge exchange is proportional to
the ion beam intensity and background gas pressure. Since the ion beam
current is constant, this process is not coherent with modulation of the

27

Figure 10

Cathode Emission Current vs Applied Anode Potential
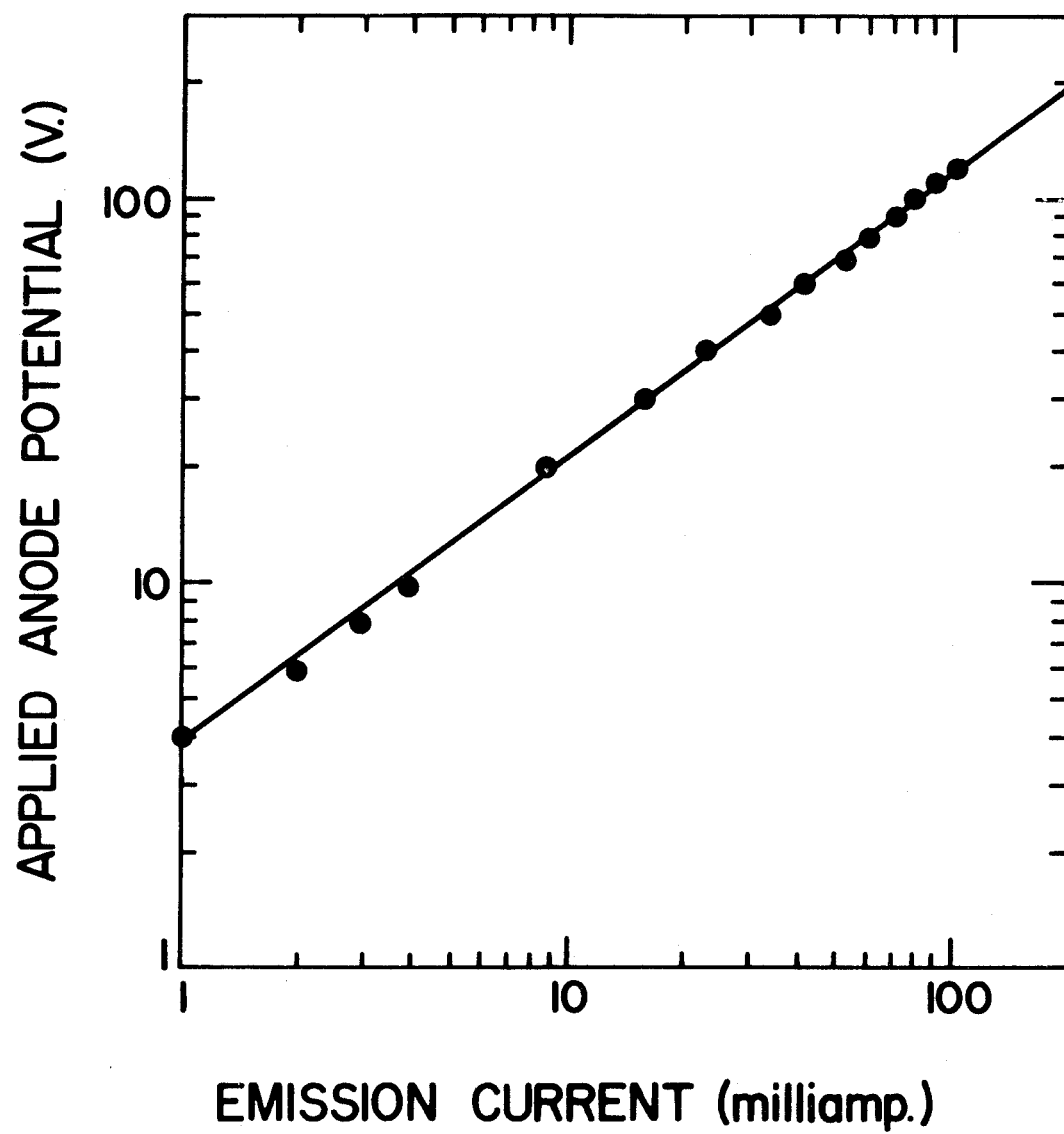
electron beam. This process of modulating the electron beam but holding the ion beam constant is illustrated in Figure 11. The chopping gate is provided by a Wavetek VCG, Model III, pulse generator.

The cathode used for high current density production was a Phillips type A impregnated cathode. The cathode described in Reference (24) consists of a porous tungsten surface impregnated with barium, calcium and strontium carbonates. This surface is brazed to a molybdenum body. Upon activation, a mono-molecular layer of barium is formed on the cathode surface and emission results. Figure 12 illustrates the cathode used in this experiment.

The neutralizer sits on an aluminum pillar block, adjusted and aligned for ion beam penetration centered between the grid and anode region. The cathode is housed in a molybdenum frame and 0.010" tantalum foil heat shields are placed between it and the frame. The chopping grid support is also molybdenum with 90% transparency tungsten mesh spot-welded to its surface. The interaction region grid support is 304 stain-less with 90% transparency tungsten mesh similarly spot-welded to it. The reaction region anode was constructed from molybdenum.

Ceramic insulators used between the neutralizer elements and also as filament supports were constructed from Aremco 1100 machinable ceramic and fired at 1400°C afterward. The cathode was indirectly heated by four 0.010" tungsten filaments powered by a Kepco KS36-5M supply. Typical operating conditions for the filament assembly were 18V at 5 amps.

The cathode was initially activated over a period of 24 hours by raising its temperature to near operating condition and letting it remain at this temperature with 20 volts extraction potential on the chopping grid. After activation the cathode is very resistant to contamination by

29

Figure 11

Schematic of Pulsed Signal and Background Phases

BACKGROUND

SIGNAL

e^-

TIME (millisec.)
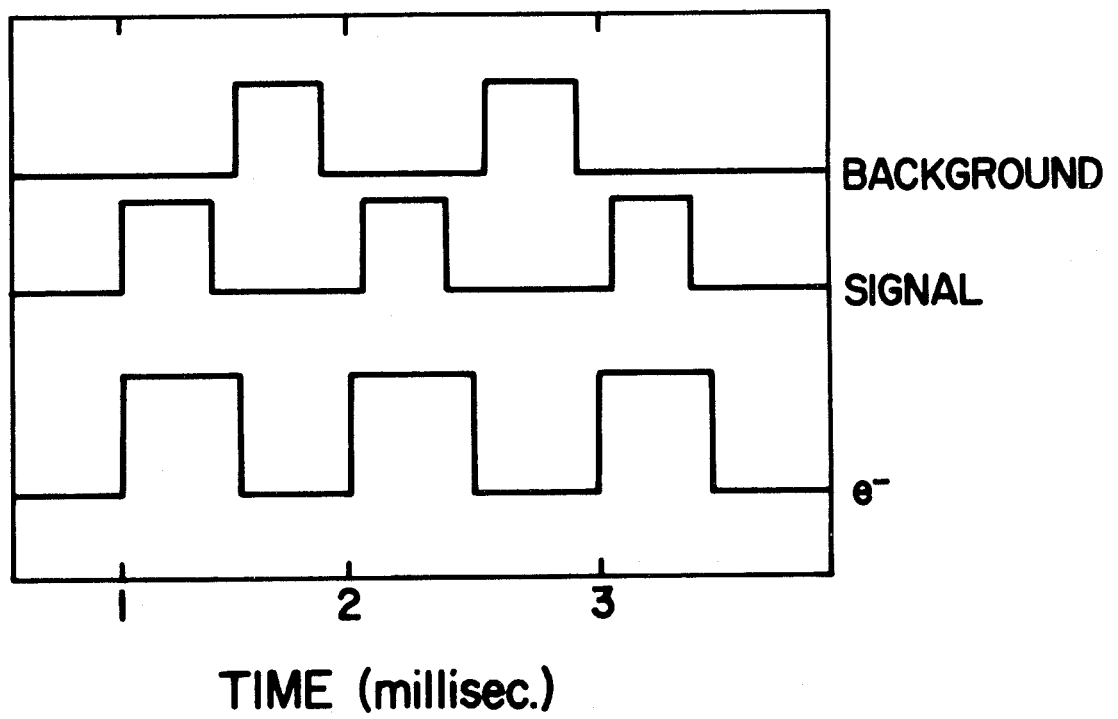
Figure 12

Schematic of Phillips Cathode

(dimensions given in inches)

A.   Molybdenum support

B.   Tungsten cathode (Phillips type A impregnant)

1.640

0.418

TOP VIEW

B

0.166

A
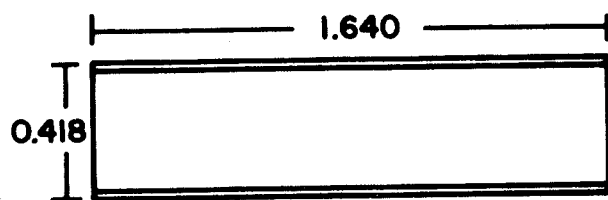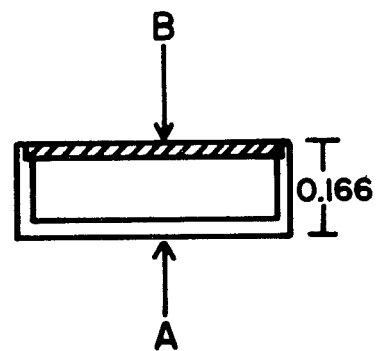
END VIEW

exposure to atmosphere. The same cathode was employed for a one-year period during development before replacement was necessary.

Immediately following the interaction region and mounted on the neutralizer support block are two deflection plates. These were made from 304 stainless steel and are maintained at a potential high enough to deflect the unneutralized portion of the primary ion beam. The deflection voltage is dependent on the initial energy of the primary beam and determined experimentally for each set of conditions. Deflection voltages were determined by monitoring the primary ion beam with a Keithley Model 610 CR electrometer.

E.   The Detector

The detector consists of the following components, each of which will be described in detail:

   (a)   High efficiency ionizer.

   (b)   Spherical deflector.

   (c)   Quadrupole mass filter fitted with a Bendix

          Model 306 magnetic electron multiplier.

   (d)   Both a Keithley 610 CR electrometer and

          Ortec pulse counting equipment.

   (a)   The High Efficiency Ion Source

In an experiment of this nature where the total number density of recombination neutrals would be considered very adequate for detection as charged particles, the critical parameter is the ionization efficiency of the detector train. Efficiencies on the order of ~0.1% are considered good when extraction optics, usable emission current and ionizer geometry are taken into account.

The ionizer used in this research was obtained from Extranuclear Laboratories, Inc., Pittsburgh, Pennsylvania, Model 041-1. It has an efficiency of approximately 0.1% for thermal energy N_2 beams as reported in Reference (25). The ionizer is illustrated in Figure 13.

In the operation of an ion gun used to obtain strong ion intensities, the ion region geometry is an important consideration. The neutral beam enters the Model 041-1 ionizer and passes along the axis of a cylindrical grid which accelerates electrons toward this axis from four filaments surrounding the grid in the form of a square (also shown in Figure 13). This geometry creates four crossing electron beams for maximum interaction between electrons and the neutral beam. Tungsten wire, 0.010" in diameter, is used for filament material. Emission currents range from zero to 50 milliamperes at 100 volts electron energy. Extranuclear Laboratories (26) indicate that at high emission current levels, a quasi-plasma is built up in the ionizer and ion-space charge dominates over electron space-charge. Ion-space charge is thus a significant factor in gaining high ionization efficiencies.

The ion optics include a lens which acts as an electron barrier. Without such a barrier, the electrons from the ionizing beam are capable of scattering from residual gas and traveling along the mass filter during the time in each RF cycle when the field inside the filter approaches zero. If this occurs, the electrons can ionize residual gases at the exit end of the quadrupole immediately before the ion detector producing untunable noise throughout the mass spectrum. The electron barrier prevents this from occurring and results in an improved signal to noise ratio.

The ionizer operating conditions for the experiment described herein are

Figure 13

Schematic of High Efficiency Ionizer

A.   Filament shield

B.   Ion region grid

C.   Extractor

D.   Lens 1

E.   Lens plate

F.   Lens 2

G.   Lens 3
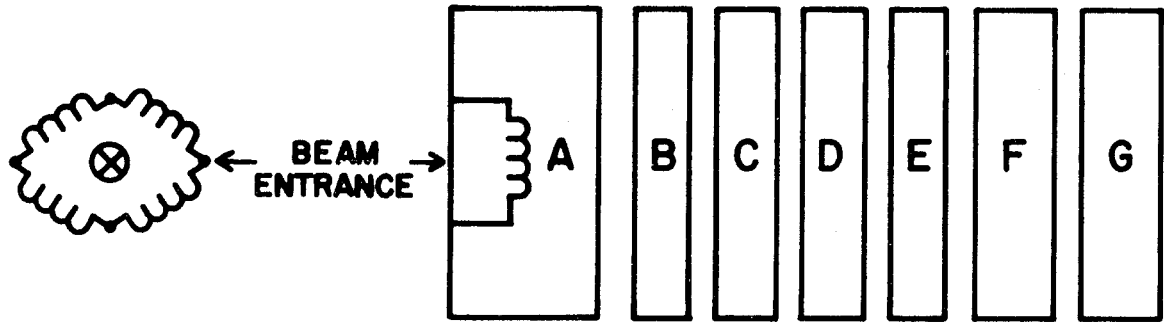
END VIEW   SIDE VIEW

(1) Emission current: 30-40 ma

(2) Electron energy: 100 V

(3) Ion energy: 0 V

(4) Lens 1: -440 V

   Lens 2: 0

   Lens 3: -172 V

(5) Extractor: -10 V

(b) The Spherical Deflector

The spherical deflector described by Wollnik (27) and Duckworth (28) was built to minimize untunable noise due to

(a) photons

(b) metastable neutrals formed in the ionizer

(c) neutrals accompanying the primary beam and subject to ionization.

The deflector was constructed from 304 stainless steel and is illustrated in Figure 14. In theory, this element is used only for transmission of the ion beam and not for focusing. The path indicated by the radius a_e actually describes a surface of zero potential. Thus, a beam passing along this path should not be subject to focusing effects. The entrance and exit slits, however, determine resolution and contribute an energy dispersion effect on the transmitted particles.

This deflection system can be briefly outlined mathematically as follows:

From Coulombs law

$$E = \frac{K}{a_e^2} \tag{20}$$

Figure 14

Schematic of Spherical Deflector

A. Beam path

B. Beam exit defining plates

C. Beam entrance defining plates

D. Spherical deflector

A
↑ BEAM PATH

B

ϕ_e

$-$

a_e

A →
BEAM PATH

D

$+$

C

R_1

R_2
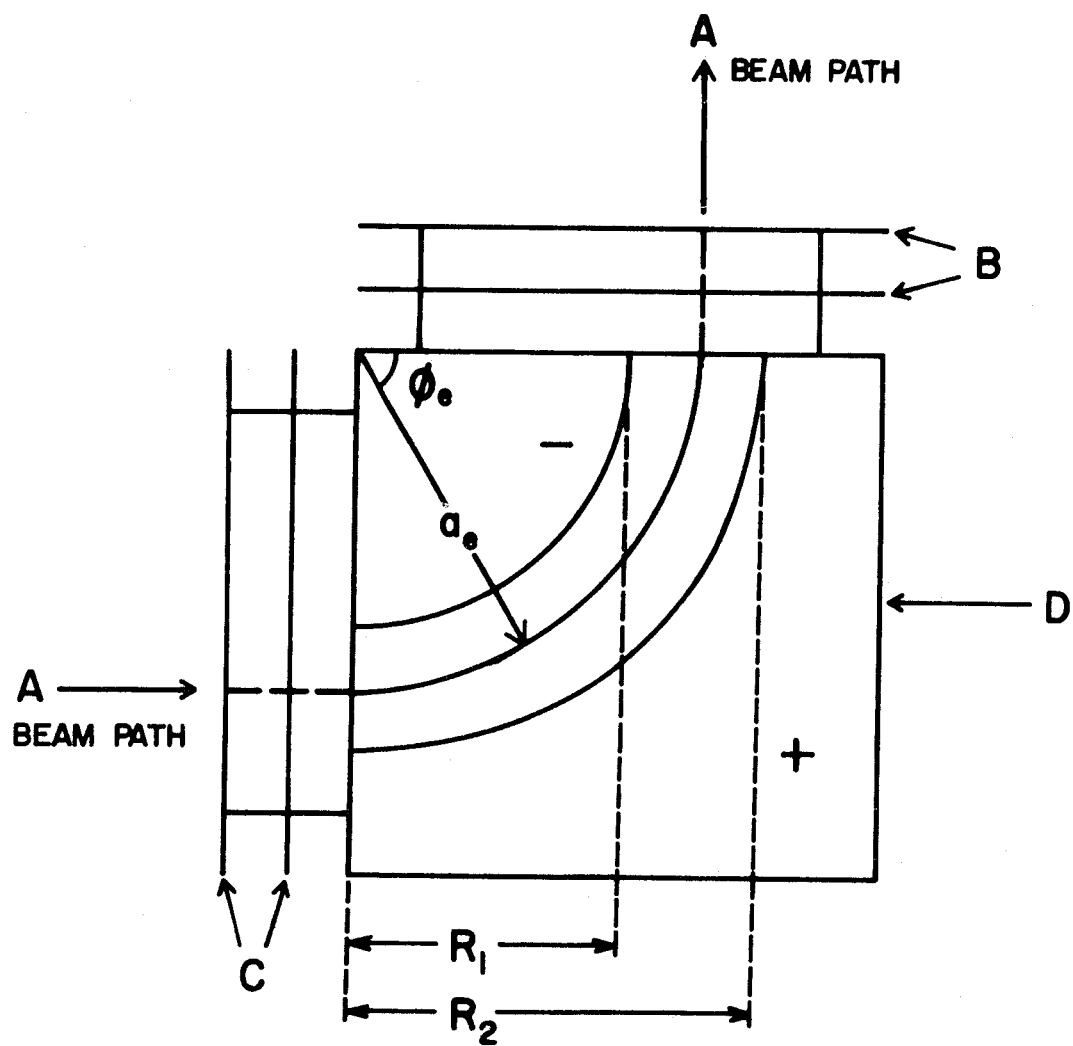
where E is the electric field strength, a_e is
the radius along the zero potential surface and
K is a constant.

$$\Delta V = \int_{R_2}^{R_1} \frac{K \, dR}{R^2} = \frac{K(R_2 - R_1)}{R_2 R_1} \tag{21}$$

where ΔV is the change in potential over the
deflection path. R_1 is the inner deflection
radius and R_2 is the outer deflection limit.

$$E = \frac{K}{a_e^2} = \frac{\Delta V \, R_1 R_2}{a_e^2 (R_2 - R_1)} \tag{22}$$

The ion kinetic energy is given by

$$U = \frac{1}{2} m v^2 \tag{23}$$

where m is the particle mass and v is its velocity.
The centripetal force exerted on the ions moving
through the deflector along a_e is given by

$$E = \frac{m v^2}{a_e} \tag{24}$$

Thus

$$\frac{U}{E} = \frac{a_e}{2} = \frac{K}{2a_e} \tag{25}$$

$$\Delta V = 0.728U \tag{26}$$

Table II gives the dimensional data for the deflector. Figure 15 gives the calibration data experimentally determined for this system. It can be seen that these data compare favorably with the result predicted by Equation (26).

The energy resolution due to the entrance slit is 17.6%. The energy dispersion due to the exit slit is calculated to be 9.2%. Thus, the total resolution is

$$9.2\% \leq Res \leq 26.8\%$$

(c)   The Quadrupole Mass Filter

The quadrupole mass filter was purchased from Extranuclear Laboratories, Inc.; Model 324-9. The theory and design data for such a mass filter are very adequately described in the original work of Paul et al. (29) and more recently in a review concerning mass spectroscopy employing radio frequency quadrupole fields by Dawson and Whetten (30). Thus this dissertation will not attempt to outline this instrument in detail.

Mass spectrometers are generally grouped into two classes: static and dynamic. The latter are based on the time-dependence of one or more parameters of the system. Dynamic instruments can be further subdivided into three categories: energy balance spectrometers (omegatron, r-f linear accelerators), time-of-flight instruments and path stability spectrometers.

The quadrupole is a path stability spectrometer and was chosen for this experiment because of the following characteristics:

(1)   Nearly 100% transmission efficiency for ions obtained
        at low resolution.

Table II

Dimensions of Spherical Deflector

R_1	7/8"
R_2	1-1/4"
a_e	1-1/10"
ϕ_e	90°

Entrance and exit apertures 3/16"

Figure 15

Calibration Curve for Spherical Deflector
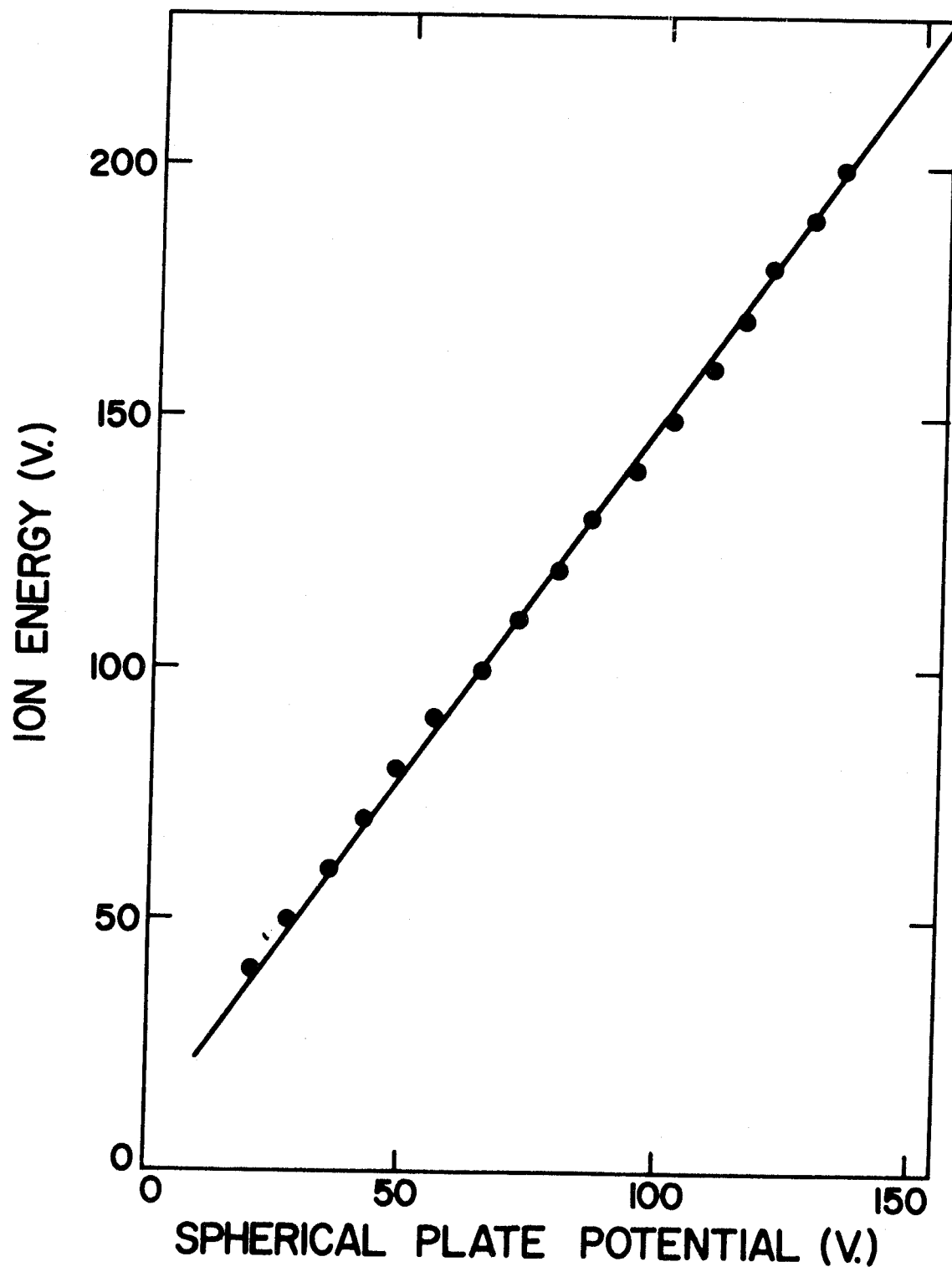
(2) Minimal kinetic-energy discrimination of ions.

(3) Easily variable resolving power.

(4) Absence of stray magnetic fields that could disturb
    the electron-ion recombination region.

(5) The capability of operation at considerable residual
    pressure in the analyzer.

(6) Comparatively small size and ease of installation.

The model 324-9 has rods 8 inches long and 3/4 inches in diameter mounted in a stainless steel jacket 3 inches in diameter. It has an r_o of 0.822 cm and can scan up to mass 254 depending on the head employed. Two heads were employed in the experiment, low range (0-60), Model C and high range (mass 0-254), Model D2. The filter is illustrated in Figure 16. The R.F. and D.C. voltages applied to the rods of the filter and indicated by $\phi/2$. The path stability characteristic of quadrupole instruments is described by the Mathieu equations of motion. Reference (3) gives the derivation of these equations and indicates their relation to the electric fields obtained from the quadrupole potential. Figure 17 illustrates the path stability characteristic of this filter. Each ionic mass entering the quadrupole field has its own R.F./D.C. value for transmission. If the instrument is tuned for this mass then the ions execute harmonic motion of constant amplitude along the entire length of the filter rods. Other species not "tuned in" execute similar motion but with amplitude that increases so rapidly it soon becomes greater than r_o for the filter. These unwanted ions strike the rods before reaching the exit and are thus not detected.

Figure 16

Schematic of Quadrupole Mass Filter
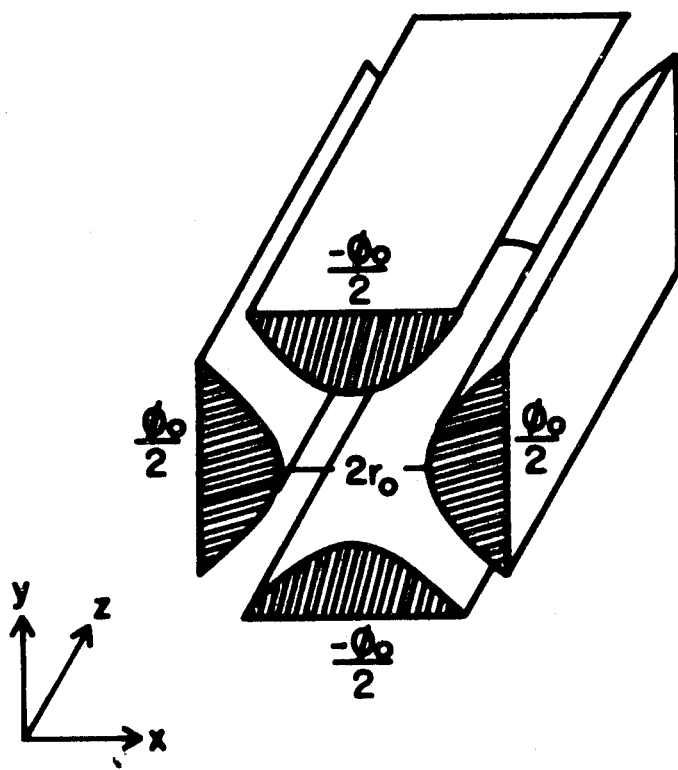
Figure 17

Path Stability Diagram for Quadrupole Mass Filter

        A.   Stable ion path

        B.   Unstable ion path

(A)

X →

Z

(B)

X

r_0

Z
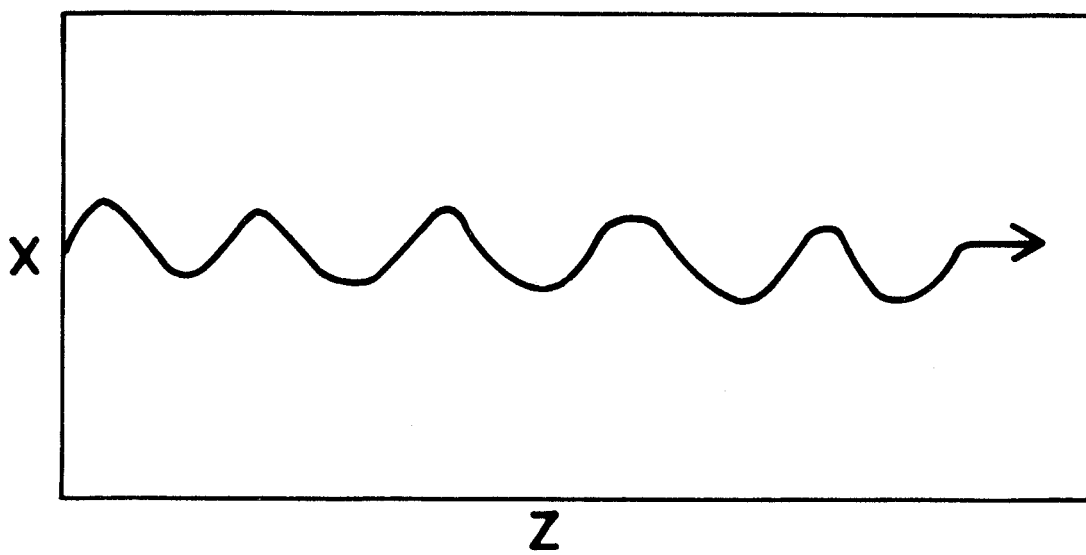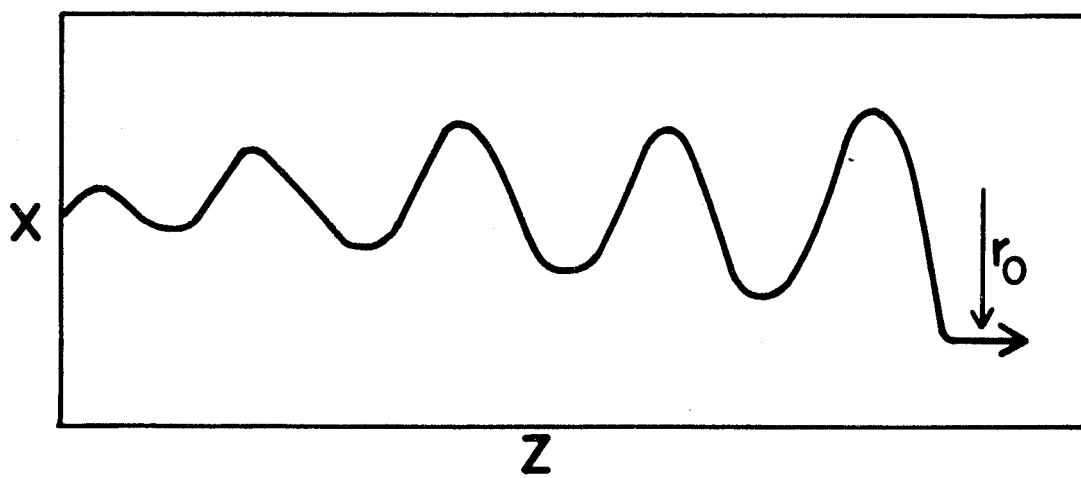
The quadrupole supply system, also obtained from Extranuclear, has the additional feature of the ability to bias the poles in such a manner that the axis of the mass filter is off ground by ±8 volts using an internal D.C. supply and can be biased up to ±400 volts using an external voltage source. This capability permits a mass filter to sample ions from plasmas near ground and also establishes D.C. fields to counteract rejection of desired ions as they pass through the fringe fields upon entering the mass filter.

The mass filter is fitted with a Bendix 306 magnetic electron multiplier. The gain can be varied from $0-10^8$ by adjusting the dynode strip input and field strip input voltages. The entrance grid of the multiplier is made of etched nickel mesh 0.5 mils thick, 100 lines per inch, and having greater than 90% transmission. The multiplier has the advantage of reproducible gain even upon repeated exposures to atmosphere and is described in detail in References (31) and (32). One disadvantage, as pointed out by Reference (33), is that the gain is a function of where the particles of interest strike the cathode. Figure 18 illustrates the basic construction of the multiplier. A Fluke, Model 415B, power supply with appropriate voltage divider network was employed for operation (34).

It was observed during experimental procedure that unless the multiplier was mounted vertically so that the entrance grid is parallel to the beam exiting the mass filter, a certain amount of untunable noise resulted. Since recombination signals are low per se, any noise affecting the signal to noise ratio is undesirable. The vertical mounting configuration included an extractor grid located over the quadrupole exit aperture and a repeller plate opposite the multiplier entrance grid. Figure 19 shows this mounting design.

Figure 18

Schematic of the Bendix M306 Continuous Dynode Electron Multiplier

        A.   Field strip

        B.   Dynode strip

        C.   Incident ion beam

        D.   Cathode

        E.   Magnetic field

A

C

TO ANODE

⊗E

B

D
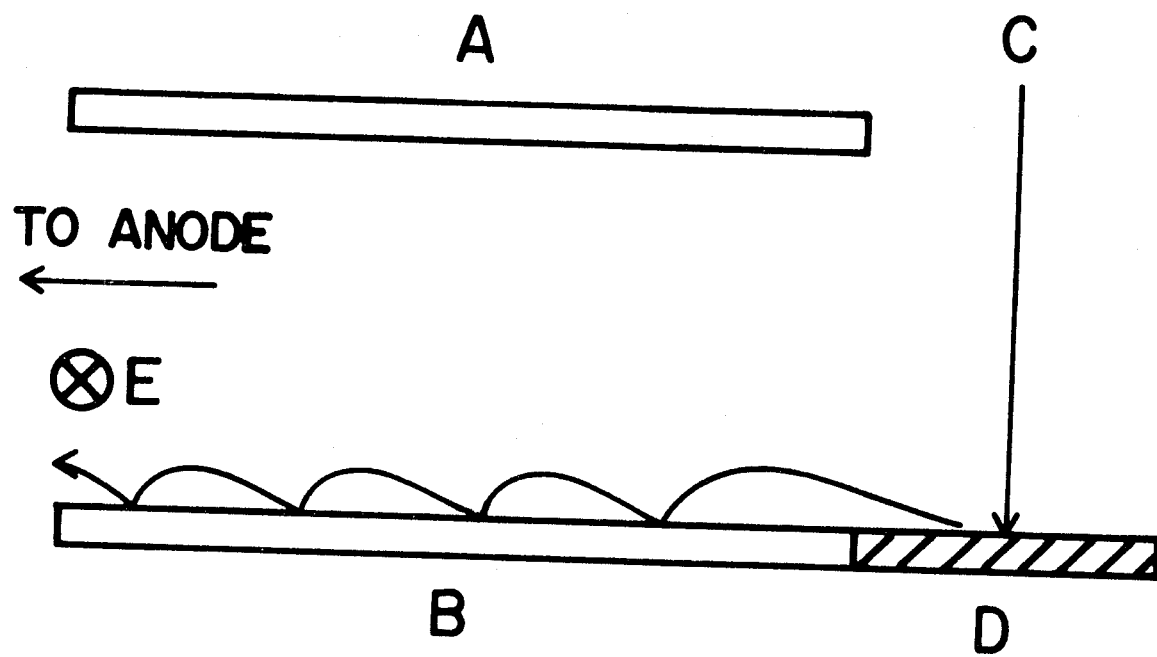
Figure 19

Schematic of Multiplier Mount and Extractor for the

Quadrupole Mass Filter

    A.   Bendix, Model 306, magnetic electron multiplier

    B.   Ion repeller plate

    C.   Ion extraction grid

    D.   Quadrupole mass filter

BEAM PATH
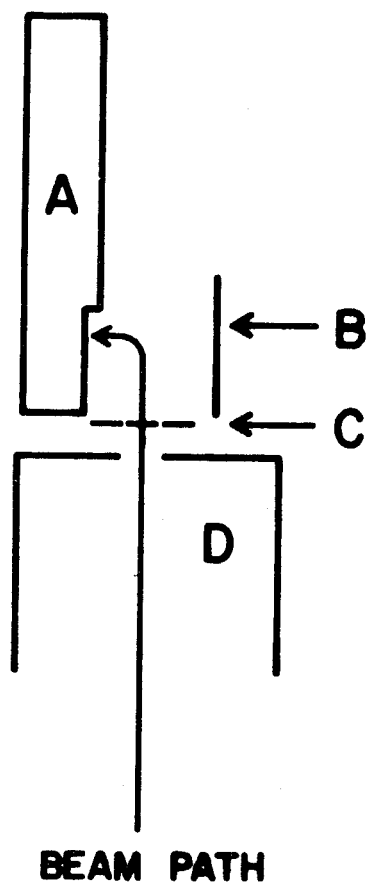
Table III gives typical calibration data for the quadrupole and resolution (m/Δm) for various settings on the resolution indicator. The data in this table show the variation of transmitted ion intensity with increasing resolution. These are necessary because the quadrupole is not calibrated as installed. Resolution is physically set by use of a one-turn potentiometer variable from 0 → 10. R gives the setting on this dial with corresponding experimentally determined resolution. When a certain molecule was under investigation, the procedure was to first look at the mass spectrum of the primary beam for determination of the strongest peaks representing the best possibility for observance of a recombination signal. When actually measuring the neutrals, the quadrupole was initially set at low resolution so a small range of mass numbers could be viewed at maximum possible signal intensity. The resolution was then slowly increased until mass separation for the re-ionized neutrals was achieved. It should be noted at this point that increasing the resolution sufficiently for mass separation sometimes eliminates weaker signals due to the rapid intensity decline with increasing resolution. This point is very important when scanning for the recombination signal.

The mass spectra of the primary ion beam were usually observed from the meter mounted on the quadrupole control chassis. The signal was also displayed on the oscilloscope.

(d) The Counting System

The counting system (34), illustrated in Figure 20, consists of

(1) Ortec, Model 113, preamplifier

(2) Ortec, Model 485, amplifier

47

Table III

Calibration of High-Q Head Model D_2

P_s = 93u

I_c = 2.7×10^{-8}

E/M = 950V

Ion	m/e	I'_c	L.M	R	ΔM	R'
Ar^+	40	9.0×10^{-9}	19.8	4.8	4	20
	40	3.2×10^{-9}	19.0	6.2	4	40
	40	5.0×10^{-9}	19.0	6.7	0	20
	40	2.0×10^{-9}	19.0	7.5	0	40
	40	1.05×10^{-9}	19.0	8.0	0	70

P_s: Source pressure

I_c: Primary ion current monitored on spherical deflector (amps)

E/M: Electron multiplier potential

I'_c: Current monitored from multiplier (amps)

L.M: Setting on low mass dial

R: Setting on resolution dial

ΔM: Setting on ΔM selector

R':   Actual resolution (m/Δm)

Figure 20

Schematic of Beam Chopper Timing Circuitry
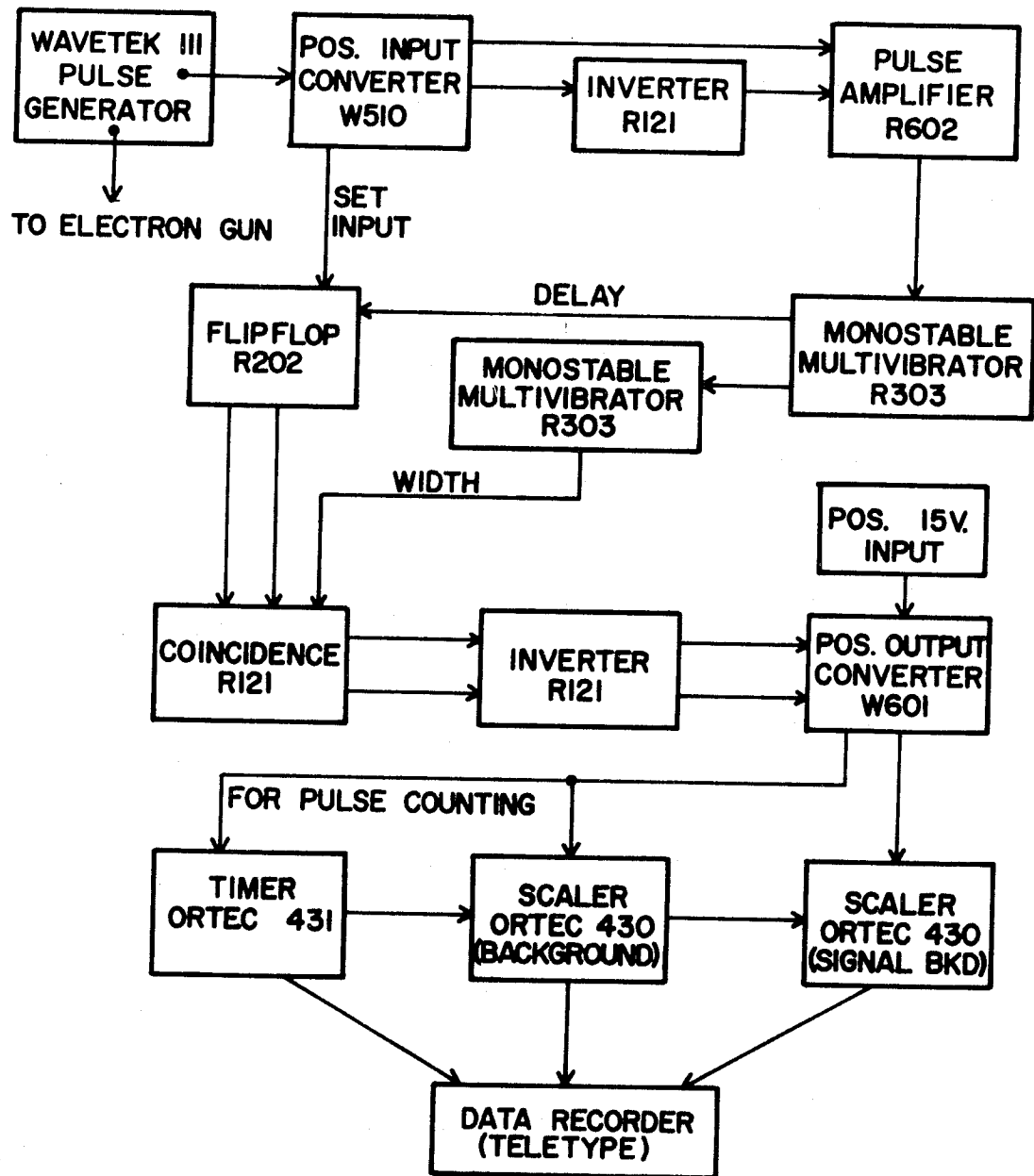
(3) Ortec, Model 431, timer scaler

(4) Ortec, Model 430, scaler (two)

(5) Ortec, Model 441, ratemeter

(6) Ortec, Model 406A, single channel anlayzer

All counting equipment was housed in a standard nuclear instrument module bin and power supply, Ortec, Model 401A. The two scalers were interconnected with the Wavetek, Model III, pulse generator so that total background plus signal counts were recorded on one and total background counts on the other. Timing interface circuitry, illustrated in Figure 20, was purchased from Digital Equipment Corporation.

A Tetronix, Model RM545B, oscilloscope was connected into the detection circuitry for both troubleshooting and observance of normal noise levels during an experimental run. The noise characteristic of the detection circuitry is bucked out by a variable discriminator included in the amplifier. Also, pulse amplitude from signal and background were monitored on the scope during each experimental run.

F.   The Vacuum Environment

The vacuum environment consists of the following elements, each of which will be separately described in this section.

(1) The primary ion source chamber.

(2) The interaction chamber with rotating lid.

(3) The detector chamber.

(4) The pumping system with appropriate protection circuitry.

(1) The primary ion source chamber, illustrated in Figure 21, was constructed from 304 stainless steel. Preformed stainless steel elbows

Figure 21

Schematic of Vacuum Environment

A. Primary beam chamber

B. Main or interaction chamber

C. Detector chamber

D. NRC Orb-ion pump

E. Rotating lid

D

C

E

BEAM PATH

A

B

TO 2" PUMP

TO 6" PUMP
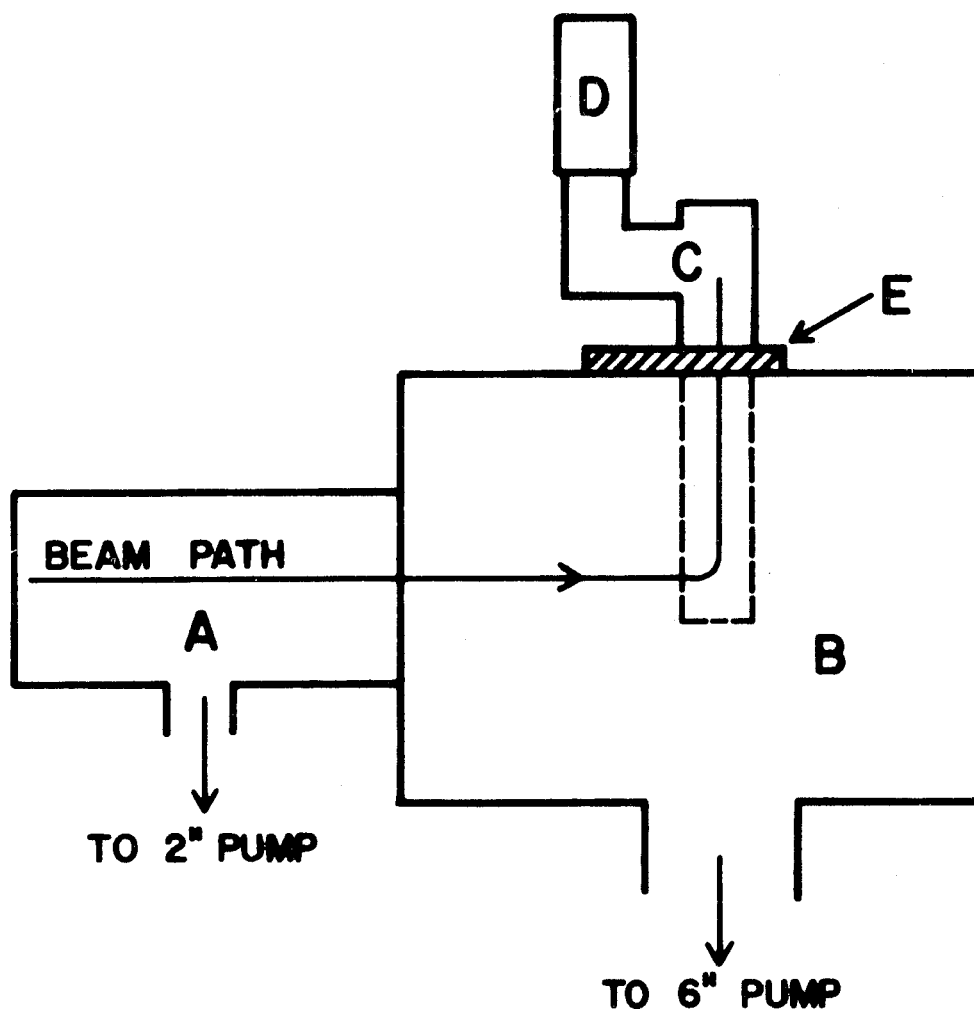
were mated to this chamber to serve as pumping ports. The ion source is located on an aluminum flange machined so that the source properly mates and aligns with the extractor/acceleration lens system. The entire source chamber mates with the interaction chamber and is aligned with the beam path by recess machining into the interface flange.

(2) The interaction chamber, illustrated in Figure 21, was constructed from 6061T aluminum. Each member of the chamber was anodized after machining to harden and protect the surfaces. Stainless steel helicoils were inserted into tapped holes to prevent stripping during normal break-down procedures. The rotating lid, illustrated in Figure 22, was also constructed from aluminum. The bearing was purchased from Kaydon Engineering Corporation (35). Vacuum under rotation was maintained by use of two Tec-Ring seals described by Reference (36).

Pumping ports were machined into the bottom of the chamber before assembly and electrical feedthrough flanges were machined in the removable side flanges after preliminary leak testing of the welded structure.

Buna-N-O-rings are used on all flange seals, except the rotating lid.

(3) The detector chamber, illustrated by Figure 21, was constructed of 304 stainless steel. The entire chamber was positioned on the rotating lid and sealed to it with a buna-N-O-ring. Seals, however, in the detector itself were fabricated from 0.080 inch diameter indium wire.

(4) The Pumping System. The primary ion source chamber was fitted with two NRC HS-2 diffusion pumps, each backed by a Precision D-150 mechanical pump. The interaction chamber was pumped by an NRC VHS-6

Figure 22

Schematic of Rotating Lid Cross Section

A.   Kaydon bearing

B.   Thrust ring for lid and sprocket

C.   Tec-ring seals

D.   Rotating lid

E.   Bearing retaining ring

F.   Aluminum cylinder

B

B

E

A

D

F

C

C
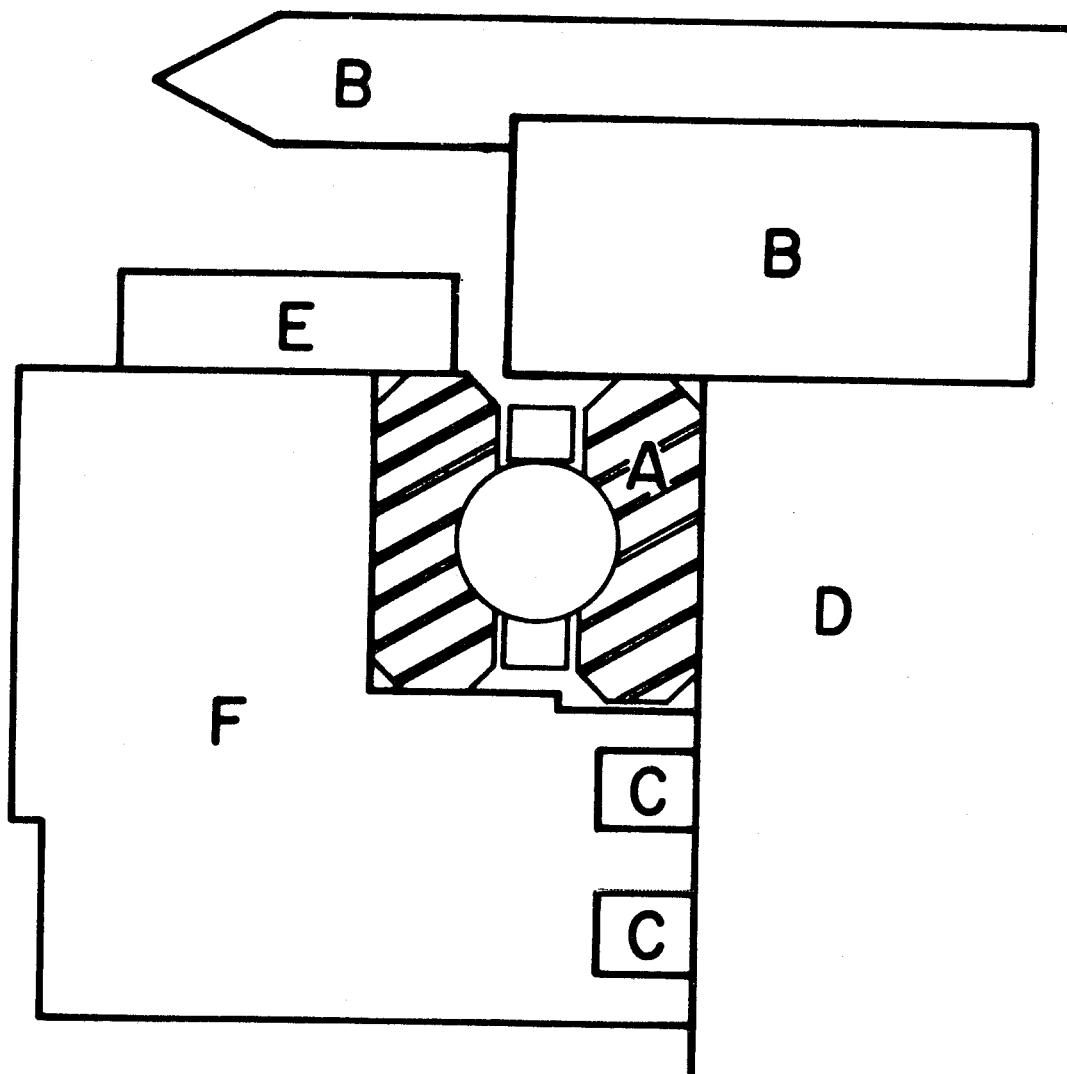
diffusion pump, backed by a Precision D-500 mechanical pump. The detector chamber was equipped with an NRC 204 Orb-Ion pump which was mounted away from the line of sight of the detector by use of an NRC Model 4EL water-cooled elbow. The NHS-2 diffusion pumps were baffled by Model 0325 NRC cryobaffles. The VHS-6 diffusion pump was baffled by an NRC Model 0326-6 cryobaffle.

Documented pumping speeds for the pumps employed are:

    (a)   NRC HS-2:   285 liters/sec

    (b)   NRC VHS-6:   2400 liters/sec

    (c)   NRC Orb-Ion 204:   400 liters/sec

The cryobaffles when empty of liquid nitrogen cut these speeds down by approximately one-half.

Cooling water to the diffusion pumps was provided by means of externally cooled recirculated distilled water flow metered by Brooks 18 and 30 gallon per hour meters.

IV. RESULTS AND DISCUSSION

The data presented in this chapter were obtained through essentially two separate experiments. The apparatus described in the previous chapter was modified to detect neutral particles by secondary emission. This technique discussed in Reference (3) does not yield the identity of the fragments resulting from dissociative recombination except for diatomic parent ions. It does offer, however, a means of observing baseline recombination signals which provide information for further work toward identifying product species.

The experimental configuration for the first segment of the work is illustrated in flow chart form by Figure 23. It is basically the same as for later investigation excluding the high efficiency ionizer, spherical deflector and quadrupole mass filter. High energy ions, 900 volts, were produced from the primary ion source. Neutrals resulting from recombination using such an energetic beam are considered "hot" or "fast neutrals". They were allowed to impinge on the cathode of the electron multiplier causing secondary emission. Pulses from the multiplier were amplified and counted by means of the circuitry previously described.

The systems studied using the fast neutral technique were

$$(a) \quad N_2^+ + e^- \rightarrow N_2^* \rightarrow N + N$$

$$(b) \quad N_2H^+ + e^- \rightarrow N_2H^* \rightarrow N_2 + H$$

$$(c) \quad CH_4^+ + e^- \rightarrow CH_4^* \rightarrow CH_3 + H$$

$$CH_4^+ + e^- \rightarrow CH_4^* \rightarrow CH_2 + 2H \text{ or } H_2$$

$$CH_4^+ + e^- \rightarrow CH_4^* \rightarrow CH + 3H$$

$$CH_4^+ + e^- \rightarrow CH_4^* \rightarrow C + 4H$$
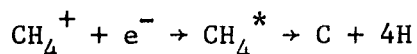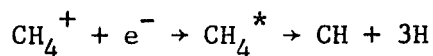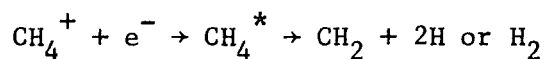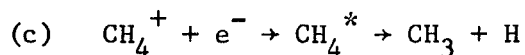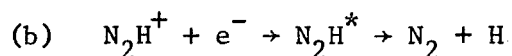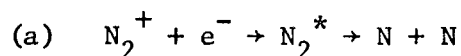
Figure 23

Flow Chart of Apparatus Configuration for the Fast Neutral Experiment

ION
SOURCE
(A)

BEAM PATH

EXTRACTION
LENSES
(B)

WIEN
FILTER
(C)

DECELERATION
LENSES
(D)

ELECTRON
GUN
(F)

BENDIX 306
ELECTRON
MULTIPLIER
DETECTOR
(G)

DETECTOR
ROTATION
PATH

(d) $NH_3^+ + e^- \rightarrow NH_3^* \rightarrow NH_2 + H$

$NH_3^+ + e^- \rightarrow NH_3^* \rightarrow NH + 2H \text{ or } H_2$

$NH_3^+ + e^- \rightarrow NH_3^* \rightarrow N + 3H$
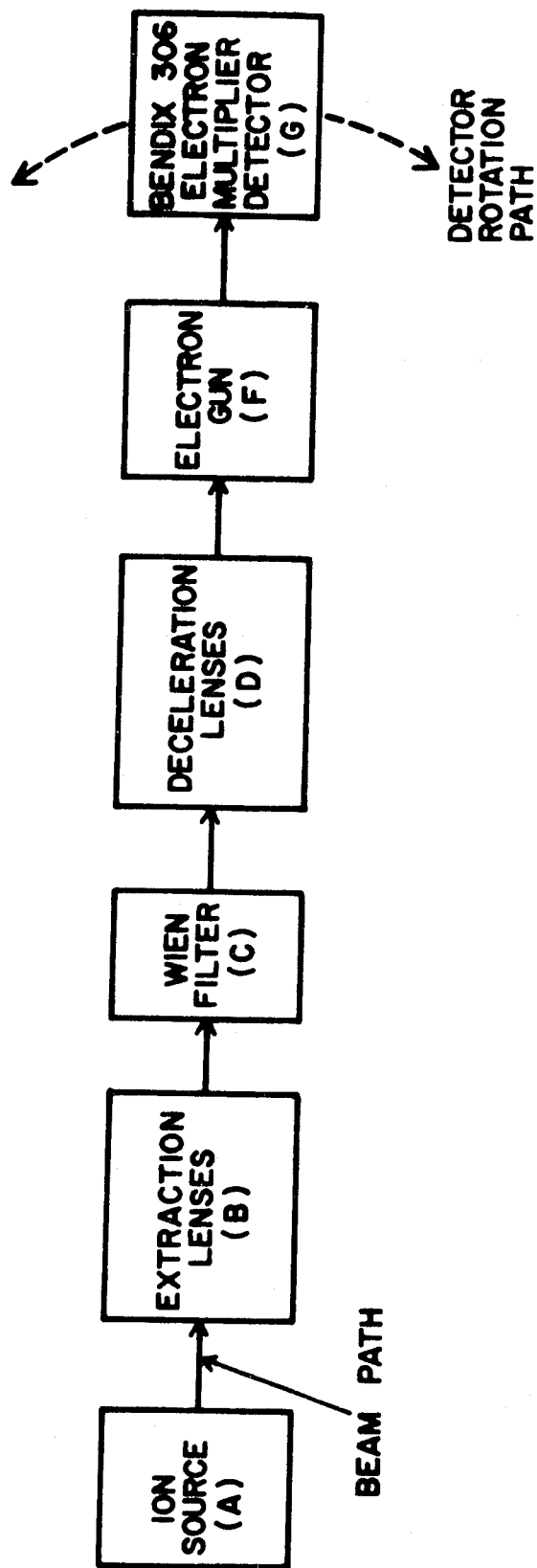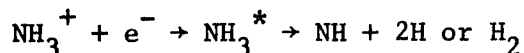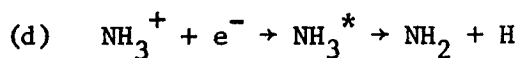
All possible reaction paths are shown for CH_4^+ and NH_3^+ since the products were not positively identified. The molecule N_2H does not exist as a stable entity, thus for N_2H^* the process indicated above should be the most probable path. The primary beam was mass selected with the Wien filter. Although the species were not passed through the quadrupole, the Wien filter was calibrated with nitrogen. The two characteristic peaks for nitrogen, N^+ and N_2^+, were noted as to the magnetic field strength necessary for maximum peak observation. The peak intensities composing the spectrum of each molecule investigated were observed on the Keithley electrometer and referenced to the two nitrogen peaks.

Signal intensities in terms of counts/sec were plotted against applied anode potential. These data are displayed in Appendix A. The cross sections for recombination can be calculated from experimental parameters as found in Chapter II. The equation employed is

$$\sigma(E) = \frac{I_n}{I_e} \frac{v_i v_e}{|\, (v_i)^2 + (v_e)^2 \,|^{\frac{1}{2}}} \frac{e}{L} \frac{A}{I_i} \quad cm^2 \qquad (27)$$

where I_n, I_e and I_i represent the neutral, electron and ion currents, respectively; v_i and v_e represent the ion and electron velocities; L the interaction path length; A the interaction area; and e is the electronic charge. For the fast neutral experiment v_i is 900 volts, v_e varies from 0 to approximately 7 volts, I_e is the effective interacting emission current in amperes, I_i is approximately 10^{-9} amperes and I_n varies with

the system being investigated. L is 4.18 cm and A is 0.080 cm^2.

The Weiss equation describing the potential minimum between the interaction region anode and grid was solved by graphical integration for a beam of 1/8 inch in diameter. The average interaction energy was found to be V/3.41 where V is the applied anode potential in volts. The V/4 relationship derived by Weiss is approached by a very "thin" beam centered exactly between the anode and grid region.

Tabulated cross sections for N_2^+, N_2H^+, CH_4^+ and NH_3^+ are to be found in Appendix A. It should be noted that the N_2H^+ primary ion currents were obtained with both C_2H_2 and NH_3 in the ionization chamber of the primary source. This does not mean that C_2H_2 and NH_3 give N_2H^+ directly but that conditions in the source contribute to its formation. The boron nitride housing of the source was observed to give both N^+ and N_2^+ currents when the filaments were brought to operating conditions. When molecules containing hydrogen such as the paraffins and NH_3 were subjected to ionization, strong currents of N_2H^+ resulted. It appears that conditions in this type of source are harsh enough to produce high concentrations of hydrogen as well as cause breakdown of the boron nitride insulating surface.

A composite plot of recombination cross sections against the calculated interaction energy is given in Figure 24 for all species investigated by the fast neutral technique. It can be seen that the cross sections approach zero above about 2 volts, interaction energy, and above approximately 7 volts applied anode potential. Table IV in Appendix A lists results from this work and from Hagen (3) for N_2^+ recombination cross sections. Hagen's values are seen to be somewhat higher for several reasons: (a) he collected total recombination signal whereas the detector

58

Figure 24

Recombination Cross Section versus Interaction

Energy for N_2^+, N_2H^+, CH_4^+ and NH_3^+
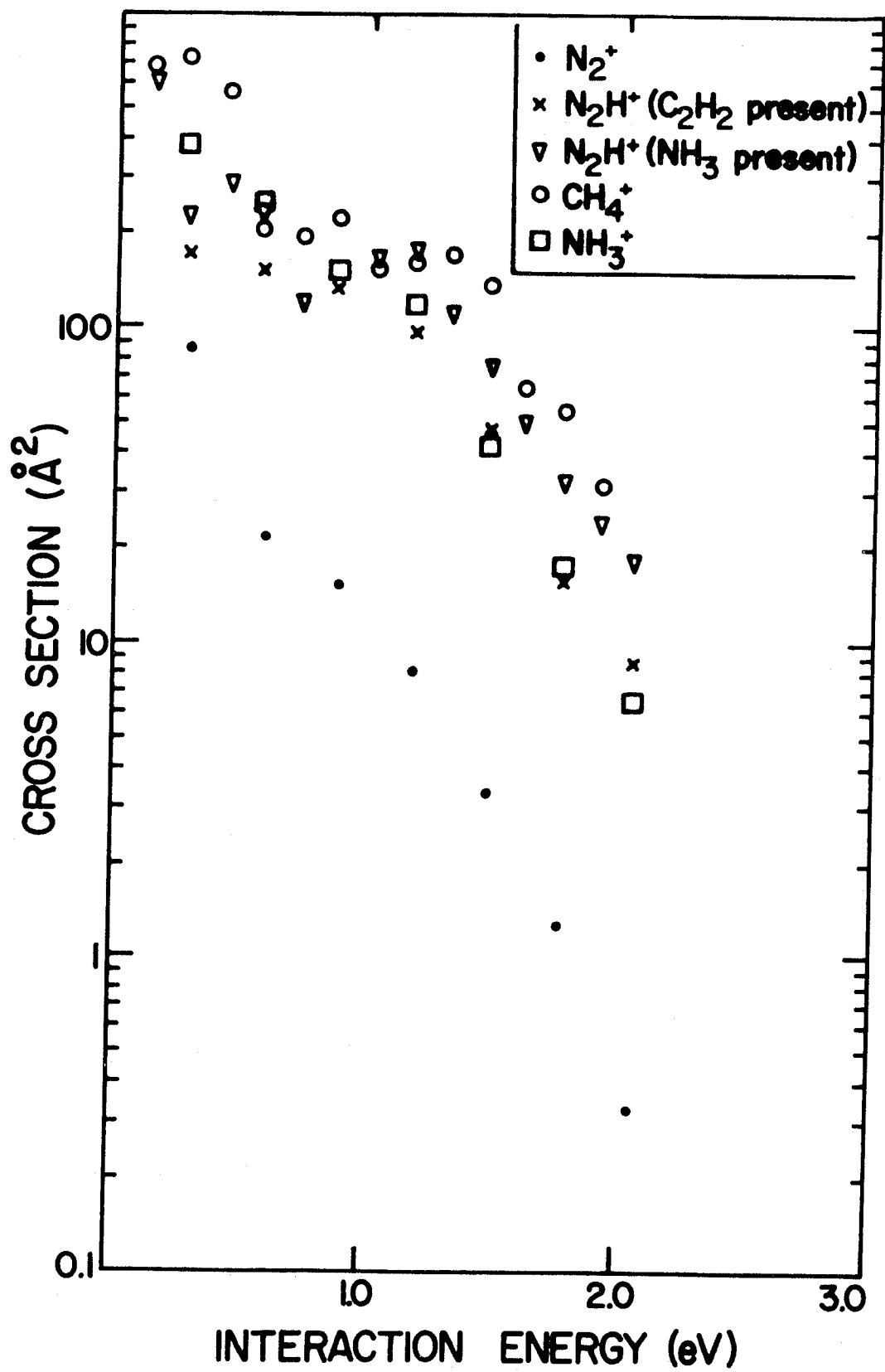
in this experiment was set at one angle only and the signal collected; (b) Hagen achieved lower operating pressures and thus better signal to noise ratios. The discriminator setting on the counting module had to be set at a relatively high value to achieve good signal to noise ratios. This higher setting relative to the value needed to simply buck out the normal electronic circuit noise can easily discriminate against a portion of the signal while discriminating against the background; (c) as seen in Equation (27), the cross section for beams intersecting at 90° is reciprocally related to the sum of the squares of ion beam velocity and electron beam velocity, taken to the one-half power whereas for colinear beams, intersecting at 0°, the cross section is reciprocally related to the difference of these two parameters. Thus with increasing electron velocity, a smaller cross section will be obtained for right angle interaction.

It can be seen, however, that the cross sections for N_2H^+, CH_4^+ and NH_3^+ are significantly larger than for N_2^+. This would seem logically related to the number of degrees of freedom possessed by a species. The more degrees of freedom, the more states available for accommodation of the colliding electron energetically in the AX^* transient complex. Also, Biondi (38) has indicated that dissociative recombination cross sections theoretically should vary from 10^{-16} cm^2 to 10^{-14} cm^2 with the larger value relating to polyatomic ions.

Large background signals were observed during initiation of the experiment and consequently the primary ion beam was deflected in the horizontal plane before entrance into the neutralizer. This deflection necessitated setting the detector "off angle" from the true zero angle by five degrees for maximum signal detection. The very large background counts observed at the original zero angle resulted from charge exchange

within the primary ion beam. Beam deflection in addition to higher relative discriminator settings gave reduced background noise and, thus, better signal to noise ratios. Angular distributions, however, were observed to be non-symmetric around the zero angle as a consequence of primary beam deflection. The distribution for N_2^+ is given in Figure 25. Distributions for species such as N_2H^+ and CH_4^+ are not given. Systems such as these which can give a light fragment, H, and a heavy one produced signals confined to a total angle of a few degrees. The light fragment carries away most of the energy of dissociation as kinetic energy leaving the heavier fragment confined to a relatively small angle. This point will be elaborated on later in this chapter.

The second experiment had the objective of both detection and identification of product species. The detector included those elements not present in the "fast neutral" configuration. Also, due to the very low signals under consideration, the Wien filter and deceleration lens system were removed. Figure 26 gives the apparatus assembly in flow chart form. The detector was moved forward, closer to the exit aperture of the primary ion source. The experiment had been previously attempted with all elements present and at the longer ion path distance but without success. Even in the modified configuration, N_2^+ did not yield a recombination signal. This again illustrates that the magnitude of the product angular dispersion can drop signal levels below the detection threshold.

If one considers the two systems

$$N_2^+ + e^- \rightarrow N_2^* \rightarrow N + N$$

and

$$CH_4^+ + e^- \rightarrow CH_4^* \rightarrow CH_3 + H$$
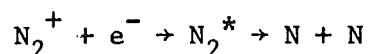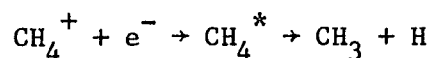
Figure 25

Angular Distribution for N_2 at 4.00 Volts Applied Anode Potential

(fast neutrals)
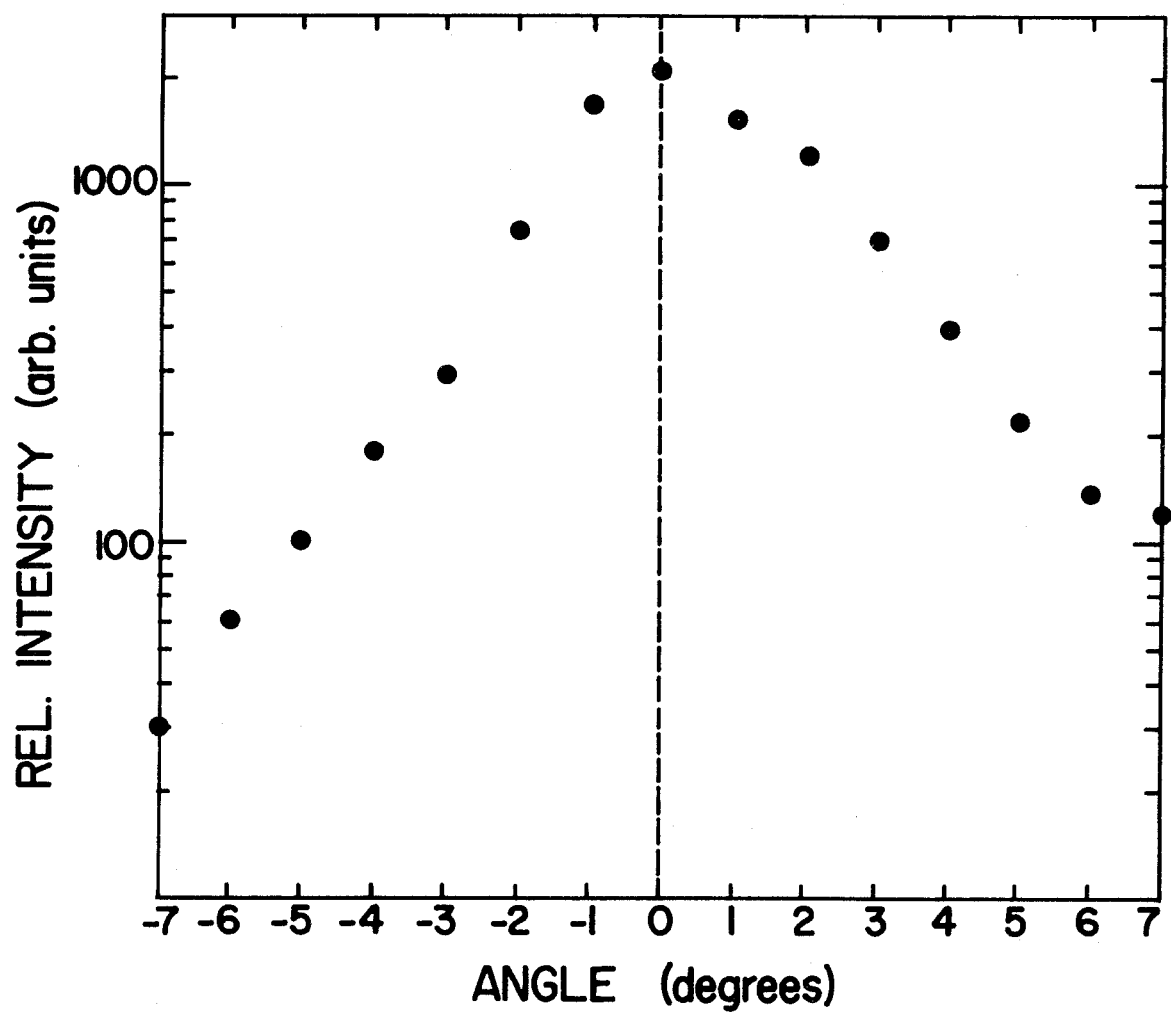
Figure 26

Flow Chart of Apparatus Configuration for

the Reionized Neutral Experiment

PRIMARY
ION
SOURCE

EXTRACTION
AND
FOCUSING
LENS

NEUTRALIZER

HIGH
EFFICIENCY
IONIZER

SPHERICAL
DEFLECTOR

90°

QUADRUPOLE
MASS
FILTER

BENDIX 306
MEM
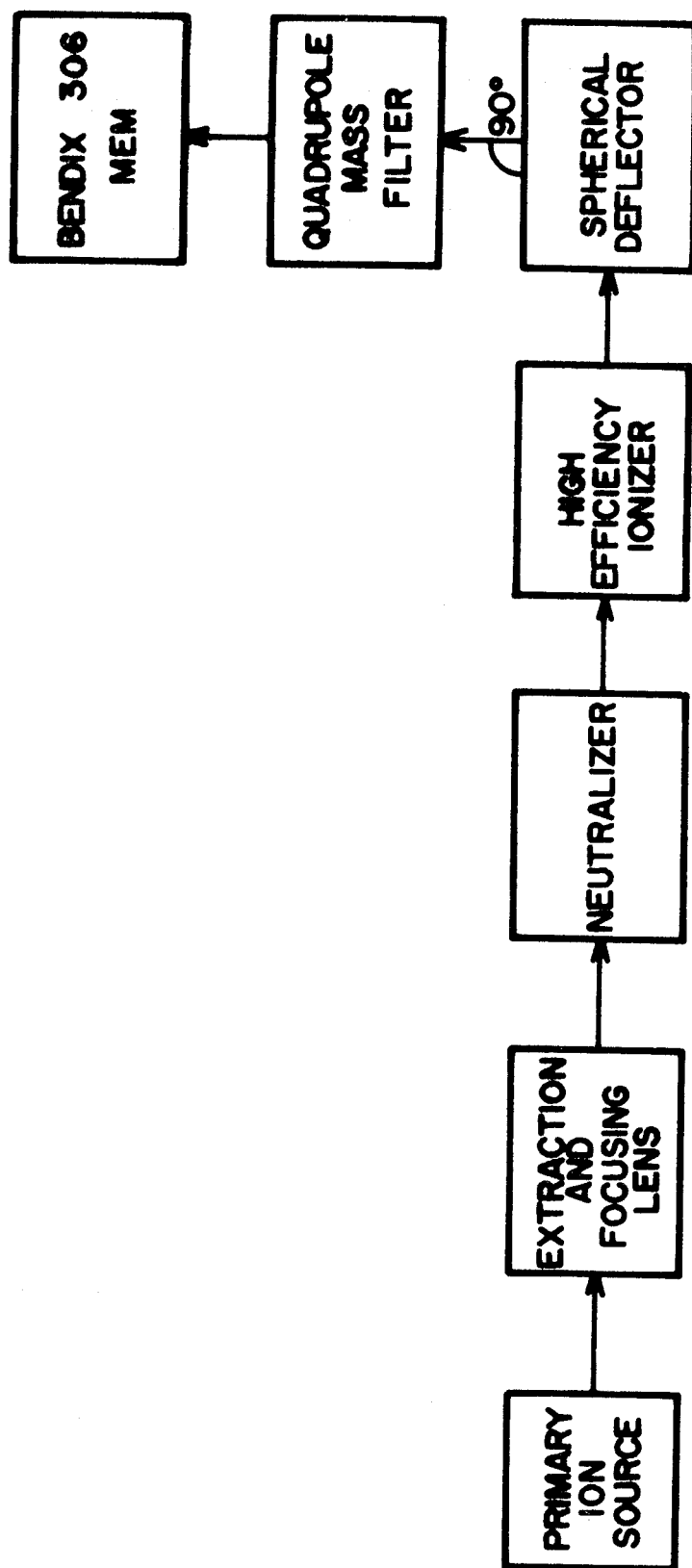
at 200 volts primary ion beam energy, the dispersion angle will be determined by the energy carried away by each fragment in the center of mass system. Appendix J gives the derivation of the equation which describes the collision of the ion and electron in the center of mass system. It can be seen from these equations that the angular dispersion for the N_2^+ system is given by the relation

$$\tan \Theta = \frac{V_N}{V_{C.M}} = \frac{\left[2 \frac{m_N}{m_N} \frac{e}{M}\right]^{\frac{1}{2}}}{\left[2 \frac{E_{C.M}}{M}\right]^{\frac{1}{2}}} = \left[\frac{e}{E_{C.M}}\right]^{\frac{1}{2}} \tag{28}$$

$$\tan \Theta \cong 0.191 \tag{29}$$

$$\Theta \cong 11° \tag{30}$$

$$2\Theta \cong 22° \tag{31}$$

where the reaction exothermicity, e, is calculated to be 7.3 volts.

For the $CH_4^+ + e^-$ system, the angular dispersion if in regard to the CH_3 fragment is given by

$$\tan \Theta = \frac{\left[2 \frac{m_H}{m_{CH_3}} \frac{e}{M}\right]^{\frac{1}{2}}}{\left[2 \frac{E_{C.M}}{M}\right]^{\frac{1}{2}}} \tag{32}$$

$$\tan \Theta = \left[\frac{m_H}{m_{CH_3}} \frac{e}{E_{C.M}}\right]^{\frac{1}{2}} \tag{33}$$

$$\Theta \cong 0.058 \tag{34}$$

$$\Theta \cong 3° \tag{35}$$

$$2\Theta \cong 6° \tag{36}$$

where the reaction exothermicity is calculated to be 10.1 volts. Similarly the spread for the H fragment is given by

$$\tan \Theta = \left[\frac{^m CH_3}{^m H} \frac{e}{E_{C.M}} \right]^{\frac{1}{2}} \tag{37}$$

$$\tan \Theta \cong 0.870 \tag{38}$$

$$\Theta \cong 41° \tag{39}$$

$$2\Theta \cong 82° \tag{40}$$

It should be noted that the previous equations cannot predict the direction of the product fragment relative velocity vector. This indicates the fragments can be scattered in any direction from the dissociation center. The product, also, would not be confined to the plane of intersection of the ion and electron beams but cover a complete 2π steradians of solid angle. Systems, therefore, such as N_2H^+, CH_4^+ and $C_2H_2^+$ were chosen since dissociation can result in a relatively light particle, namely, H. Thus, detection possibility is increased for the species ejecting the light fragment.

The ion beam obtained from the primary source was held at 200 volts for each molecule investigated. The primary beam was first analyzed at high resolution and the strongest peaks noted. The mass spectra for CH_4, N_2H and C_2H_2 are given in Figures 27, 28 and 29 as an example of the primary source output. Abundance ratios for this source are not exactly the same as those obtained for normal electron impact spectra. The nature of the source in regard to operation and temperature during ionization is not compatible with the electron impact source. The source can be operated in a quasi-electron impact mode, however, which minimizes the

Figure 27

Mass Spectrum of CH_4
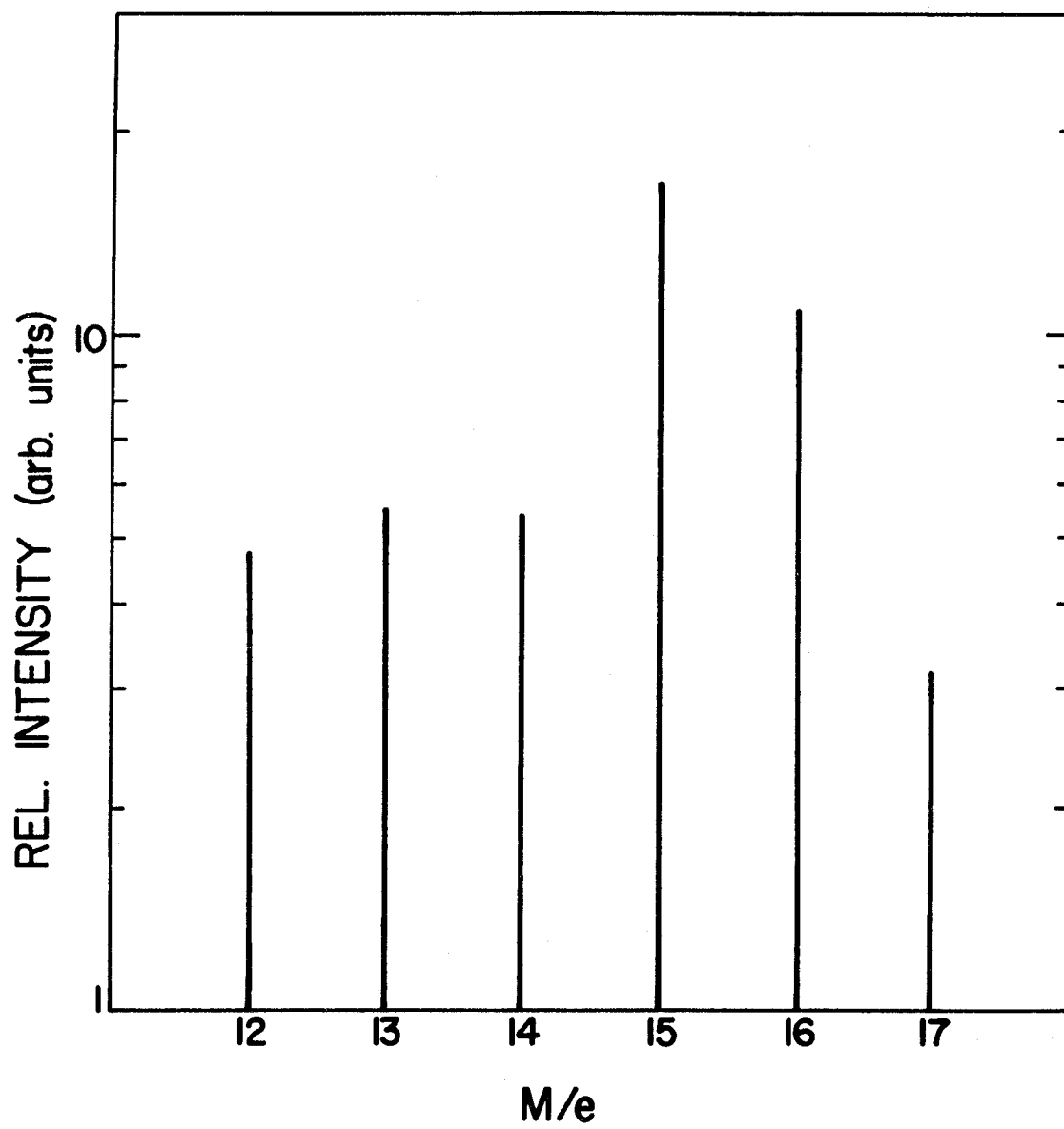
Figure 28

Mass Spectrum of N_2H
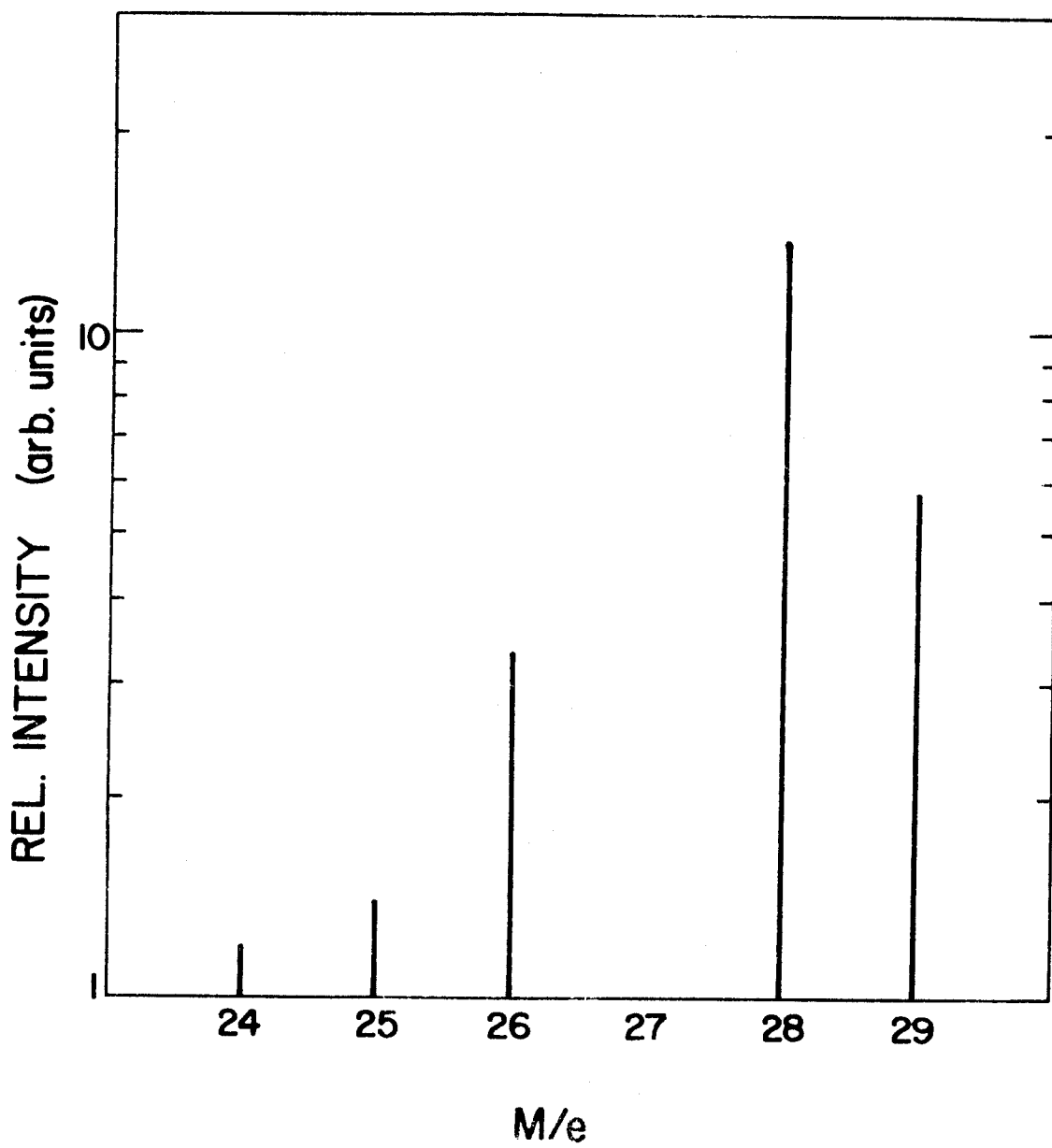
Figure 29

Mass Spectrum of C_2H_2
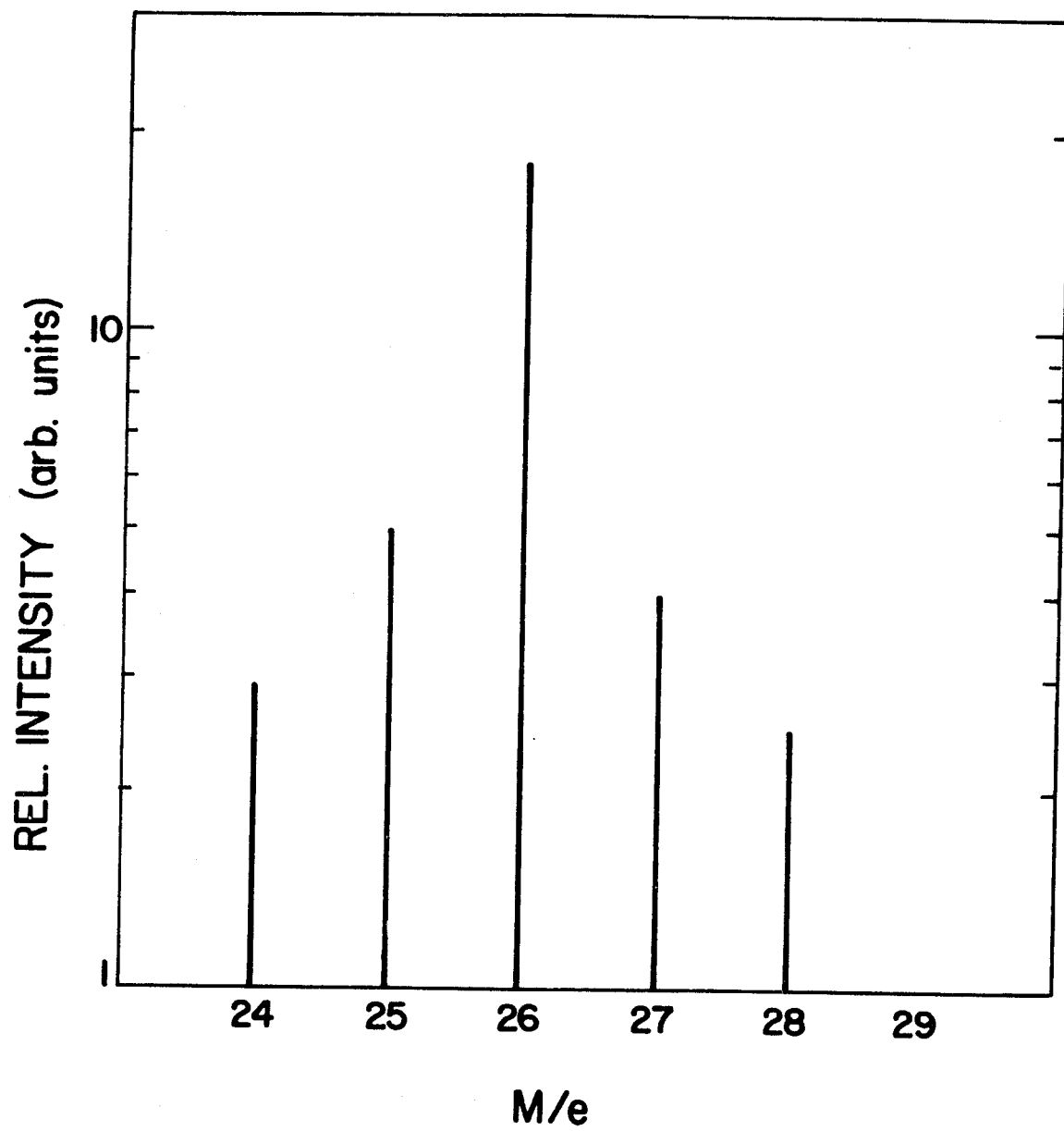
intensity of N_2H^+ but the beam energy spread is large, i.e., 60 volts

full width at half-height. In the discharge mode, the energy spread is

less than 2 volts but the intensities of N_2H^+ obtained with hydrogen-

bearing species were very strong. For this second experiment, the source

was operated in the impact mode but in the fast neutral experiment where

lower intensity primary ion beams were satisfactory, the discharge mode

was employed. It should be mentioned that the discharge mode produces

strongest N_2H^+ intensities when maximum beam intensity is sought. The

presence of N_2H^+ in the beam has the dual disadvantage of obscuring

signals in the m/e = 28 range and also contributes to the maximum space

charge limited current obtainable in the beam without enhancing wanted

signals.

After mass analysis of the primary beam, the filter was set to

detect species from ions occurring in the primary beam, having both high

intensity and capability of dissociation upon recombination, i.e., CH_4^+

and not C^+.

The following processes were investigated in this portion of the work:

(a) $N_2H^+ + e^- \rightarrow N_2H^* \rightarrow N_2 + H$

   $N_2 + e^- \rightarrow N_2^+ + 2e^-$ m/e = 28, species detected

(b) $CH_4^+ + e^- \rightarrow CH_4^* \rightarrow CH_3 + H$

   $CH_3 + e^- \rightarrow CH_3^+ + 2e^-$ m/e = 15, species detected

(c) $CH_4^+ + e^- \rightarrow CH_4^* \rightarrow CH_2 + 2H$ or H_2

   $CH_2 + e^- \rightarrow CH_2^+ + 2e^-$ m/e = 14, species detected

(d) $CH_3^+ + e^- \rightarrow CH_3^* \rightarrow CH_2 + H$

   $CH_2 + e^- \rightarrow CH_2^+ + 2e^-$ m/e = 14, species detected

(e) $C_2H_2^+ + e^- \rightarrow C_2H_2^* \rightarrow C_2H + H$

$C_2H + e^- \rightarrow C_2H^+ + 2e^-$ m/e = 25, species detected
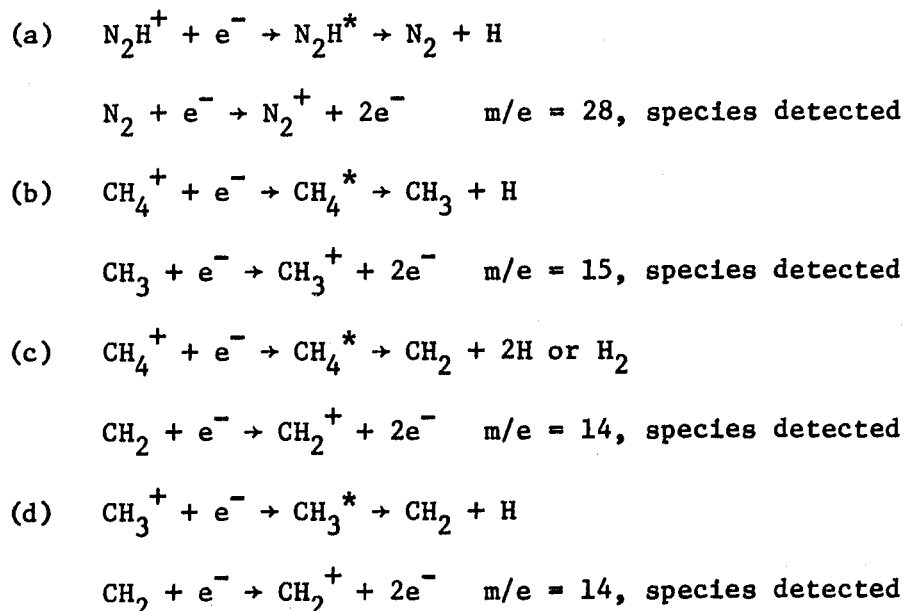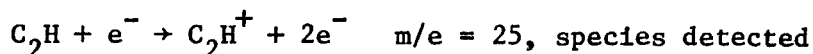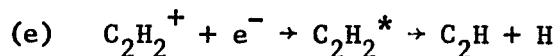
Plots of signal intensity versus applied anode potential are given in Appendix A. The cross section calculation for the reionized neutrals takes the ionization efficiency of the quadrupole ionizer into consideration. The equation used is

$$\sigma(E) = \frac{I_n}{I_e} \frac{v_i v_e}{|\,(v_i)^2 + (v_e)^2\,|^{\frac{1}{2}}} \frac{e}{L} \frac{A}{I_i} \frac{v_i}{v_t} \text{(I.E)} \tag{41}$$

where I.E. is the ionization efficiency of the ionizer for thermal ions, about 0.1%, and v_t is the thermal velocity of the species in question. The other parameters have been described previously. Cross sections from this part of the experiment are tabulated in Appendix A. Figure 30 gives a composite plot of the systems studied in terms of cross section versus interaction energy.

The cross sections obtained from the reionized neutral experiment are small for possibly two reasons; (a) the signal was not collected over the entire dispersion angle but at one fixed location. As mentioned earlier, the signal would be scattered over a complete 2π steradians of solid angle and not confined to only the plane of intersection of the ion and electron beam; (b) it had been determined earlier that the detector train transmission could be reduced by as much as a factor of 10. Ion beam intensity monitored on the spherical deflector surface differed by as much as 10 compared to that collected on the multiplier at the quadrupole exit (39).

70

Figure 30

Recombination Cross Section versus Interaction

Energy for CH_4^+, N_2H^+ and $C_2H_2^+$
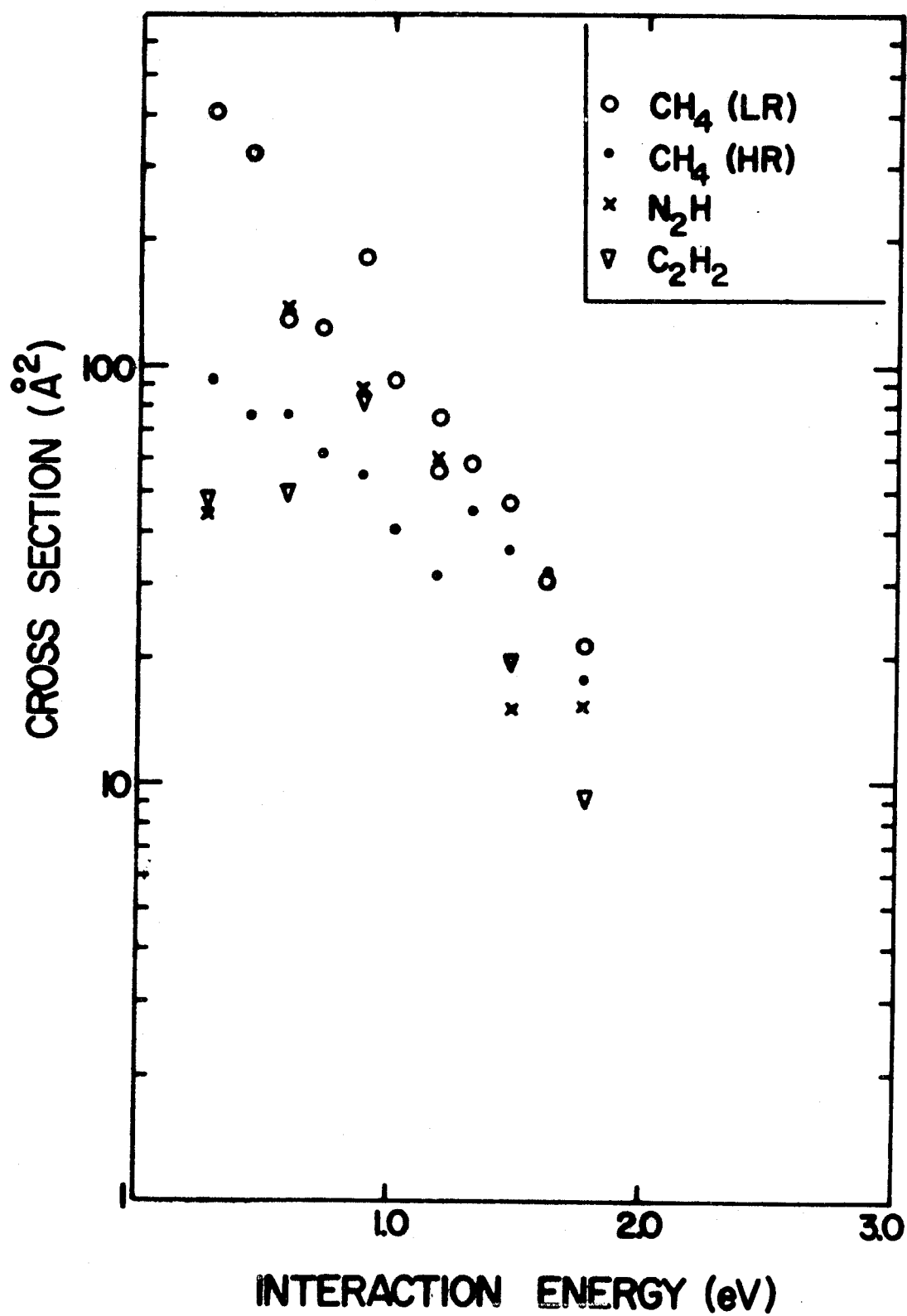
It can be seen that the cross sections from both experiments compare favorably in order of magnitude when a correction factor for transmission is taken into account. With the reionized signal, data is indicated at both high and low resolution for CH_4. High resolution indicates sufficient resolution to separate close peaks, i.e., $m/e = 15$ and 14. Some signal intensity, however, can be lost as resolution increases.

V. CONCLUSIONS

The apparatus as assembled and operated for this work must be termed a "first generation" machine. The data collected and presented in this thesis represents an effort to shed more light upon ion-electron recombination from the standpoint of mechanism. The crossed beam technique with product species identification is a complex subject experimentally due to the low signal intensities observed. The microwave experiments set the stage in a manner of speaking for these investigations by giving basic cross section data for diatomic species. Hagen performed the intermediate step required in regard to placing such studies on the beam level.

Work was completed employing the fast neutral technique for several molecules. The cross sections obtained agree in order of magnitude with predicted values and available experimental data. The recombination cross sections were found to increase with parent molecular ion complexity. Also, product species from recombination reactions were identified by reionization and subsequent mass analysis for three systems. It was observed that one decomposition path is the ejection of a light fragment. Other paths for decomposition may be followed, such as $C_2H_2 \rightarrow 2CH$, but the products can be dispersed over an angle too large for provision of threshold detection intensities. Cross sections calculated from the reionized neutral experiment agree favorably with those from the initial phase of this work.

The apparatus can be improved to give more refined data and allow for expansion of the number of systems possible for investigation. The feasibility of ion-electron recombination beam studies with product identification, however, has been demonstrated.

73

BIBLIOGRAPHY

1. E. Rutherford, Phil. Mag. 44, 422 (1897).

2. P. Visconti et al., Phys. Rev. 3, 1310 (1971).

3. G. Hagen, Ph.D. Thesis, Department of Physics, University of California, Los Angeles, California 90024, March 1968.

4. J. C. Tully, Z. Herman and R. Wolfgang, J. Chem. Phys. 54, 1730 (1971).

5. W. Aberth, J. Peterson, D. Lorentz and C. Cook, Phys. Rev. Letters 20, 979 (1968).

6. W. Miller, S. Safron and D. Herschbach, Disc. Faraday Soc. 44, 108 (1967).

7. D. R. Bates and A. Dalgarno, Atomic and Molecular Processes (Academic Press, New York, 1962), ed. by D. R. Bates, Chap. 7, pp. 245-279.

8. J. Sayers, Proc. Roy. Soc. (London) A169, 83 (1938).

9. M. A. Biondi and S. Brown, Phys. Rev. 75, 1700 (1949); M. A. Biondi and S. Brown, Phys. Rev. 76, 1697 (1949).

10. S. Nielson and J. Dahler, J. Chem. Phys. 45, 4060 (1966).

11. E. W. McDaniel, Collision Phenomena in Ionized Gases (John Wiley and Sons, Inc., New York, 1964), Chap. 12.

12. B. Davis and A. Barnes, Phys. Rev. 34, 1229 (1929).

13. J. Hammer and B. Aubrey, Phys. Rev. 141, 146 (1966).

14. M. F. A. Harrison, Methods of Experimental Physics, Vol. 7, Part A, (Academic Press, New York, 1968), ed. by B. Bederson and W. L. Fite, Chap. 1.4, pp. 95-100.

15. The ion source, acceleration optics, Wien Filter and deceleration lens system were purchased from the Colutron Corporation, P. O. Box 1288, Boulder, Colorado.

16. M. Menzinger and L. Wahlin, Rev. Sci. Instr. 40, 102-105 (1969).

17. Circuit diagram for the deceleration lens system is given in Appendix G.

18. L. Wahlin, Nuc. Instr. and Meth. 38, 133 (1965).

19. A. Henglein and G. Muccini, Zeits Naturforsch. 17a, 452 (1962).

20. R. Weiss, Rev. Sci. Instr. _32_, 397 (1961).

21. K. R. Spangenberg, _Vacuum Tubes_ (McGraw-Hill Book Co. Inc., New York, 1948).

22. J. W. Gervantowski and H. A. Watson, _Principles of Electron Tubes_ (D. Van Nostrand Co. Inc., Princeton, New Jersey, 1965), p. 119.

23. F. W. Lampe, J. L. Franklin and F. H. Field in _Progress in Reaction Kinetics_ (Pergamon Press, London, 1961), ed. by G. Porter, Vol. 1, p. 69.

24. F. Rosebury, _Handbook of Electron Tube and Vacuum Techniques_ (Addison-Wesley Publishing Co. Inc., Reading, Massachusetts, 1965), pp. 103-104.

25. H. F. Krause, Ph.D. Thesis, Department of Physics, University of Pittsburgh, Pittsburgh, Pennsylvania, 1970; J. Geddes, H. F. Krause and W. L. Fite, J. Chem. Phys. _52_, 3296 (1970).

26. Extranuclear Laboratories, Pittsburgh, Pennsylvania. Private communication with R. T. Brackmann, Technical Director.

27. H. Wollnik in _Focusing of Charged Particles_ (Academic Press, New York and London, 1967), ed. by A. Septier, Vol. 2, pp. 163-202.

28. H. E. Duckworth and S. N. Ghoshal in _Mass Spectrometry_ (McGraw-Hill, New York, 1963), ed. by C. A. McDowell, pp. 210-216.

29. W. Paul and H. Steinwedil, Z. Naturforsch. _82_, 448 (1953).

30. P. H. Dawson and N. R. Whetten, General Physics Laboratory, General Electric Corporation, Schenectady, New York, Report 68-c-418, December, 1968.

31. G. W. Goodrich and W. C. Wiley, Rev. Sci. Instr. _32_, 846 (1961).

32. C. A. Spindt and K. R. Shoulders, Rev. Sci. Instr. _36_, 775 (1965).

33. C. F. Barnett and J. A. Ray, ORNL-3760, p. 63, Oak Ridge National Laboratory, Oak Ridge, Tennessee, 1964.

34. The voltage divider circuit diagram for the Bendix 306 multiplier is to be found in Appendix G.

35. The digital counting equipment was purchased from Ortec, Oak Ridge, Tennessee.

36. The thrust bearing for the rotating lid was purchased from Kaydon Engineering Corporation.

37. P. C. McLeod, Research/Development _13_, 45 (1968); The Tech Seal Corporation, 22624 Avalon Boulevard, Wilmington, California 90745.

38. M. Biondi, Eighth Int. Symposium on Combustion, The Williamson and Wilkins Co., Baltimore, Maryland, pp. 21-30, 1926; M. Biondi, Endeavour, Vol. XXIV, 40 (1965).

39. When using the quadrupole as a drift space.

40. M. F. A. Harrison, Brit. J. Appl. Phys. 17, 371 (1966).

41. K. T. Dolder, M. F. A. Harrison and P. C. Thonemann, Proc. Roy. Soc. A, 264, 367-78 (1961); K. T. Dolder, M. F. A. Harrison and P. C. Thonemann, Proc. Roy. Soc. A, 274, 546-51 (1963).

42. H. Goldstein, Classical Mechanics (Addison-Wesley, 1950); E. W. McDaniel, Collision Phenomena in Ionized Gases (John Wiley and Sons, Inc., New York, 1964); R. D. Present, Kinetic Theory of Gases (McGraw-Hill Book Co., Inc., New York, 1958).

APPENDIX A

Intensity and Cross Section Data

I. Sample Data

The following data are representative of that collected for each species in the fast neutral experiment and used to calculate recombination cross sections. I_e refers to the usable or interacting electron current; I_{et} refers to the total electron current monitored.

(a) N_2^+ ($\sigma = 15.2$ $\overset{\circ}{A}{}^2$)

$$v_i = 900 \text{ V} = 7.87 \times 10^6 \text{ cm/sec}$$

$$v_e = 0.880 \text{ V} = 5.56 \times 10^7 \text{ cm/sec}$$

$$e = 1.6 \times 10^{-19} \text{ coulombs}$$

$$I_n = 161 \text{ sec}^{-1}$$

$$I_i = 1.2 \times 10^{-9} \text{ amps}$$

$$I_{et} = 3.8 \times 10^{-6} \text{ amps}$$

$$I_e = 3.4 \times 10^{-7} \text{ amps}$$

$$L = 4.18 \text{ cm}$$

$$A = 0.080 \text{ cm}^2$$

(b) N_2H^+ (NH_3 present)

$$(\sigma = 166 \text{ } \overset{\circ}{A}{}^2)$$

$$v_i = 900 \text{ V} = 7.73 \times 10^6 \text{ cm/sec}$$

$$v_e = 0.880 \text{ V} = 5.56 \times 10^7 \text{ cm/sec}$$

$$e = 1.6 \times 10^{-19} \text{ coulombs}$$

$$I_n = 128 \text{ sec}^{-1}$$

$$I_i = 1.4 \times 10^{-10} \text{ amps}$$

$$I_{et} = 2.3 \times 10^{-6} \text{ amps}$$

$$I_e = 2.04 \times 10^{-7} \text{ amps}$$

$$L = 4.18 \text{ cm}$$

$$A = 0.080 \text{ cm}^2$$

(c) N_2H^+ (C_2H_2 present)

$(\sigma = 135 \text{ Å}^2)$

$$v_i = 900 \text{ V} = 7.73 \times 10^6 \text{ cm/sec}$$

$$v_e = 0.880 \text{ V} = 5.56 \times 10^7 \text{ cm/sec}$$

$$e = 1.6 \times 10^{-19} \text{ coulombs}$$

$$I_n = 6970 \text{ sec}^{-1}$$

$$I_i = 1.0 \times 10^{-9} \text{ amps}$$

$$I_{et} = 2.18 \times 10^{-5} \text{ amps}$$

$$I_e = 1.93 \times 10^{-6} \text{ amps}$$

$$L = 4.18 \text{ cm}$$

$$A = 0.080 \text{ cm}^2$$

(d) CH_4^+ ($\sigma = 222 \text{ Å}^2$)

$$v_i = 900 \text{ V} = 1.04 \times 10^7 \text{ cm/sec}$$

$$v_e = 0.880 \text{ V} = 5.56 \times 10^7 \text{ cm/sec}$$

$$e = 1.6 \times 10^{-19} \text{ coulombs}$$

$$I_n = 194 \text{ sec}^{-1}$$

$$I_i = 1.3 \times 10^{-10} \text{ amps}$$

$$I_{et} = 3.78 \times 10^{-6} \text{ amps}$$

$$I_e = 3.35 \times 10^{-7} \text{ amps}$$

$$L = 4.18 \text{ cm}$$

$$A = 0.080 \text{ cm}^2$$

(e) NH_3^+ (157 $\overset{\circ}{A}$)

$$v_i = 900 \text{ V} = 1.01 \times 10^7 \text{ cm/sec}$$

$$v_e = 0.880 \text{ V} = 5.56 \times 10^7 \text{ cm/sec}$$

$$e = 1.6 \times 10^{-19} \text{ coulombs}$$

$$I_n = 108 \text{ sec}^{-1}$$

$$I_i = 5.0 \times 10^{-10} \text{ amps}$$

$$I_{et} = 7.61 \times 10^{-7} \text{ amps}$$

$$I_e = 6.73 \times 10^{-8} \text{ amps}$$

$$L = 4.18 \text{ cm}$$

$$A = 0.080 \text{ cm}^2$$

The following data are representative of that collected for each species in the reionized neutral experiment and used to calculate recombination cross sections.

(a) $C_2H_2^+$ ($\sigma = 87.5 \ \overset{\circ}{A}^2$)

$$v_i = 200 \text{ V} = 3.86 \times 10^6 \text{ cm/sec}$$

$$v_e = 0.880 \text{ V} = 5.56 \times 10^7 \text{ cm/sec}$$

$$v_t = 0.03 \text{ V} = 4.70 \times 10^4 \text{ cm/sec}$$

$$e = 1.6 \times 10^{-19} \text{ coulombs}$$

$$I_n = 6.85 \text{ sec}^{-1}$$

$$I_i = 1.2 \times 10^{-8} \text{ amps}$$

$$I_{et} = 1.14 \times 10^{-4} \text{ amps}$$

$$I_e = 1.01 \times 10^{-5} \text{ amps}$$

$$L = 4.18 \text{ cm}$$

$$A = 0.080 \text{ cm}^2$$

$$I.E \cong 10^{-3}$$

(b) N_2H^+ (σ = 88.5 $\overset{\circ}{A}^2$)

v_i = 200 V = 3.64 x 10^6 cm/sec

v_e = 0.880 V = 5.56 x 10^7 cm/sec

v_t = 0.03 V = 4.45 x 10^4 cm/sec

e = 1.6 x 10^{-19} coulombs

I_n = 4.06 sec^{-1}

I_i = 1.2 x 10^{-8} amps

I_{et} = 6.25 x 10^{-5} amps

I_e = 5.53 x 10^{-6} amps

L = 4.18 cm

A = 0.080 cm^2

$I.E \cong 10^{-3}$

(c) CH_4^+ (LR)

(σ = 181 $\overset{\circ}{A}^2$)

v_i = 200 V = 4.92 x 10^6 cm/sec

v_e = 0.880 V = 5.56 x 10^7 cm/sec

v_t = 0.03 V = 6.01 x 10^4 cm/sec

e = 1.6 x 10^{-19} coulombs

I_n = 4.98 sec^{-1}

I_i = 1.0 x 10^{-8} amps

I_{et} = 6.12 x 10^{-5} amps

I_e = 5.42 x 10^{-6} amps

L = 4.18 cm

A = 0.080 cm^2

$I.E \cong 10^{-3}$

(d) CH_4^+ (HR)

$$(\sigma = 54.3 \text{ Å}^2)$$

$$v_i = 200 \text{ V} = 4.92 \times 10^6 \text{ cm/sec}$$

$$v_e = 0.880 \text{ V} = 5.56 \times 10^7 \text{ cm/sec}$$

$$v_t = 0.03 \text{ V} = 6.01 \times 10^4 \text{ cm/sec}$$

$$e = 1.6 \times 10^{-19} \text{ coulombs}$$

$$I_n = 1.49 \text{ sec}^{-1}$$

$$I_i = 1.0 \times 10^{-8} \text{ amps}$$

$$I_{et} = 6.12 \times 10^{-5} \text{ amps}$$

$$I_e = 5.42 \times 10^{-6} \text{ amps}$$

$$L = 4.18 \text{ cm}$$

$$A = 0.080 \text{ cm}^2$$

$$I.E \cong 10^{-3}$$

It should be noted that the above neutral currents are given in particles or counts per second. The equations illustrated in the previous chapter regarding results and discussion are modified slightly to account for this as follows:

$$\text{(fast neutral)} \quad \sigma(E) = \frac{I_n}{I_e} \frac{v_i v_e}{|(v_i)^2 + (v_e)^2|^{\frac{1}{2}}} \frac{e^2}{L} \frac{A}{I_i} \text{ cm}^2 \tag{1}$$

and

$$\text{(reionized neutral)} \quad \sigma(E) = \frac{I_n}{I_e} \frac{v_i v_e}{|(v_i)^2 + (v_e)^2|^{\frac{1}{2}}} \frac{e^2}{L} \frac{A}{I_i} \frac{v_i}{(I.E) v_t} \tag{2}$$

II. Solid Angle Subtended by the Detector

In the fast neutral experiment, the distance from the center of the neutralizer to the detector aperture was 4". The diameter of the detector aperture was 1/16". The angle subtended by the detector was:

$$\tan \theta = \frac{1/32}{4} = 0.0078 \tag{3}$$

$$\theta = 28' \tag{4}$$

$$2\theta = 56' = 0.932° \tag{5}$$

In the reionized neutral experiment, the distance from the center of the neutralizer to the detector aperture was 4". The diameter of the detector aperture was 1/8". The solid angle subtended by the detector was:

$$\tan \theta = \frac{1/16}{4} = 1/64 = 0.0156 \tag{6}$$

$$2\theta = 1° \ 48' = 1.80° \tag{7}$$

TABLE IV

Recombination Cross Sections for N_2^+

(fast neutral)

Cross Section ($\overset{\circ}{A}{}^2$)		Int. E (volts)	Appl. Pot. (volts)
This Work	Hagen		
89.5	90.5	0.293	1.00
21.8	52.6	0.587	2.00
15.2	32.8	0.880	3.00
8.02	22.9	1.17	4.00
3.33	15.4	1.47	5.00
1.27	11.3	1.76	6.00
0.332	8.63	2.05	7.00

TABLE V

Recombination Cross Sections for N_2H^+ (C_2H_2 present)

Cross Section ($\overset{\circ}{A}^2$)	Int. E (volts)	Appl. Pot. (volts)
174	0.293	1
152	0.587	2
135	0.880	3
99.1	1.17	4
47.9	1.47	5
15.7	1.76	6
8.83	2.05	7

TABLE VI

Recombination Cross Sections for N_2H^+ (NH_3 present)

Cross Section $(\overset{\circ}{A}{}^2)$	Int. E (volts)	Appl. Pot. (volts)
604	0.147	0.50
224	0.293	1.00
292	0.440	1.50
229	0.587	2.00
124	0.733	2.50
166	0.880	3.00
169	1.03	3.50
176	1.17	4.00
111	1.32	4.50
75.8	1.47	5.00
51.6	1.61	5.50
32.3	1.76	6.00
24.1	1.91	6.50
18.3	2.05	7.00

TABLE VII

Recombination Cross Sections for CH_4^+

(fast neutral)

Cross Section ($\overset{\circ}{A}^2$)	Int. E (volts)	Appl. Pot. (volts)
695	0.147	0.50
730	0.293	1.00
576	0.440	1.50
203	0.587	2.00
198	0.733	2.50
222	0.880	3.00
159	1.03	3.50
165	1.17	4.00
170	1.32	4.50
139	1.47	5.00
65.3	1.61	5.50
55.2	1.76	6.00
31.7	1.91	6.50

TABLE VIII

Recombination Cross Sections for NH_3^+

Cross Section $(\overset{\circ}{A}{}^2)$	Int. E (volts)	Appl. Pot. (volts)
383	0.293	1.00
245	0.587	2.00
157	0.880	3.00
120	1.17	4.00
43.9	1.47	5.00
17.9	1.76	6.00
6.75	2.05	7.00

TABLE IX

Recombination Cross Sections for CH_4^+

(reionized neutral)

Cross Section ($\overset{\circ}{A}^2$)		Int. E (volts)	Appl. Pot. (volts)
LR	HR		
405	94.1	0.293	1.00
326	76.1	0.440	1.50
136	76.5	0.587	2.00
124	61.8	0.733	2.50
181	54.3	0.880	3.00
93.6	40.3	1.03	3.50
58.6	31.3	1.17	4.00
59.3	45.2	1.32	4.50
56.6	36.7	1.47	5.00
30.5	30.8	1.61	5.50
21.2	17.9	1.76	6.00

TABLE X

Recombination Cross Sections for N_2H^+

(reionized neutral)

Cross Section ($\overset{\circ}{A}{}^2$)	Int. E (volts)	Appl. Pot. (volts)
44.3	0.293	1.00
137	0.587	2.00
88.5	0.880	3.00
59.7	1.17	4.00
15.3	1.47	5.00
15.0	1.76	6.00

TABLE XI

Recombination Cross Sections for $C_2H_2^+$

(reionized neutral)

Cross Section $(\mathring{A}^2)$	Int. E (volts)	Appl. Pot. (volts)
46.7	0.293	1
48.2	0.587	2
87.5	0.880	3
74.6	1.17	4
19.1	1.47	5
9.05	1.76	6

Figure 31

Signal Intensity versus Applied Anode Potential for N_2^+

(fast neutral)
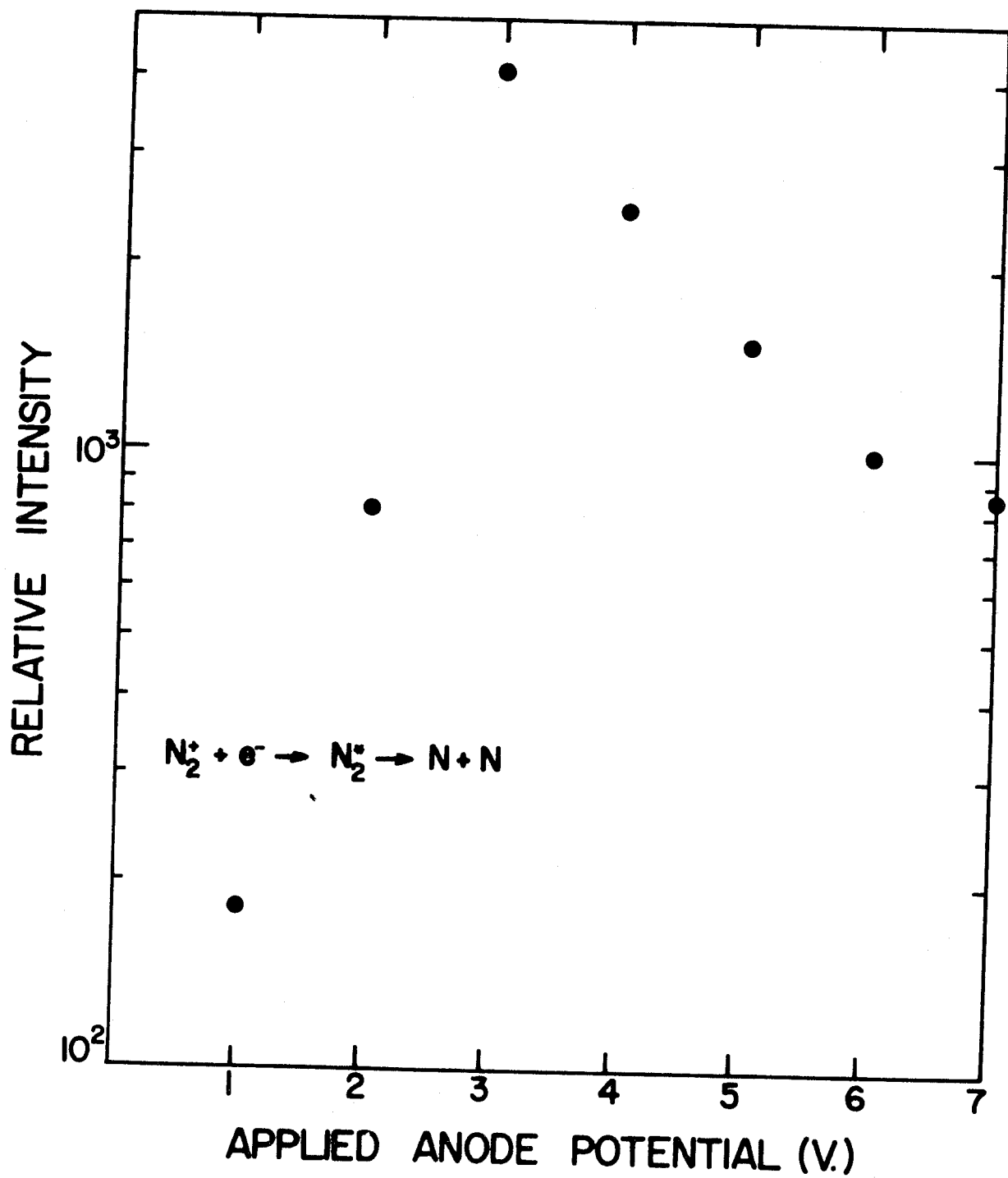
Figure 32

Signal Intensity versus Applied Anode Potential for N_2H^+

(C_2H_2 Present in Ionization Chamber)

(fast neutral)

$N_2H^+ + e^- \longrightarrow N_2H^* \longrightarrow N_2 + H$
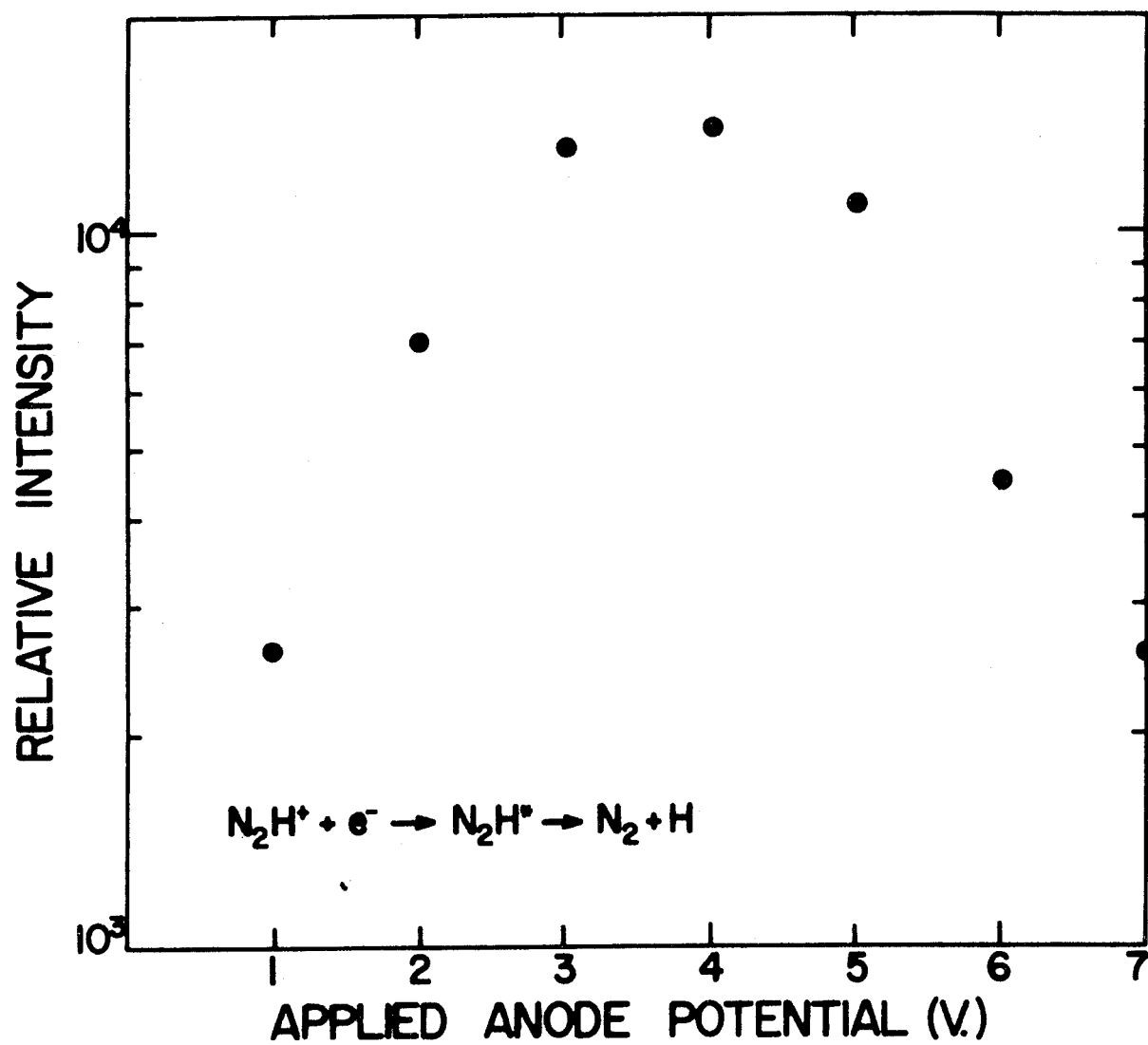
Figure 33

Signal Intensity versus Applied Anode Potential for N_2H^+

(NH_3 Present in Ionization Chamber)
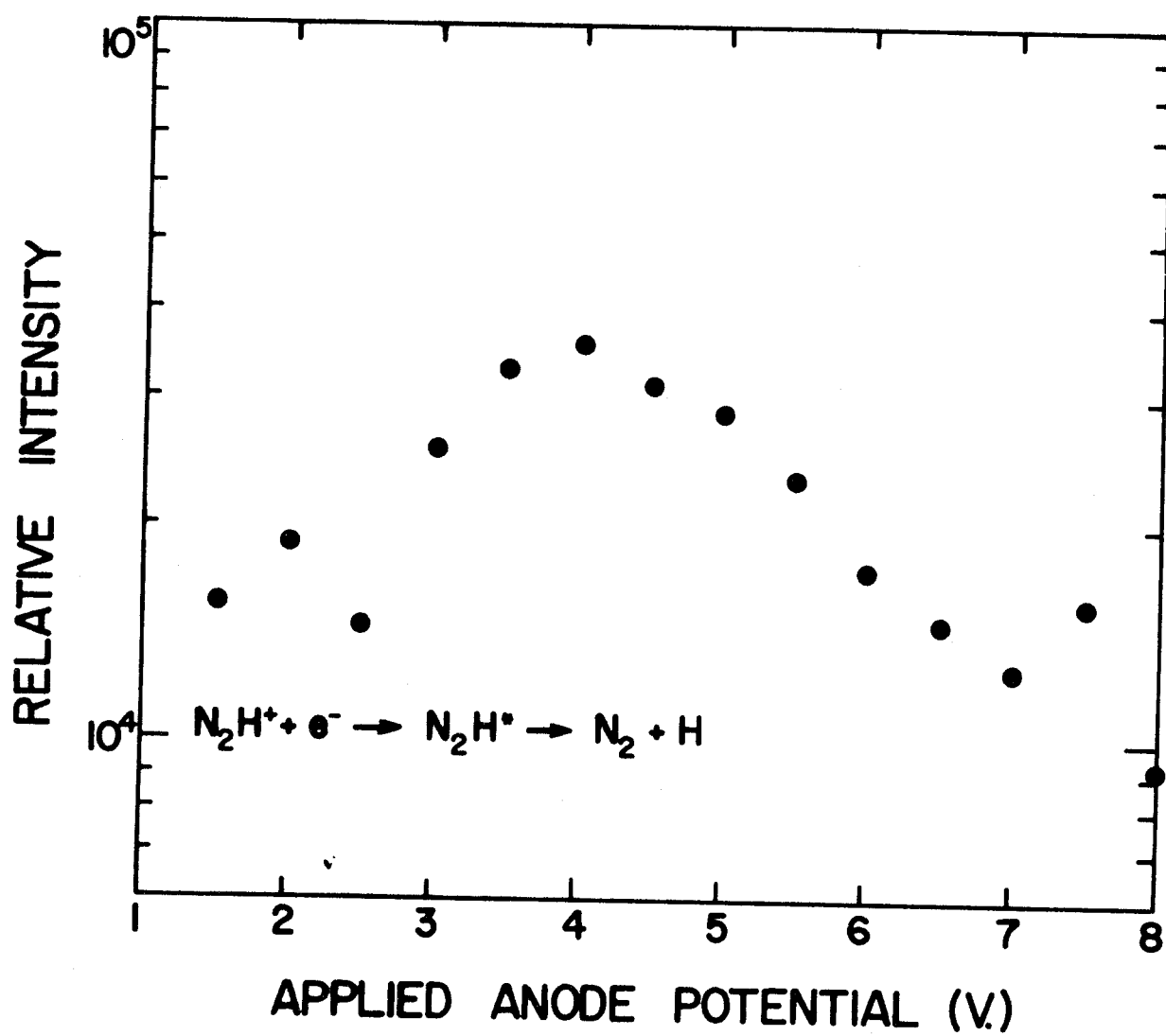
(fast neutral)

Figure 34

Signal Intensity versus Applied Anode Potential for CH_4^+

(fast neutral)
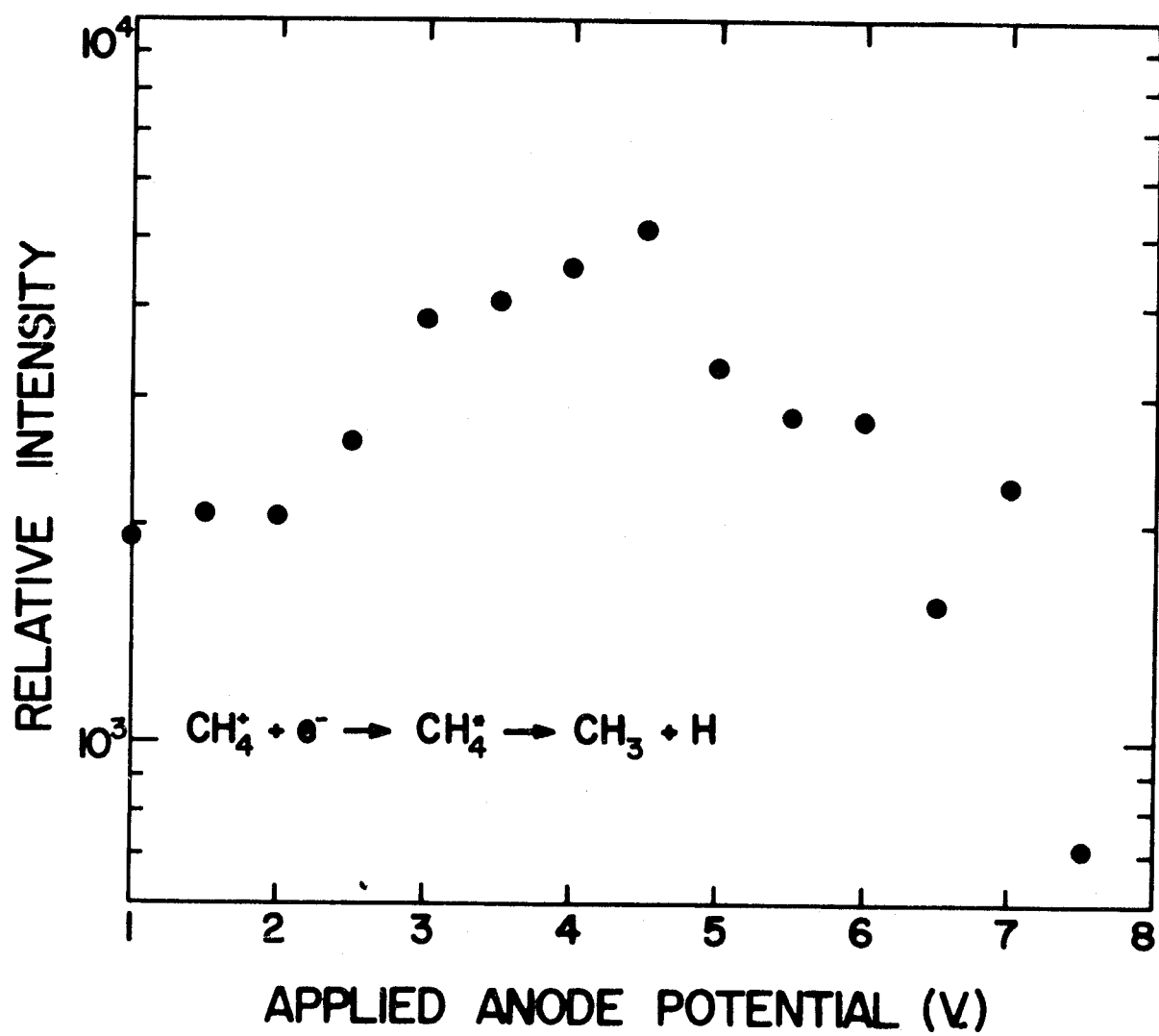
Figure 35

Signal Intensity versus Applied Anode Potential for NH_3^+

(fast neutral)

$NH_3^+ + e^- \rightarrow NH_3^* \rightarrow NH_2 + H$
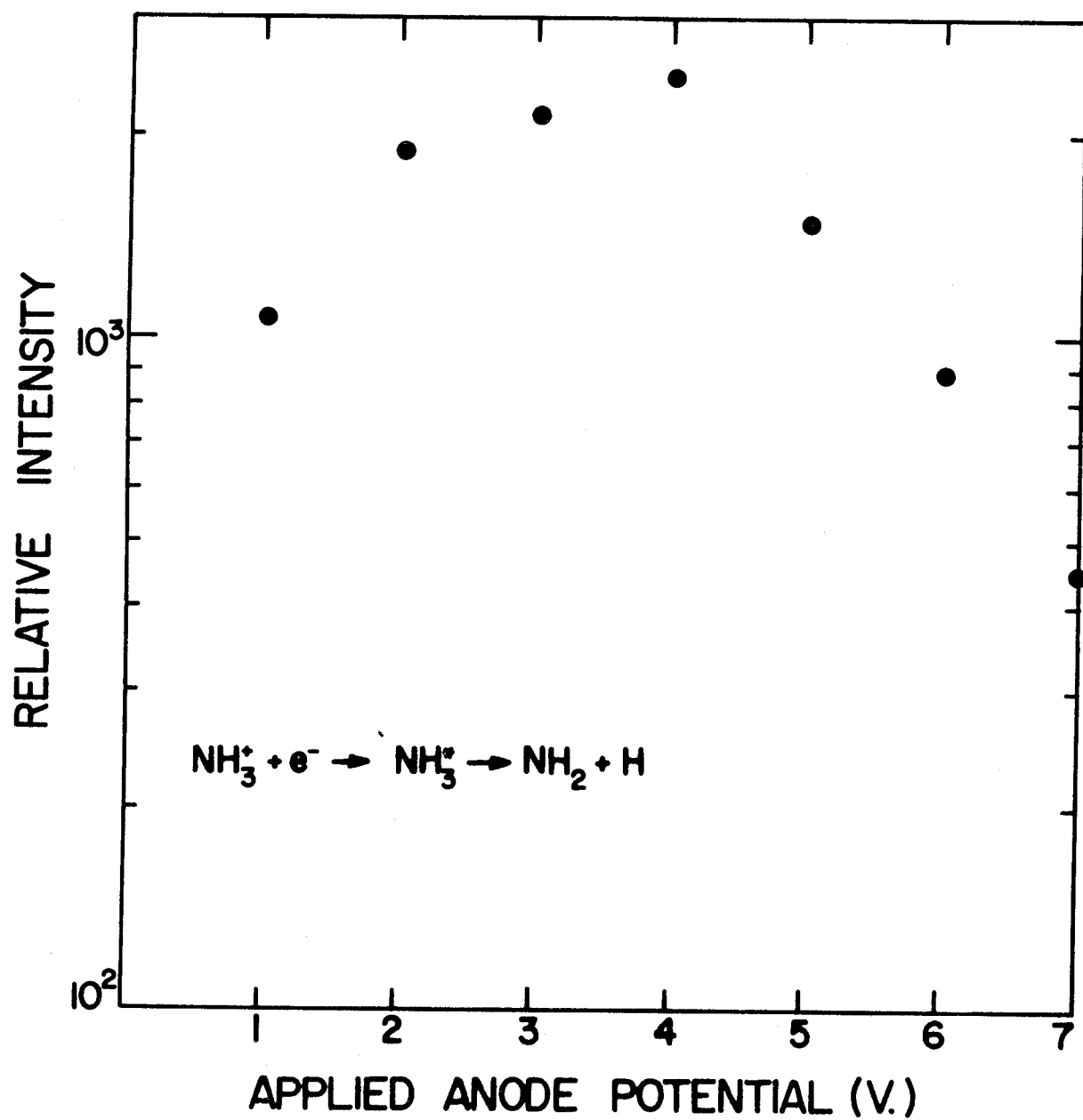
Figure 36

Signal Intensity versus Applied Anode Potential for CH_4^+

(reionizied neutral)

RELATIVE INTENSITY vs APPLIED ANODE POTENTIAL (V.)

$CH_4^+ + e^- \rightarrow CH_4^{**} \rightarrow CH_3 + H$

Figure 37

Signal Intensity versus Applied Anode Potential for $C_2H_2^+$

(reionized neutral)

$C_2H_2^+ + e^- \rightarrow C_2H_2^* \rightarrow C_2H + H$
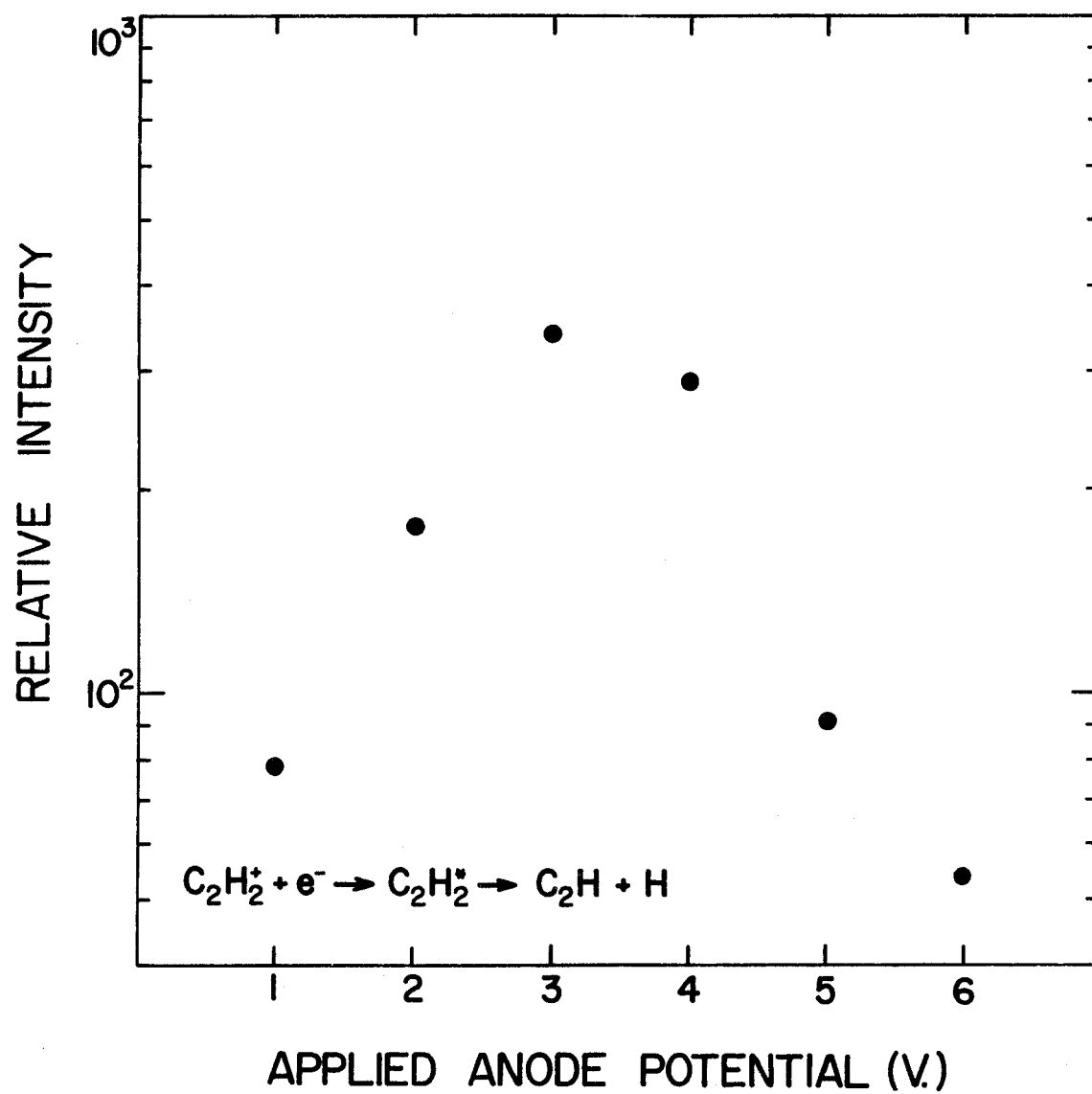
Figure 38

Signal Intensity versus Applied Anode Potential for N_2H^+

(reionized neutral)

$N_2H^+ + e^- \rightarrow N_2H^* \rightarrow N_2 + H$
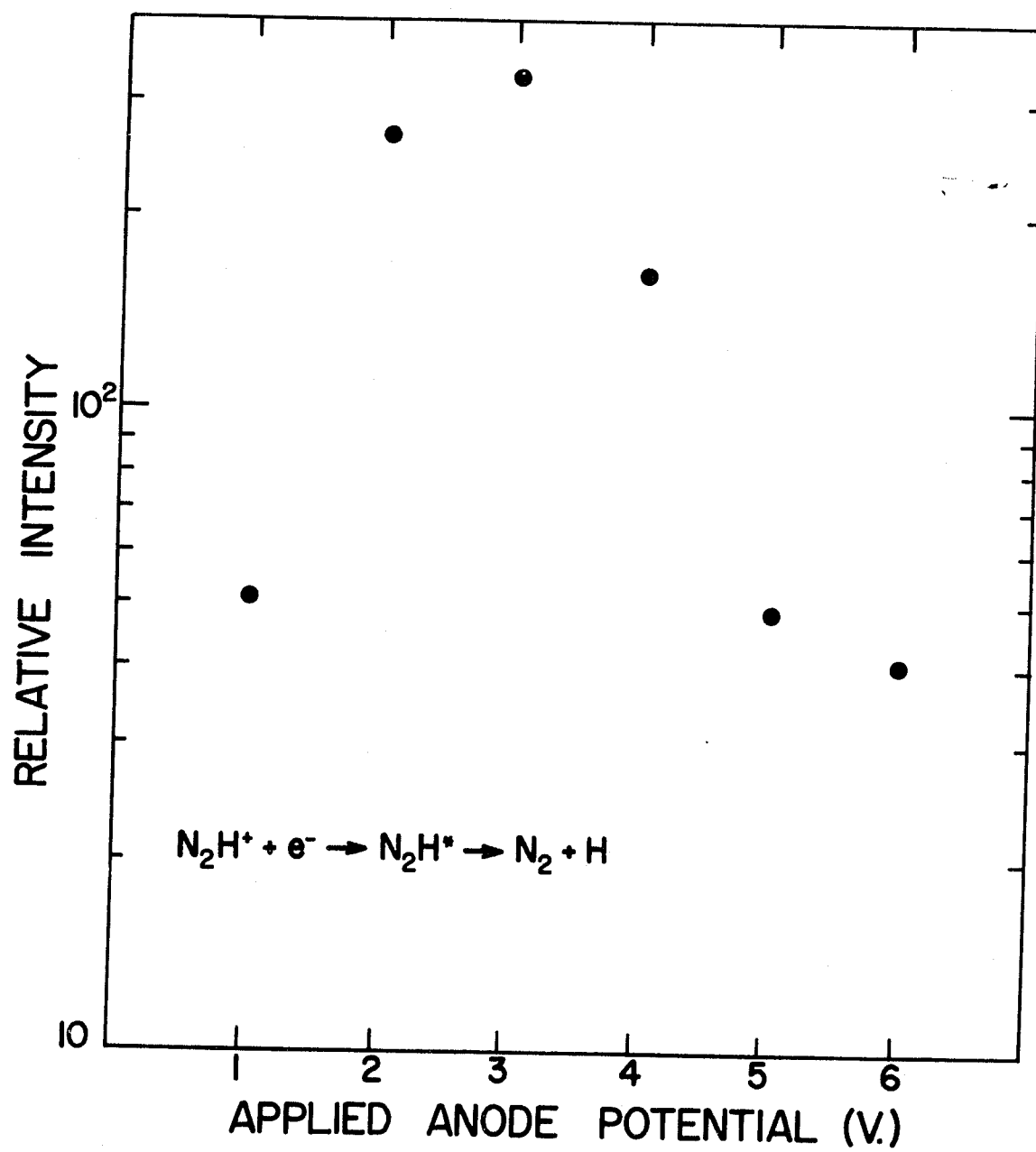
APPENDIX B

The Primary Ion Source

Power requirements for the source filament and anode were mentioned in Chapter II. Figure 39 illustrates the electrical circuitry for the source. The filaments are normally outgassed over a period of several hours. After the primary beam chamber has been pumped down and trapped with LN_2 (to a pressure of 2-5 x 10^{-7} torr), the filament current is slowly increased to half power for about 30 minutes to an hour. The current is then raised to the operation level slowly, not allowing the source pressure to rise over about 100 microns as indicated on the NRC 531 thermocouple controller. The anode supply can be turned up to 150 volts, after outgassing, and gas can be leaked into the source. The anode current, if an arc is struck, should not exceed 1 ampere. A current limiting resistor (100 ohm) is placed in series with the anode to protect the power supply. The gas flow can be decreased somewhat after an arc is struck.

This source can also be operated in the emission current mode as well as the discharge mode. For anode currents of less than 0.10 amp, optimumly 10-30 µamps, a discharge will not occur but strong beams are obtainable. The energy spread, however, for emission beams is larger than for the arc discharge beam.

Cleaning the boron nitride barrel and anode cap can be accomplished in two ways: (1) for lightly contaminated surfaces, the ultrasonic cleaner works quite well, or (2) for heavily coated surfaces, commercially available bleach solution will dissolve tungsten oxide and loosen other contaminants. After cleaning and thorough rinsing with distilled water,

Figure 39

Electrical Schematic of Primary Ion Source

A. Anode power supply

B. Filament power supply

C. Anode

D. Protection resistor

F. Filament

- A +

D

B

C

F

BEAM PATH
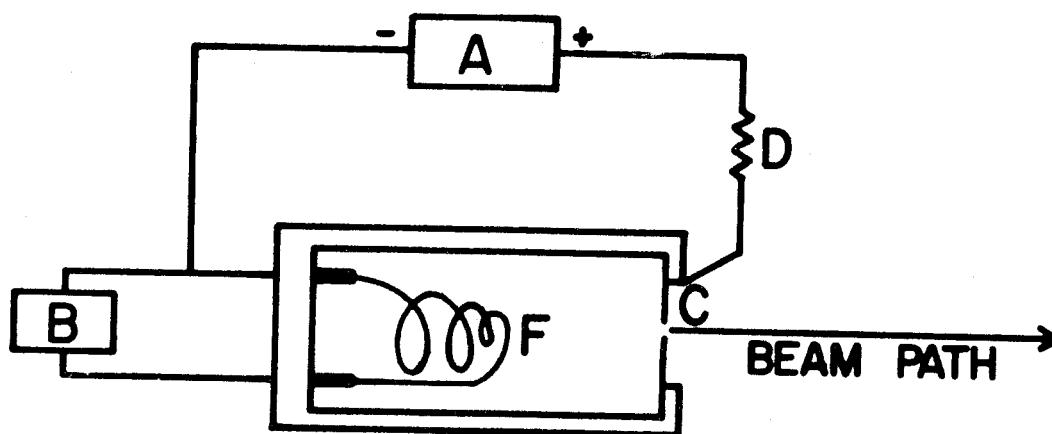
the parts are placed in an oven at 200°C for a period of 24 hours before assembly and installation.

Filament life varies with type of gas used, its elemental composition and ionization potential. Gases such as N_2 and Ar give longest lifetimes, the paraffins give moderate lifetimes and oxygen-containing species such as CO_2 or H_2O result in very short operating periods.

APPENDIX C

The Wien Filter

The power supply for the filter magnet is a Lambda Model LH122.
The magnet is designed to operate at 15 watts or 750 gauss uncooled.
The coils can be connected in series or parallel and each has a resis-
tance of 1.17 ohms. Cooling would be required for higher magnetic fields.
Electrically biased guard rings are part of the filter construction as
illustrated in Figure 40. These guard rings modify the electric field
in such a manner as to eliminate the focusing effect of the filter.
The circuit diagram for the guard ring control box is given in Figure 41.
A Kepco, Model HB2AM, power supply is used to operate this control.

For normal mass filter operation, the plate voltage is turned on
and the guard ring controls are set to a linear voltage across the plates,
then balanced. Plate voltage can be tuned to zero after balancing. The
ion beam is passed through the filter. A slight deflection may be
observed due to the residual magnetic field. The plate supply is used
to deflect the beam back. A small aperture, 1/16" in diameter, is used
in front of the target to observe beam intensity and deflection. The
beam is then adjusted with the magnet supply. This procedure should be
repeated in small increments while observing the intensity at the target.
As the filter is being powered, the beam may become distorted. The guard
ring potentials can be readjusted to eliminate any distortion. The
magnetic field is now varied for maximum intensity.

Figure 40

Schematic of Wien Filter Guard Ring Control Circuit Diagram
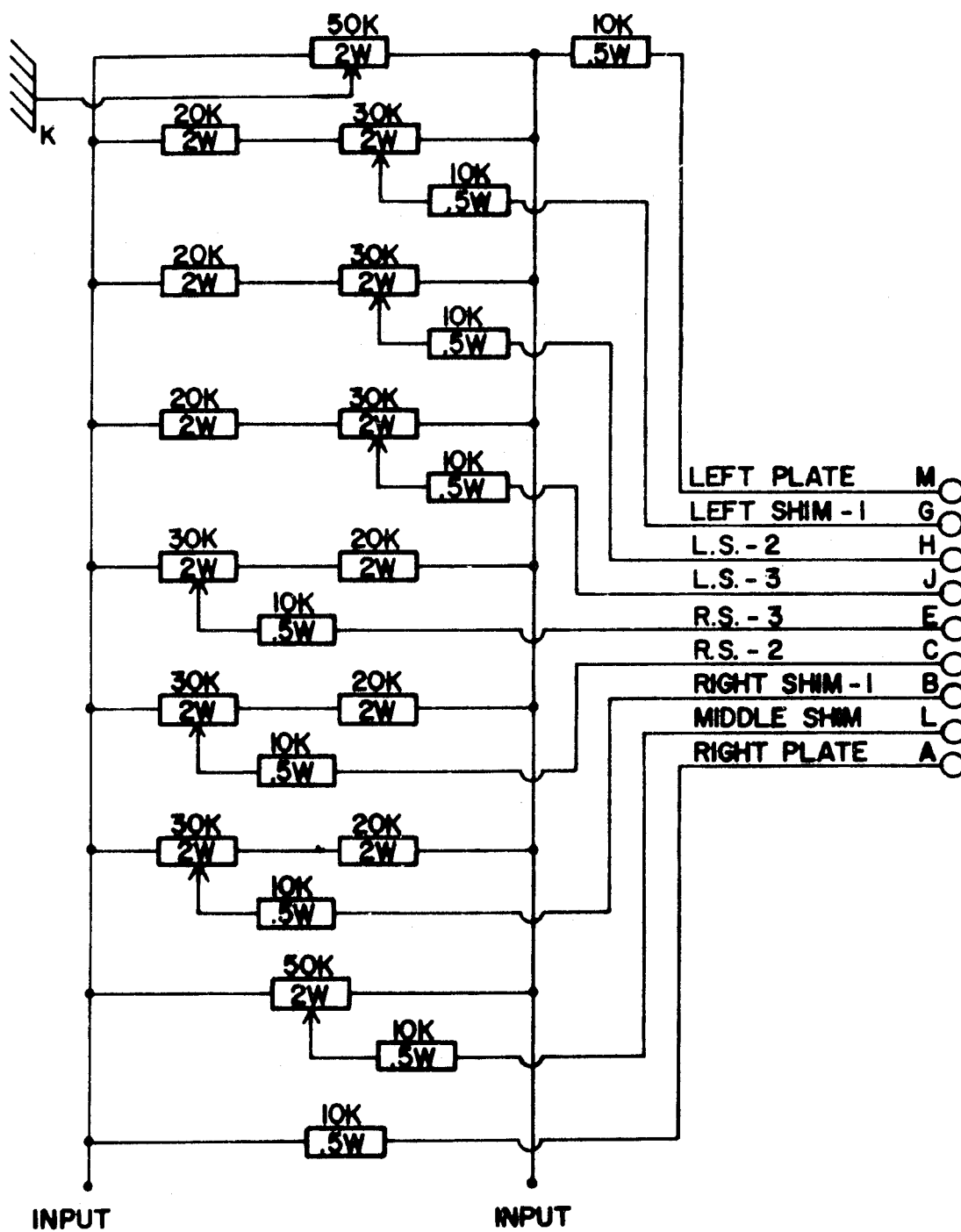
Figure 41

Schematic of the Wien Filter Indicating Guard Ring, Plate and Magnet Leads

PLATE
SHIM 3
SHIM 2
SHIM 1

4 3 2 1

N

S

+ ⊗ −
BEAM
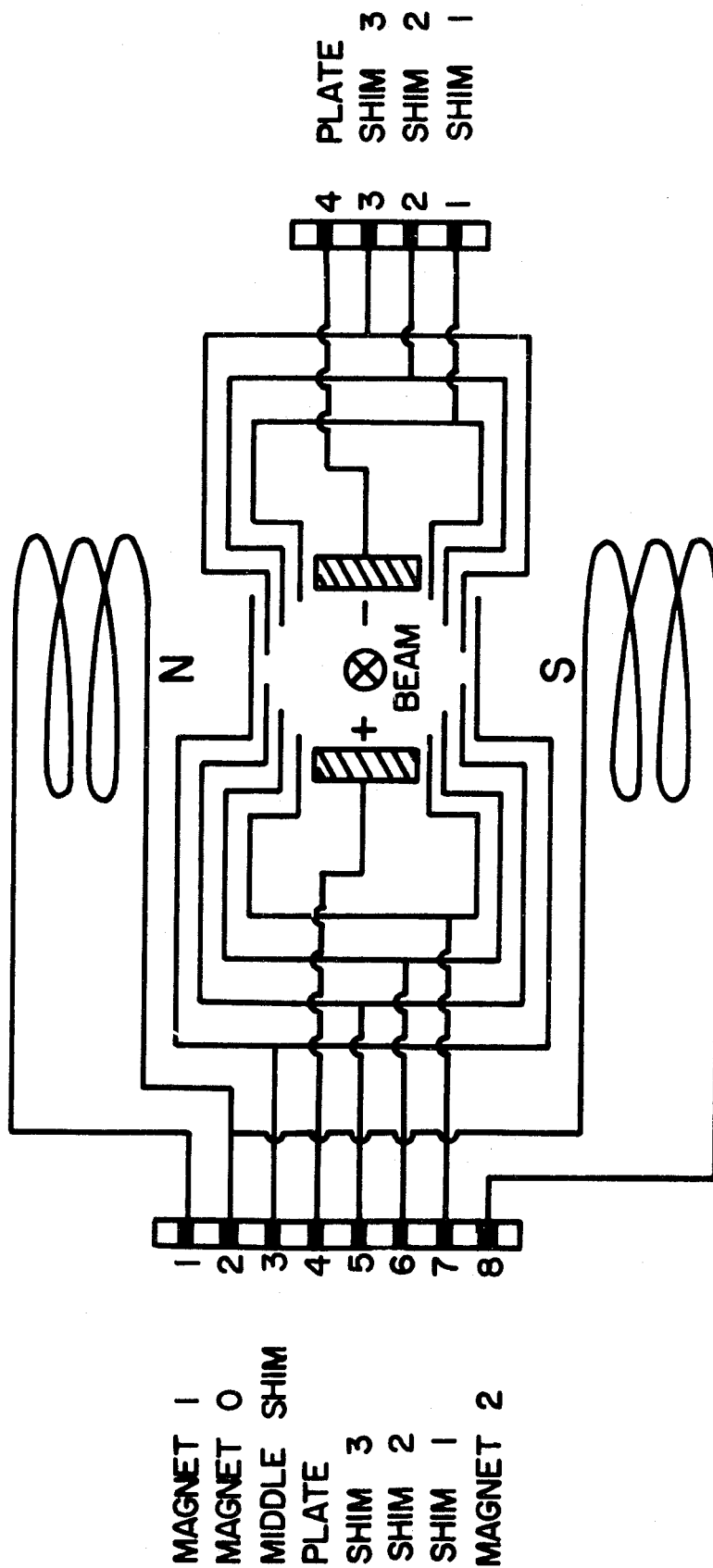
MAGNET 1
MAGNET 0
MIDDLE SHIM
PLATE
SHIM 3
SHIM 2
SHIM 1
MAGNET 2

1 2 3 4 5 6 7 8

APPENDIX D

The Electron Gun (Neutralizer)

The electron gun is readily disassembled for modification or cleaning. Cleaning procedures for molybdenum and stainless steel are given in Rosebury (24). A set of filaments should last several months. When they are replaced, however, it should be noted that outgassing is accomplished slowly since the interior of the cathode support is a relatively enclosed volume. Rapid outgassing will set up a discharge between the filaments and ground which can damage them. The cathode is very resistant to poisoning by simple exposure to atmosphere but care should be taken so chemical cleaning agents and/or fingerprints do not contact its surface.

Table XII gives typical emission currents obtained from the cathode as a function of applied anode potential. Theoretically, the slope of this plot should be 0.667 for space charge limited current but is measured to be around 0.700 to 0.715.

TABLE XII

Electron Gun Emission Current versus Anode Potential

Anode Potential (volts)	Electron Current (milliamperes)
0	0.16
4	1.0
6	2.0
8	2.86
10	3.8
20	8.8
30	15.7
40	22.9
50	33.0
60	41.0
70	51.0
80	60.0
90	70.0
100	79.5
110	89.0
120	100.0

APPENDIX E

Detector Ionizer Operating Procedure

The detector ionizer described in Chapter II should be operated according to the following procedure:

(1) Check all connections to the ionizer carefully and pump the system down to at least 5×10^{-6} tcrr before turn on.

Set the Emission Adjust Control and the Volts Adjust Control to minimum (full CCW[*]). Set the Electron Energy Adjust fully CW[**]. Set the Circuit Monitor Meter Function Switch to 250 volts.

(2) Turn the ionizer on. The meter should indicate about 100 volts of electron energy.

(3) Set the Meter Function Switch to 10 amps. It will read a small filament heating current.

(4) Set the Regulation Mode Selection Switch to the filament voltage setting and slowly advance the filament voltage until some emission is obtained.

(5) Slowly advance the filament voltage until 30-40 ma of emission is obtained.

(6) Allow the system to operate for approximately a ten minute warm-up period.

---

[*] counter clockwise - CCW

[**] clockwise - CW

(7) The extractor voltage setting depends on #1 lens
setting, on emission current and on electron energy.
This potential is usually within ±10 volts of the
ion energy. In general, if #1 lens is operated
highly negative, the extractor can be set a few
volts positive with respect to the ion energy,
compensating for the large negative field reach
through lens #1.

(8) In order to keep the electrons from being accelerated
down the ionizer axis toward the quadrupole, it is
necessary to make at least one of the three lenses
highly negative so that it becomes energetically
impossible for electrons to go beyond that lens.

(9) For focus of the ions, one of the lenses is operated
near the ion energy potential. Lens #2 or lens #3
usually serves this purpose. Lens #1 should not be
operated near the ion potential since it becomes
energetically possible for a large current of
electrons to reach the #1 lens which is operated
from a high impedance power supply.

(10) In high efficiency operation the ion current will not
be proportional to emission current or be a function
of electron energy as one might expect from cross
section curves. This is because the high electron
density in the ionizer and ion space charge neutrali-
zation alter drastically the true potential in the
ionizing region. Thus, changing electron energy or

emission current changes the focus and extraction

in a nearly unpredictable manner.

(11) Immediately after installation of the ionizer,

check the continuity and isolation of each element.

(12) Refer to circuit diagrams provided by Extranuclear

Corporation when troubleshooting. These are kept

on file in the group director's office.

APPENDIX F

Quadrupole Operating Procedures

The quadrupole mass filter described in Chapter II can be aligned
and operated according to the following procedure:

(1) Set Range switch on high-Q head to 2 for the type C

head and to 3 for the type D_2 head. Set the 30-turn

dial to about 17.27 for the C head and about 26.90

for the D_2 head. Turn the toggle switch to Variable,

not Crystal.

(2) On the high-Q head, set the RF balance so that the

screwdriver slot is horizontal. Set the Coarse Reso-

lution so the screwdriver slot is horizontal and set

the Loading halfway between stops. It may be necessary

to loosen the outer locking nuts on these controls so

that they may be turned. The Loading Control has a

lock on the back of the box.

(3) On the Quadrupole Control chassis, set the controls as

follows:

High Cal: 3.00 (three turns from CCW)

Mass Range: Toward High

Low Cal: Full CCW

Sweep Width: Full CCW

Low Mass: Full CCW

Manual Mass: Full CCW

Function Switch: To Align

Level: CCW

Resolution: To 5 on dial

ΔM and Pole Bias: 0 volts on dial

Balance Switch: R.F.

D.C. Balance: Halfway open

With the High Cal set at 3.00, the Mass Meter has a
full scale sensitivity of about 5 KV peak r.f. pole
voltage V, i.e., a reading of 30 on the 100 scale will
represent a 1500 V increment.

(4) Be certain that the mass filter is in a vacuum of 10^{-5}
torr or better so all elements are capable of with-
standing the high peak r.f. voltage which will be
impressed upon them. If the filter is operated at a
pressure of atmosphere to 10^{-4} torr, an arc discharge
may occur.

Turn on the Power switch. After about one minute, the
Standby Light should light. Press the On button. The
Amplifier Plate Current Meter should read about 50 ma.
Slowly advance the Level Control until the Current Meter
reads 200 ma, or until the Level Control is halfway open.

(5) Adjust the Frequency Set dial on the R.F. Power Source
looking for a maximum reading on the Mass Meter. The
Balance Meter may deflect off scale but it is protected
by silicon overload meter protectors. Alternately
adjust the Frequency Set and the Loading on the high-Q
head seeking a higher reading on the Mass Meter. Do
not exceed 300 ma on the Current Meter at any time.

The Frequency Set may need to be changed somewhat from the approximate value of step 2.

In this step it is not only necessary to peak the Loading and Set controls for a maximum, but it will be necessary to offset the Loading and slightly repeak the Set seeking a higher and higher Mass Meter reading several times. Do not exceed a reading of 80 on the Mass Meter since this represents a 4 KV peak r.f. pole voltage, the maximum for which the system is designed. If 80 is reached, it will be necessary to lower the Level Control while continuing the matching procedure. A maximum of 4 KV can be reached on both C and D_2 heads.

Warning

If at any time when the Function switch is in the Align position and the Mass Meter suddenly drops to a low value, an r.f. arc may be occurring in the mass filter or leads. Such an arc can destroy the leads or mass filter since over 100 watts of power may be dissipated in the arc. When the Function switch is in the Manual or Sweep position, the system automatically goes to Standby instantly if such an arc occurs or if for any reason the system cannot regulate to the set mass for more than about 0.05 seconds. If an arc occurs, shut the system off immediately and correct the situation before going on.

(6) Rotate the R.F. Balance Control on the high-Q head until the Balance Meter goes to zero. This indicates proper r.f. balance. If it is not possible to obtain a balance, the external cables and quadrupole present a condition too unbalanced to be corrected with Balance Control (see No. 7 below).

Throw the Balance switch to d.c. and rotate the D.C. Balance knob on the Control chassis until the Balance Meter reads zero. If at any time the d.c. balance falls outside of ± 1 V, it may be necessary to slightly trim the R.F. Balance and/or the D.C. Balance.

(7) Advance the Level Control to maximum and repeat step No. 5. It should be possible to nearly reach or exceed the maximum approximate V for the particular high-Q head used.

Do not exceed 300 ma plate current at any time or the 8122 r.f. power amplifier tube may be damaged.

(8) After proper matching, the Plate Current Meter should indicate between 200-250 ma if the Level Control is full CW, and the high-Q head should be noticeably warm after several minutes of operation. The Frequency Set might be trimmed slightly after warm-up to obtain maximum Mass Meter output.

Rotate the Level Control back and forth. The Mass Meter and Plate Current Meter should follow the action of the Level Control approximately. Do not exceed 80 on Mass Meter.

(9) Turn the Function switch to Manual Mass and advance the
10-turn dial to 1.00 (one turn). The Mass Meter should
now read 10. As the 10-turn dial is advanced, the Mass
Meter should follow number by number until the maximum
output indication that was previously obtained on the
Mass Meter is reached. At this point the Overload
light should come on and the system will trip to Standby.
This is normal since at any time the system cannot produce
the desired regulated output, it will shut down and light
the Overload lamp if the Function switch is in the Manual
or Sweep mode.

(10) After the preceding matching procedure is complete,
lock the Loading coil nuts so the coil will not turn.
Record on the high-Q head panel the Frequency Set and
Range switch settings that were used. It may be
necessary to trim the Frequency Set later, if large
changes are made in the R.F. Balance or Coarse Resolu-
tion. The high-Q head can be removed and reinstalled
later by simply setting the Range and Frequency Set to
the recorded values, the high-Q head will be properly
matched. It may be necessary, however, to trim the Set
dial slightly for maximum Mass Meter readings.

Obtaining a Mass Spectrum

The mass filter will yield a resolved mass spectrum following the
procedure below:

(1) On the Quadrupole Control chassis, set the controls as
   follows:

     High Cal: 3.00 (or as previously calibrated)

     Range Switch: Toward High

     Low Cal: 5.00 (or as previously calibrated)

     Sweep Width: Full CCW

     Low Mass: Full CCW

     Manual Mass: Full CCW

     Function: Manual Mass Tuning

     Level: Full CCW

     Resolution: Full CCW (0.00)

     ΔM and Pole Bias: 0 volts on dial

     Balance Switch: D.C.

     D.C. Balance: to balance d.c.

(2) Make sure that the Pole Bias terminals at the rear of
   the Control chassis are shorted together so the filter
   poles are referenced to ground. If the experimental
   requirements are such that the poles must be referenced
   to another potential, this potential should be applied
   on the red terminal; the black terminal is at chassis
   ground. The potential should not exceed ±400 volts.

(3) Without turning the quadrupole supply on, operate the
   ionizer and the detector system so as to focus ions of
   all masses through the filter (it is operating as a
   field-free drift space) to the detector system with an
   ion energy of about 50 volts.

(4) Turn the quadrupole power supply on and wait until the Standby light comes on and press the On button. Slowly advance the Manual Mass Tuning while observing the ion current. The ion current should now fall off and increase as the Manual Mass is increased through various mass peaks. The resolution will be very poor because the controls are set for the least resolution. The resolution may be so low that very little or no separation will be found.

(5) Advance the Resolution control until separation is obtained between masses. If it is not possible to completely cut off the transmission of the filter by turning the control to full CW, rotate the Coarse Resolution on the high-Q head a few degrees at a time, until the transmission of the filter is reduced to zero. It should now be possible to adjust the Resolution on the Control so that at full CW there is no transmission and at full CCW there is good transmission and poor resolution.

APPENDIX G

Voltage Divider Circuit Diagrams for the Acceleration/Deceleration

Lens System and the Bendix 306 Magnetic Electron Multiplier

Figure 42

Circuit Diagram for Acceleration/Deceleration Lens System Voltage Divider

1. All resistors 100 K ohm, 5%, 2 watt

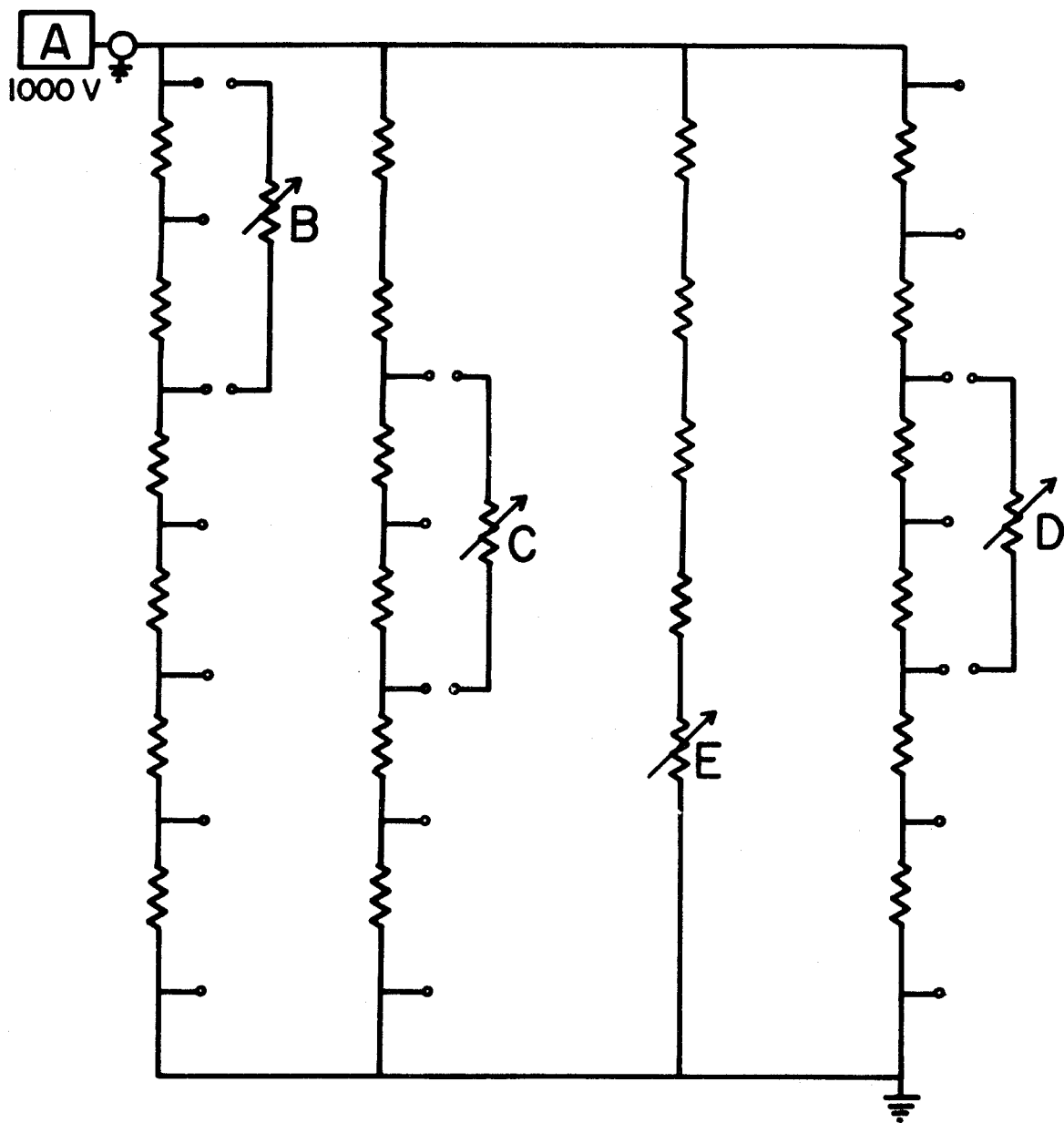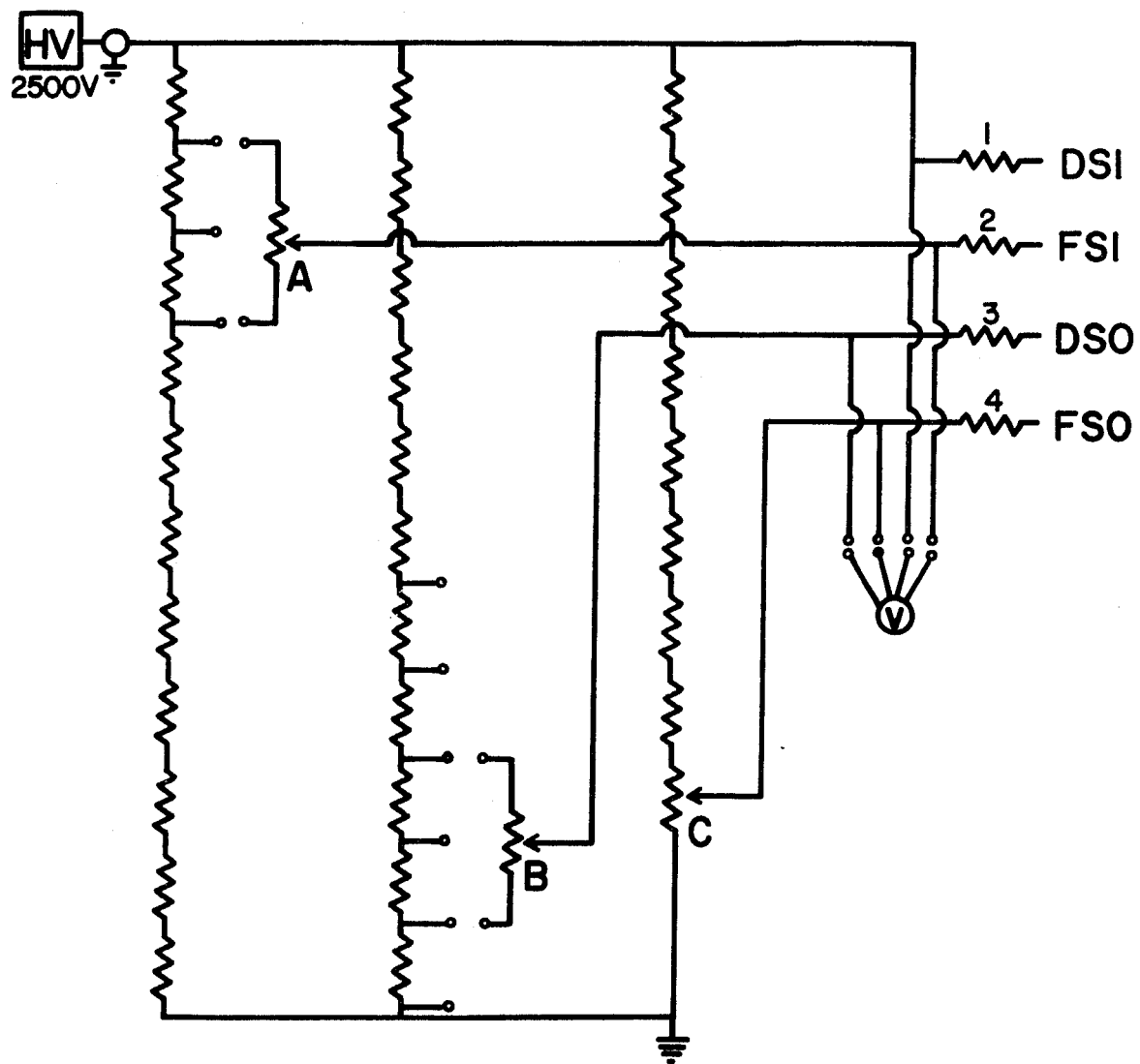2. All helipots - 200 K ohm, 5 watt, 10 turn

Figure 43

Circuit Diagram for Bendix 306 Electron Multiplier Voltage Divider

1. All resistors 100 K ohm, 5%, 2 watt unless otherwise
   indicated.

2. Each helipot – 200 K ohm, 5 watt, 10 turn.

3. Resistors 1, 2, 3, 4 – 1 Megohm each.

APPENDIX H

Recombination Cross Section Calculation

The following is the derivation of the expression used to calcu-
late dissociative recombination cross sections in terms of parameters
observed experimentally. The analysis will be limited to two-body
single collisions.

It is assumed that (a) no projectile interacts with more than one
target; (b) no target particle is shielded by another; (c) the supply
of targets is not depleted by collisions, i.e., the target density
remains constant; (d) each beam is parallel, monoenergetic and composed
of only one species; (e) the interaction region is well defined.

Let ρ = the number of recombination reactions occurring per
cubic centimeter per second,

n_i = the ion density,

n_e = the electron density,

v_r = the relative velocity between the ions and electrons.

Then $\rho = n_i n_e \sigma v_r$.

Integrating both sides of this equation over the volume V

$$\int_V \rho d\tau = \int_V n_i n_e \sigma v_r d\tau \tag{1}$$

The left-hand side is the total number of recombination reactions
per second. Defining an equivalent neutral current as every recombina-
tion reaction contributing one fictitious charge, the total current of
neutrals resulting from the recombination reaction will be

120

$$I_n = e \int_V \rho \, d\tau \tag{2}$$

$$I_n = e \int_V \sigma \, v_r n_i n_e \, d\tau \tag{3}$$

It is assumed also that all neutral particles are detected. The relative geometry between the projectile and target particles can be expressed as

$$v_r = [v_i^2 + v_e^2 - v_i v_e \cos \Theta]^{\frac{1}{2}} \tag{4}$$

where Θ is the angle between the two beams. For beams crossing perpendicularly, $\Theta = 90°$, and

$$v_r = [v_i^2 + v_e^2]^{\frac{1}{2}} \tag{5}$$

The beams are considered circular in cross section, uniform in density in the axial direction, but varying in the radial direction. The interaction region will be of length L.

The volume integral is considered in the cylindrical coordinate system. The current density for each beam is

$$j = nev \tag{6}$$

and solving for density

$$n = j/ev \tag{7}$$

Substituting for the densities and integrating with respect to length

$$I_n = \frac{\sigma [v_i^2 + v_e^2]^{\frac{1}{2}}}{v_i v_e e} \cdot \int_A j_i j_e \, dA \tag{8}$$

121

Solving for the cross section

$$\sigma = I_n \frac{e}{L} \frac{v_i v_e}{[v_i^2 + v_e^2]^{\frac{1}{2}}} \cdot \frac{1}{\int_A j_i j_e dA} \qquad (9)$$

Expressing the above equation in terms of the total ion current and the total electron current

$$I_e = \int_A j_e dA \qquad (10)$$

$$I_i = \int_A j_i dA \qquad (11)$$

$$\sigma = \frac{I_n}{I_e I_i} \frac{e}{L} \frac{v_i v_e}{[v_i^2 + v_e^2]^{\frac{1}{2}}} \frac{\int j_e dA \int j_i dA}{\int j_i j_e dA} \qquad (12)$$

The form factor is represented by

$$F = \frac{\int j_e dA \int j_i dA}{\int j_i j_e dA} \ (cm^2) \qquad (13)$$

Therefore

$$\sigma = \frac{I_n}{I_e I_i} \frac{v_i v_e}{[v_i^2 + v_e^2]^{\frac{1}{2}}} \frac{e}{L} F \ (cm^2) \qquad (14)$$

For a uniform ion beam the form factor reduces to the ion beam area, i.e., indicating no divergence.

APPENDIX I

Consistency Check for In-Phase Noise

Harrison (40) has pointed out that in ion electron crossed beam
experiments errors can result as a consequence of space charge associated
with the beams. These errors can be due to (1) electron space charge
causing ion loss from the beam by deflection, (2) electron space charge
causing variation of the background arising from passage of the ion beam,
and (3) ion space charge causing variation of the background arising from
passage of the electron beam.

The error cited by example (1) can be significant in experiments
where the collision products are ions rather than neutrals. In such
cases loss of both parent and product ions can be made negligible by
proper choice of dimensions, ion optics and by limiting the electron
beam current to a low value. Errors caused by example (2) can arise in
experiments such as the one described by Dolder et al. (41) where doubly-
charged product ions are separated from singly-charged parent ions by a
magnetic field. Background results from doubly-charged ions formed by
charge-stripping collisions between parent ions and residual gas. The
charge-stripped ions are scattered relative to the trajectories of their
parent ions resulting in a divergent product ion beam. If a significant
fraction of this divergent beam is formed before the ions cross the
electron beam and if the divergence is great enough for the ion beam to
be larger than its collector then the background due to charge stripping
is increased by the converging action of the electron space charge and
would interfere with measurement of the collision rate. Errors arising

from example (3) are likely only in experiments where electrons are detected and in excitation experiments where photons are detected close to the collision region.

Hagen (3) refers to such possible errors in his work regarding the dissociative recombination of N_2^+. Attempts were made during consistency check procedures on his apparatus to acquire a signal with a species which should not undergo dissociative recombination. A beam of N^+ ions was tested but no signal indicating system malfunction was observed.

In like manner to the consistency checks described by Hagen, a beam of Ar^+ ions was tested in the apparatus of this report. No dissociative recombination signal was observed with Ar^+ over the range of interaction energies used with all species studied in these experiments. Thus, it was assumed that there was no "in-phase noise" contribution to signals observed with diatomic and polyatomic parent ions.

APPENDIX J

Angular Dispersion Calculation

This derivation will consider only collisions resulting in dissociative recombination for beams of ions and electrons crossing perpendicularly. It is assumed that there are two point particles having masses m_1 and m_2 traveling with lab velocities of v_1 and v_2, respectively. The recombination products will be indicated by masses m_3 and m_4 with velocities v_3 and v_4. The conversion to the center of mass coordinate system is now convenient so the frame of reference is one moving with the center of mass (C.M.) of the colliding particles and not the lab frame of reference.

The principle of conservation of momentum requires that the total momentum be constant during the collision process (42)

$$m_1 v_1 + m_2 v_2 = m_3 v_3 + m_4 v_4 = MV \tag{1}$$

with
$$M = m_1 + m_2 = m_3 + m_4 \tag{2}$$

$$V = (m_1 v_1 + m_2 v_2)/M \tag{3}$$

where V is the center of mass velocity (C.M.).
The velocity of each particle in the center of mass system is the lab velocity minus the C.M. velocity.

$$v_i' = v_i - V \tag{4}$$

where v_i' is the velocity of the i'th particle in the C.M. system and v_i is the velocity in the lab. The relative velocity is defined as

$$v_r = v_1' - v_2' = v_1 - v_2 \tag{5}$$

125

The reduced mass is defined as

$$m_r = m_1 m_2 / (m_1 + m_2) \tag{6}$$

If MV represents the momentum in the center of mass system then

$$\frac{1}{2} MV^2 = E_{C.M.} \tag{7}$$

The initial total energy E_t is

$$E_t = \frac{1}{2} m_1 v_1^2 + \frac{1}{2} m_2 v_2^2 \tag{8}$$

Conservation of energy also requires that E_t be constant. The energy of the two particles in the C.M. system will be

$$e = E_t - E_{C.M.} = \frac{1}{2} m_1 v_1^2 + \frac{1}{2} m_2 v_2^2 - \frac{1}{2} MV^2 \tag{9}$$

where

$$e = \frac{1}{2} m_r v_r^2 \tag{10}$$

The center of mass energy and momentum remain constant during the collision, thus only the relative energy of the two particles need be considered. The C.M. frame of reference moves with the total momentum of the two particles; their total relative momentum is thus zero.

$$m_1 v_1' + m_2 v_2' = m_3 v_3' + m_4 v_4' = 0 \tag{11}$$

$$m_1 v_1' = -m_2 v_2' \tag{12}$$

$$m_3 v_3' = -m_4 v_4' \tag{13}$$

If $\qquad m_r' = m_3 m_4 / M \tag{14}$

and
$$v_r' = v_3' - v_4' \tag{15}$$

then
$$e = \frac{1}{2} m_r' v_r'^2 \tag{16}$$

giving
$$(v_3' - v_4')^2 = e/(\frac{1}{2} m_r') \tag{17}$$

$$v_3' = \left[\frac{2m_4 e}{m_3 M} \right]^{\frac{1}{2}} \tag{18}$$

The parameter e in the case of ion-electron recombination represents reaction exothermicity.